NASA-CR-190934

NCC1-46

AN INVESTIGATION OF THE EFFECTS OF AFT BLOWING ON A 3.0 CALIBER TANGENT OGIVE BODY AT HIGH ANGLES OF ATTACK

LANGLEY GRANT

IN-02-CR

125220

P. 100

by

Nathan M. Gittner

A thesis submitted to the Graduate Faculty of
North Carolina State University
in partial fulfillment of the
requirements for the Degree of
Master of Science

Department of Mechanical and Aerospace Engineering

Raleigh

1992

Approved By:

_____   _____

_____
Chairman of Advisory Committee

Abstract

Gittner, Nathan M. An Investigation of the Effects of Aft Blowing on a 3.0 Caliber Tangent Ogive Body at High Angles of Attack. (Under the direction of Dr. Ndaona Chokani)

An experimental investigation of the effects of aft blowing on the asymmetric vortex flow of a slender, axisymmetric body at high angles of attack has been conducted. A 3.0 caliber tangent ogive body fitted with a cylindrical afterbody was tested in a wind tunnel under subsonic, laminar flow test conditions. Asymmetric blowing from both a single nozzle and a double nozzle configuration, positioned near the body apex, was investigated. Aft blowing was observed to alter the vortex asymmetry by moving the blowing-side vortex closer to the body surface while moving the non-blowing-side vortex further away from the body. The effect of increasing the blowing coefficient was to move the blowing-side vortex closer to the body surface at a more upstream location. The data also showed that blowing was more effective in altering the initial vortex asymmetry at the higher angles of attack than at the lower. The effects of changing the nozzle exit geometry were investigated and it was observed that blowing from a nozzle with a low, broad exit geometry was more effective in reducing the vortex asymmetry than blowing from a high, narrow exit geometry.

Acknowledgements

The author would like to offer his deepest gratitude to the following people for their help and contributions during this research and the preparation of this thesis:

Dr. Ndaona Chokani for serving as chairman of my advisory committee and for many enlightening conversations.

Drs. Fred R. DeJarnette and Kwangil Koh for serving on my advisory committee.

Dr. Robert M. Hall for serving as technical monitor of the research.

Mr. Rufus "Skip" Richardson and Mr. Mike Breedlove for the fabrication of the group A blowing nozzles.

Mr. Art Illingworth and the North Carolina State University College of Engineering Research Services Division for expert counsel and craftsmanship in the fabrication of the group B blowing nozzles.

To my parents, fiancée and very close friends without whom I would never have been able to accomplish such a monumental task.

Table of Contents

Nomenclature

A_{fm} cross–sectional area of the flow meter

A_{ref} reference area, 40 × model base area

C_p pressure coefficient, $(p - p_\infty)/q_\infty$

C_y sectional side force coefficient, based on unit radius and unit length,

$\sum 2\pi C_p \sin \phi$

C_μ blowing coefficient, $(\dot{m}_j u_j)/(q_\infty A_{ref})$

d local diameter of the model

D base diameter of the model

$\dot{m}_j$ mass flow rate through the blowing nozzle

p local static pressure

P_o plenum stagnation pressure

p_∞ free stream static pressure

q_∞ free stream dynamic pressure

R gas constant

T_o plenum stagnation temperature

u_j exit velocity from the blowing nozzle

$\dot{V}$ volumetric flow rate

x axial distance from model apex

$\overline{y}$ distance from the surface of the model to the mean geometric center of the nozzle exit orifice

z_{max} maximum width of the nozzle exit

α angle of attack

γ specific heat ratio

ϕ azimuthal location from windward meridian

ϕ_b azimuthal location of the non–blowing nozzle from the windward meridian

ϕ_j azimuthal location of the blowing nozzle from the windward meridian

ϕ_m roll position of the model

1 Introduction

The flight of high-performance aircraft at high angles of attack is compromised by the effects of the forebody vortices which form and shed asymmetrically. These asymmetric forebody vortices can produce side forces and yawing moments which may render control of the aircraft difficult or even impossible. This problem is compounded at the higher angles of attack by the fact that the conventional control surfaces (vertical and horizontal stabilizers) are washed out by the wake of the fuselage and wings. The combat agility requirements of present and future generation high-performance aircraft dictate the need for controlled flight at high angles of attack, and thus there is a strong motivation to control the forebody vortex asymmetry in this flight regime.

Differing flowfields over an aircraft forebody are observed as the aircraft is pitched through a range of angles of attack, Figure 1. (i)At low angles of attack the flow remains attached to the forebody and vortices do not appear in the flowfield. As the angle of attack increases, the axial flow component decreases while the azimuthal flow component increases. (ii)When the aircraft is moved to a sufficiently large angle of attack, the viscous layer separates from both sides of the body and a pair of symmetric vortices form off the leeside of the forebody. (iii)A continued increase in the angle of attack will change the vortex pattern configuration from

a symmetric pattern to an asymmetric pattern. (iv)Further increase in the angle of attack will lead to unsteady shedding of the vortices with an ensuing pattern resembling a Kármán vortex street.

Figure 2 shows a cross sectional flow plane of a slender forebody at a high angle of attack. The flow approaching the model attaches to the body at the windward stagnation point and moves from the windward side towards the leeward side of the model. As the viscous layer moves towards the leeward region of the model, it encounters an adverse pressure gradient. At sufficiently large angles of attack, this pressure gradient becomes large enough to force separation of the viscous layer from the model surface at the primary separation point. Due to the velocity gradients in the viscous layer, the separated shear layer rolls up and forms the primary vortex on the leeside of the model. The entrainment effects of the vortex cause the flow to reattach to the surface of the body. The flow then moves from the region of localized high pressure to a region of localized low pressure under the primary vortex. At sufficiently large angles of attack, the reattached viscous layer cannot overcome the adverse pressure gradient as it moves below the primary vortex, thus the flow separates at the secondary separation point. This separated viscous layer rolls up and forms a secondary vortex. Due to the entrainment effects of the primary and secondary vortices, the flow reattaches to the body with the reattached flow feeding both the primary and secondary vortices.

A substantial body of evidence has been produced in experimental[2-5] and numer-

ical[6-7] studies which indicates that the forebody vortex asymmetry configuration is produced by small imperfections in the tip of the forebody. Many techniques have been studied to control this vortex asymmetry; a recent review has been presented by Ericsson[8]. These techniques include nose bluntness, body reshaping, boundary layer trips, forebody strakes, and forebody suction and blowing. The forebody blowing techniques[9-18] include normal, forward and aft blowing with respect to the model surface. The previous research in the area of aft blowing has brought about much knowledge in the area of forebody vortex control. For example, a control mechanism has been suggested in references [14–15] for vortex control by jet blowing and is sketched in Figure 3. Once blowing is initiated on the leeward side of the body, the jet entrainment moves the blowing–side separation leeward, thus the vortex on the blowing side of the body moves closer to the body. Due to the coupling of the leeside vortices, the non–blowing–side vortex moves further from the body surface and the separation on the non–blowing side moves windward. Based on this control model, the jet blowing functions primarily to control the flow separation by entrainment due to the jet. Previous research has also shown that (1)the optimal axial location of jet blowing is found to be as close as possible to the forebody apex, since jet blowing at this position can most influence the flow separation and the strong interaction between the vortices; (2)the azimuthal location of the jet blowing is found to be optimal in the range 120° to 150°, measured from the windward ray; and (3)the baseline system of vortices determines the effectiveness of vortex

control by jet blowing. Namely, the jet blowing is more effective for control of the forebody vortex system if the baseline flowfield has only a small degree of vortex asymmetry.[13,14,19,20]

Although previous researches have demonstrated the potential of aft blowing to provide forebody vortex control, questions remain regarding the fluid dynamic nature of the aft blowing technique. Previous experiments have examined the overall effects of aft blowing on an aircraft configuration. Thus, in contrast to previous studies, an experimental study of the flowfield in the near-tip region of an isolated forebody model was conducted. The objective of this study is to obtain further insight into the mechanisms of aft blowing through detailed measurements of surface pressures and flow visualization in the near-tip region. The effectiveness of asymmetric aft blowing from both a single nozzle and a double nozzle configuration was investigated. The effects of angle of attack, magnitude of blowing, and axial and azimuthal blowing nozzle locations are examined. In addition, the effect of the nozzle exit geometry on the blowing effectiveness is also investigated.

2   Apparatus and Procedure

All experiments were conducted in the North Carolina State University Subsonic Wind Tunnel Facility, Figure 4. This is a closed return wind tunnel with a settling chamber to test section contraction ratio of 3:1. The settling chamber is equipped with 3 screens located upstream of the contraction section for the purpose of decreasing the free stream turbulence in the test section. The wind tunnel is ventilated to room pressure through a breather located at the downstream end of the test section. The test section is 0.81m in height, 1.14m in width and 1.17m in length and equipped with plexiglass sides and top to permit flow visualization. The test section velocities were regulated by a variable pitch fan located downstream of the test section. The maximum attainable test section velocity was 17.2 m/s.

The model used for testing was a 3.0 caliber tangent–ogive body fitted with a removable nose tip and a cylindrical afterbody as shown in Figure 5. The model was hollow and of aluminum construction. Three circumferential rows of pressure taps were located on the ogive portion of the model, at the locations shown in Figure 5. The two rows of pressure taps located nearest the model apex, rows 1 and 2, had an azimuthal tap spacing of 15° while row 3, the row farthest from the model apex, had an azimuthal tap spacing of 10°. The model was rigidly mounted on a circular arc sting balance. A stepper motor, attached to the sting balance and controlled

by a computer, was used to provide variation of the angle of attack. A cylindrical plenum chamber, with internal dimensions of 8.1cm in length and a diameter of 2.1cm, was firmly secured to the internal wall of the model. Dried pressurized air, supplied from an external source, was routed along the sting, through the base of the model and to the plenum, while short lengths of tygon tubing supplied air from the plenum to the blowing nozzle.

Figure 6 shows a schematic of a removable nose tip with the exit of the blowing nozzle located at an axial location of $x/D = 0.125$. The blowing nozzles were designed to blow aft, along a model meridian and tangential to the surface of the body. Previous work conducted by Moskovitz[3] showed that as compared to a discrete surface perturbation of a pointed nose tip, a perturbation of a blunt nose tip was less likely to develop vortex asymmetries due to surface roughness or machining imperfections. Thus for the purposes of this study a blunted nose tip was used to minimize the possible effects of the differences in the geometries of the different blowing nozzles that were tested, and thereby accentuate the effects of blowing.

Tables 1 and 2 show the two groups of blowing nozzles that were manufactured for this research. The first group of blowing nozzles, group A, was designed to investigate the effects of angle of attack and the azimuthal and axial locations of the blowing nozzle, while the second group of nozzles, group B, was designed to study the effects of changing the geometry of the nozzle exit orifice. Group A consisted of blowing nozzles numbered 1 – 3 while the second group, group B, comprised nozzles

numbered 4 – 8. Each blowing nozzle was constructed of brass and was securely fitted to its own nose tip. The geometric mean height of the nozzle exit orifice, $\bar{y}/d$, was used as a measure of the effective height from the surface of the body to the geometric center of the jet as it exits the blowing nozzle. The effective width of the jet was characterized by z_{mas}/d, which represents the maximum width of the exit orifice. Blowing nozzles 1 and 3 were of the same exterior dimensions: 0.38cm in height, 0.38cm in width and 0.51cm in length. Nozzle 2 was of the same height and width, but measured 1.27cm long such that the desired x/D of 0.25 would be attained. Blowing nozzles 1 and 2 both had circular cross–section exit areas of diameter 0.159cm, while the exit of nozzle 3 was also circular, but with a smaller diameter of 0.079cm. Blowing nozzles 4 – 8 all had the same exterior dimensions of 0.25cm high, 0.44cm wide and 0.51cm long. Each nozzle exit orifice had the same cross–sectional area, but different geometries. Nozzle 4 was a semi–ellipse with a horizontal major axis; 5 was a semi–circle with a horizontal axis; 6 was an ellipse with a horizontal major axis; 7 was a semi–ellipse with a horizontal minor axis, and 8 was a full circle. The numerical designation of the blowing nozzles, 4 – 8, indicated an ascending geometric mean height. For some test cases, a blank nozzle was positioned at a symmetric location to the blowing nozzle with respect to the windward ray. The purpose of this blank nozzle was to provide an initial vortex pattern that was less asymmetric when compared with a single nozzle being placed on the model. These blank nozzles were of the same exterior dimensions as the

blowing nozzles and were glued directly onto the model surface. All blowing nozzles were calibrated following the procedure described in Appendix 1.

Surface pressures were measured using a pair of 8.9cm of water Validyne differential pressure transducers connected to a pair of 48–port Scanivalve modules and a Hewlett–Packard 9122 computer. The transducers' sampling time was 0.167 seconds, and thus time averaged pressures were obtained. Flow visualization was conducted using a helium bubble technique as discussed by Moskovitz[3]. Two different flow visualization configurations were used. The first configuration was used to obtain side view visualization of the vortices. An arc lamp was positioned such that the emitted beam was nearly parallel to the upper surface of the model and the vortex trajectories could be observed. Neutrally buoyant helium bubbles were introduced into the flowfield, via a bubble wand, placed upstream of the model apex. The bubbles in the flowfield were illuminated by the arc lamp, and side view visualization of the vortices was possible. The second configuration used for flow visualization allowed for cross–sectional images of the vortices to be obtained. The arc lamp was positioned such that the light beam was directed perpendicular to the model axis with only a sheet of light (approximately 0.5 inches thick) allowed to illuminate the model. The bubble wand was traversed across the test section upstream of the model and emitted helium bubbles into the free stream flow. As the helium bubbles passed through the light sheet, they were illuminated and the forebody vortices were made visible. The camera shutter was held open for ap-

proximately 12 seconds to allow a satisfactory number of bubbles to traverse the light plane such that an acceptable image of the vortices was obtained. The high velocity air exiting from the blowing nozzle made resolution of the vortices on the blowing nozzle side of the body poor, thus only limited results were obtained from this method of flow visualization.

Wind tunnel testing was conducted at a free stream velocity of 13.7 m/s for the pressure measurements and 4.6 m/s for the flow visualization. These velocities corresponded to laminar flow Reynolds numbers, based on the model base diameter, of 84000 and 28000 respectively. The angle of attack was varied from 40° to 60° in 10° increments, while sideslip was held constant at 0°. C_μ's investigated ranged from 0.0035 to 0.028 for group A nozzles and from 0.01 to 0.02 for group B.

3   Results and Discussion

3.1   "Clean" Model

A series of initial tests were conducted prior to positioning the blowing nozzles on the model. For these tests the nozzle was removed from the nose tip and the orifice on the model surface was sealed with body filler and filed smooth to the contour of the nose tip. The purpose of these tests was to measure the flowfield around the model before modifications for blowing were made to the model. These initial test conditions will be referred to as the "clean" model case.

Different degrees of vortex asymmetry were observed over the range of angles of attack investigated. Figure 7 shows the pressure coefficient distributions for the "clean" model at a roll position of 120°. This roll position was taken as a representative case of the trends observed for these test conditions. When the model was positioned at 40° angle of attack, the vortices on the leeside of the body were quite symmetric. This is observed by the leeside pressure coefficients being of equal magnitude. As the angle of attack increased to 50°, a slightly asymmetric vortex pattern was observed. At $\alpha = 60°$, the leeside vortices assumed a more asymmetric vortex pattern with large differences observed in the measured leeside pressure coefficients. The vortices on both the port and starboard sides of the

model were observed to move away from the model surface in the axial direction. This is noted by the decrease in magnitude of the C_p's on the leeside of the body from row 1 to row 3. The corresponding flow visualization for the test conditions of Figure 7 is shown in Figure 8. These results confirm the measured increase in vortex asymmetry with increasing angle of attack.

Figure 9 shows the sectional side force plots for the "clean" model. The sectional side force was obtained by integrating the pressures over the surface of the model while the variation in the sectional side force was obtained by rolling the model. When the model was at 40° angle of attack, small magnitudes of C_y were observed. This corresponds with the symmetric vortex pattern measured in the pressure plots. At $\alpha = 50°$, the sectional side forces were larger in magnitude with a general sinusoidal pattern observed as the model was rolled through 360°. For the 60° angle of attack case, large C_y's were observed, as expected from the large vortex asymmetry observed in the pressure data. The above results show that for the "clean" model, increased degrees of vortex asymmetry are observed as the angle of attack was increased. These results verify that the basic steady flow regimes could be attained with the model over the range of angles of attack tested.

3.2 Single Nozzle Configuration (Group A)

The next phase of this research consisted of placing a single blowing nozzle from group A on the model. First, tests were conducted with the blowing nozzle sealed, i.e. $C_\mu = 0$, to measure the effects of positioning the nozzle on the model. The nozzle was then unsealed and blowing initiated. The effects of varying the angle of attack, the blowing coefficient and the axial and azimuthal locations of the blowing nozzle were investigated.

Blowing nozzle 1 was positioned on the model and sealed, $C_\mu = 0$. Figure 10 shows the pressure coefficients for this case at all 3 angles of attack tested with the blowing nozzle positioned at an azimuthal location of $\phi_j = 120°$. The nozzle location of $\phi_j = 120°$ was chosen to correspond to previous researches in the area of aft blowing. When the model was positioned at 40° angle of attack a slight vortex asymmetry was observed. The vortex on the nozzle side of the body assumed the "high" vortex position, that is, it was located further from the model surface than the non-blowing-side vortex, which assumed the "low" vortex position. At 50° angle of attack the same trend was observed, but the vortex asymmetry was much greater. At $\alpha = 60°$, still greater vortex asymmetries were observed. The effect of the blowing nozzle was to force separation of the viscous layer from the surface of the model at an azimuthal location closer to the windward ray on the nozzle side of the model than on the opposite side of the model. This asymmetric separation

of the viscous layers from the body surface led to the asymmetric vortex pattern observed at all 3 angles of attack. The magnitude of the pressure coefficients of rows 1, 2 and 3 on the blowing–nozzle side of the model were relatively equal at all three angles of attack tested, while the magnitude of the pressure coefficients on the opposite side of the body increased as the angle of attack increased. This indicated that for the no–blowing case, the vortex on the nozzle side of the body did not move relative to the body with increasing angle of attack.

The sectional side force plots for the no blowing case are shown in Figure 11. As observed in the "clean" model tests, the magnitude of the side force increased as the angle of attack increased. The presence of the sealed blowing nozzle forced separation of the viscous layer from the model such that the resulting vortex assumed the "high" vortex position. Thus, the sectional side force was in the direction opposite to the side equipped with the blowing nozzle. As the model was rolled, a general sinusoidal variation in C_y was observed. Comparing this data with the "clean" model case presented in Figure 9, the vortex asymmetry and resulting sectional side force were larger in magnitude when the blowing nozzle was positioned on the model. Thus the effect of adding the blowing nozzle was to increase the initial asymmetry of the leeside vortices. This no–blowing test case will be taken as the "baseline" condition.

The blowing nozzle was unsealed and the effects of blowing at $x/D = 0.125$ were examined. Figure 12 shows the effect of varying the blowing coefficient. The model

was positioned at 50° angle of attack with blowing nozzle 1 positioned at $\phi_j = 120°$. This was taken as a representative case of the trends observed at the three angles of attack tested. Once blowing was initiated, the vortex asymmetry was observed to decrease as compared to the baseline conditions. For the case with $C_\mu = 0.007$, the pressure coefficients of rows 1 − 3 are approximately equal in magnitude at each azimuthal location from $0° \leq \phi \leq 105°$. For the baseline case, this was only observed over the range $0° \leq \phi \leq 45°$. Thus the effect of blowing was to move the separation location of the viscous layer from the model surface to a more leeward location. As the separation location of the viscous layer moved leeward, the vortex formed by the separated viscous layer moved closer to the leeside of the body, while the coupling of the leeside vortices caused the non−blowing side vortex to move further away from the model surface. These results are consistent with previously proposed control mechanisms of aft blowing.

It is also worth noting the effects of increasing the magnitude of the blowing coefficient. At the lowest blowing coefficient tested, the vortex on the blowing-nozzle side of the body was observed to move closer to the model surface from row 1 to row 3. For the $C_\mu = 0.028$ case, little movement of the blowing-side vortex with respect to the model surface in the axial direction was observed, as denoted by small differences in the pressure coefficients of rows 1 − 3. Thus the effect of increasing the blowing coefficient was to move the blowing-side vortex closer to the body surface over a shorter axial distance. Minimal differences in the pressure

coefficients were observed on the opposite side of the model as C_μ was varied.

Figure 13 shows the flow visualization results for the same test case. For the no-blowing case, the vortex on the blowing-nozzle side of the model is at the high vortex position and the opposite vortex is positioned at the low vortex position, while both of the vortices are observed to move away from the model surface in the axial direction. These results confirm the trends observed in the C_p distributions. Once blowing was initiated, the non-blowing-side vortex moved further away from the model surface and closer to the windward ray, while the blowing-side vortex appeared to move closer to the model surface (although resolution is poor due to the high velocity air exiting from the blowing nozzle). As C_μ was increased, the non-blowing-side vortex was observed to move further away from the model; this effect was not so clearly evident in the above C_p distributions. However, since the vortices are coupled, this observation is consistent with the changes in the C_p distribution observed on the blowing nozzle side of the model, which suggested that the blowing side vortex moved closer to the model as C_μ increased. Comparing rows 2 and 3 at a fixed C_μ, the non-blowing-side vortex was observed to move away from the model surface in the axial direction as expected from the C_p distributions.

The effect of varying C_μ on the sectional side force is examined in Figure 14. Compared with the baseline case, the magnitude of the sectional side force decreased once blowing was initiated; small changes in C_y are observed with increasing C_μ. Compared with the baseline conditions, the general trend of blowing with a single

blowing nozzle was to decrease the magnitude of C_y for rows 1 and 2 while for row 3, the sectional side force was observed to change sign, indicating a reversal of the vortex asymmetry.

With blowing, the sectional side forces were greatly reduced; however, the magnitude of the blowing coefficient appeared to have little effect on the sectional side force over the range of C_μ's investigated. The blowing apparently had an "on/off" effect, and not a gradual effect on the vortex asymmetry as C_μ was varied. As previously discussed, the presence of the blowing nozzle generated an initial asymmetric flowfield within which the effect of blowing was examined. It is likely that this initial flowfield resulted in too severe an environment to obtain gradual control on the degree of the vortex flow asymmetry.

The effect of blowing at varying angles of attack is shown in Figure 15. Blowing nozzle 1 was positioned on the body at an azimuthal location of 120° and the blowing coefficient was 0.014. When comparing this data to the no-blowing case, a more marked effect was observed at the larger angle of attack ($\alpha = 60°$), than at the lower ($\alpha = 40°$). As the angle of attack is increased, the axial flow velocity component along the surface of the body is decreased, while the azimuthal flow velocity component is increased. The effect of aft blowing is to add high velocity air in the axial direction, thus augmenting the axial flow component. Therefore, at the higher angles of attack where the axial flow component is smaller, the effect of blowing on the flowfield is observed to be more significant.

It is pertinent to point out changes in the pressure coefficient distributions for varying angles of attack on the blowing side of the body. For $\alpha = 50°$, a sharp decrease in the pressure coefficient of row 3 was observed at $\phi = 140°$. Because this decrease in the pressure coefficient was observed only at row 3 and not at the two most upstream rows, it could not be attributed to suction effects of the high velocity jet exiting the blowing nozzle. It is believed that this is associated with a secondary vortex, resulting from the interaction of the blowing–side vortex, which is located close to the model surface, and the viscous layer. Slight evidence of this secondary vortex appears for the 40° angle of attack case at $\phi = 130°$. At $\alpha = 60°$, the secondary vortex appeared at $\phi = 150°$ for row 3, while some evidence of this vortex was also observed at row 2 ($\phi = 135°$). Thus, as the secondary vortex moved further aft along the body, it was observed to move closer to the leeward ray.

Figure 16 shows the corresponding sectional side force plots. At the lowest angle of attack ($\alpha = 40°$), the general trend of blowing was to reduce the magnitude of the sectional side force compared to the baseline conditions. At $\alpha = 50°$, the magnitude of C_y for rows 1 and 2 was decreased while the C_y of row 3 was reversed. For the $\alpha = 60°$ case, the sectional side force was reduced for row 1; the C_y for row 2 was reduced to approximately zero for all ϕ_j, while the C_y for row 3 was reversed. As observed in the C_p distributions, aft blowing is seen to have a more marked effect at the larger angles of attack than at the smaller angles of attack.

Blowing nozzle 2 was positioned on the model to investigate the effects of blowing

further from the model apex, $x/D = 0.25$. The baseline C_p distributions are plotted in Figure 17 with $\phi_j = 120°$. These results show that the blowing–nozzle–side vortex assumed the "high" vortex position while the opposite vortex assumed the "low" vortex position. These results show that the baseline vortex pattern is the same as observed for blowing nozzle 1, Figure 10. The sectional side forces for the same test conditions were also plotted, Figure 18. The magnitudes and trends observed for the baseline case of blowing nozzle 1 were also observed in the results of nozzle 2. Thus, these results show that the baseline vortex asymmetry that blowing must overcome was quite similiar for both blowing nozzles.

Figure 19 shows the C_p distributions for this nozzle positioned at $\phi_j = 120°$ with $C_\mu = 0.007$ and the range of angles of attack investigated. These results show the same magnitudes and trends in the C_p distributions as those observed when the blowing nozzle was placed at a more upstream location, $x/D = 0.125$. When the sectional side forces were plotted, Figure 20, the same trend observed when the blowing nozzle was positioned at $x/D = 0.125$ was also observed at this axial location, namely the effect of blowing was to reduce the magnitude of the sectional side force.

A final series of tests with a single blowing nozzle was conducted to further investigate the effects of blowing at an even lower C_μ than previously tested. The purpose of this was to examine if proportional control of the vortex asymmetry could be obtained with a single blowing nozzle. Figure 21 shows the C_p distributions for

blowing nozzle 3 positioned at $\phi_j = 120°$. The blowing coefficient was 0.0035 and the angles of attack were 40°, 50° and 60°. Comparing this case with the $C_\mu = 0.014$ case (Figure 15) the leeside C_p's were generally smaller in magnitude. When comparing the asymmetry of the leeside vortices, it was observed that both C_μ's provided approximately the same degree of vortex asymmetry. Thus the lower C_μ was less effective in moving the leeside vortices closer to the model surface when compared to the larger C_μ, but only small differences were observed in the degree of vortex asymmetry between the two blowing coefficients.

When the sectional side forces for this case were plotted, the observation of small differences in the vortex asymmetry were confirmed. Figure 22 shows the sectional side force plots for blowing nozzle 3 at all angles of attack tested. When compared with the $C_\mu = 0.014$ case (Figure 16), the sectional side forces were almost identical in magnitude for $\phi_j = 0°$ to 180° while slightly larger differences in the C_y were observed for 180° to 360°. Thus, over the range of blowing coefficients investigated, $0.0035 \leq C_\mu \leq 0.028$, proportional control of the vortex asymmetry was not observed.

3.3 Double Nozzle Configuration (Group A)

Initial testing was conducted on the model with the blowing nozzles sealed, i.e. $C_\mu = 0$, to determine the baseline flow around the model. Figure 23 shows the C_p

distributions for the model with blowing nozzle 1 located on the body and sealed. The angle of attack was increased from 40° to 60° in 10° increments. At $\alpha = 40°$, the vortices on the leeside of the body were quite symmetric. When the angle of attack was increased to 50°, a small degree of vortex asymmetry was observed. The vortex on the blowing-nozzle side of the body was positioned closer to the model surface than the non-blowing-side vortex. At the largest angle of attack tested, $\alpha = 60°$, the vortex asymmetry was greater than observed at the two former angles of attack. It is necessary to point out that the vortex asymmetry observed for these test conditions, namely when both the blowing nozzle and the blank nozzle were positioned on the model, was not as large when compared with the previous test cases when only the single blowing nozzle was fastened to the model. Thus the initial vortex asymmetry that blowing must alleviate was not as adverse as compared with the previous test cases.

The blowing nozzles were unsealed and blowing was initiated. Figure 24 shows the C_p distributions for the model positioned at 60° angle of attack while the blowing coefficient, C_μ, was varied. At the lowest blowing coefficient investigated, $C_\mu = 0.0035$, the vortex asymmetry was observed to be opposite that of the baseline case. The blowing-side vortex was positioned closer to the model surface than the non-blowing-side vortex. In the axial direction, namely from row 1 to row 3, the vortex on the blowing nozzle side of the model moved closer to the model, while the opposite vortex moved further away from the body surface. At the moderate blowing

coefficient tested, $C_\mu = 0.014$, a more marked difference between the blowing test case and the baseline tests was observed on the blowing–nozzle side of the body. The magnitude of the sectional side force of row 1 was less than that observed at the lower blowing coefficient, while the C_y of row 3 was greater in magnitude. Continued increase in the blowing coefficient moved the blowing–side vortex closer to the model surface. Thus the same trends observed when the single nozzle configuration was tested were also observed for the double nozzle configuration, but the effect of varying the blowing coefficient was more noticeable when a second, symmetrically positioned nozzle was added to the body.

The effect of blowing at different angles of attack was also investigated. Figure 25 shows the pressure coefficient distributions for all 3 angles of attack investigated at a C_μ of 0.014. Compared with the baseline test cases, Figure 23, the effect of blowing at $\alpha = 40°$ on the pressure coefficients was observed to be small. Localized differences in the pressure coefficients on the blowing side of the model were observed, while small differences in the C_p distributions were measured on the opposite side of the model. At $\alpha = 50°$, the effect of blowing was more noticeable on the C_p distributions. On the blowing–side of the model, the magnitude of the pressure coefficients of row 1 was observed to decrease, while for row 3, the magnitude of the C_p increased. At the largest angle of attack tested, $\alpha = 60°$, blowing had a much larger effect on the pressure coefficients. A strong secondary vortex was observed on the blowing side of the model at row 3 ($140° \leq \phi \leq 170°$).

3.4   Single Nozzle Configuration (Group B)

The next portion of this research was an investigation of a method to improve the effectiveness of aft blowing by varying of the orifice exit geometry of the blowing nozzle. Five different blowing nozzles were fabricated (specifications are shown in Table 2) for this portion of the research. The purpose of this section of the research was to determine if the effects of aft blowing could be enhanced by varying the nozzle exit geometry when a single blowing nozzle was positioned on the model.

Figure 26 shows the pressure coefficient distributions for the baseline test case. The trends observed with blowing nozzle 8 were taken as a representative case from the nozzles of group B. The blowing nozzle was positioned on the model at $\phi_j = 120°$ and sealed, $C_\mu = 0$, while the angle of attack increased from 40° to 60° in 10° increments. The same trend was observed for this baseline test case as when the single blowing nozzles of group A were positioned on the body, namely increasing vortex asymmetry with increasing angle of attack. Figure 27 shows the sectional side force plots for the same test conditions. Again, the same trends that were observed from the previous baseline case where only a single blowing nozzle was used, group A, were also observed for this test case, namely the magnitude of the sectional side force increased as the angle of attack was increased.

Figure 28 shows the baseline sectional side forces plotted against the mean geometric center of the blowing nozzle exit plane, $\overline{y}/d$. It is observed that the variation

of the sectional side force of each row and angle of attack is small. This shows that the effects of interchanging the blowing nozzles was small and that the baseline conditions for all five blowing nozzles were similiar.

The pressure coefficient distributions for each of the five blowing nozzles from group B are plotted in Figure 29. The angle of attack was held constant at 50°, the blowing nozzle was located 120° from the windward ray and the blowing coefficient was set at 0.02. With the exception of the C_p distribution of blowing nozzle 7, all of the blowing nozzles produced almost identical C_p distributions. The magnitudes and trends observed for these four blowing nozzles were quite similar. Localized differences in the pressure coefficients were observed on the blowing–nozzle side of the model while small differences in the pressure coefficients were measured on the opposite side of the body. Nozzle 7 produced a slightly different C_p distribution. The vortex asymmetry for this blowing nozzle was slightly more asymmetric and closer to the baseline vortex asymmetry at rows 1 and 2 while at row 3 the vortex asymmetry did not change compared to the baseline case. This indicated that blowing from this nozzle was less effective in reducing the initial vortex asymmetry when compared to the other nozzles of group B.

The sectional side forces for the same test conditions are plotted in Figure 30. The general trend of aft blowing in the range $0° \leq \phi_j \leq 180°$ was to reduce the vortex asymmetry of rows 1 and 2 while reversing the asymmetry of row 3. For $180° \leq \phi_j \leq 360°$, blowing generally reduced the vortex asymmetry of row 1 while reversal

of the vortex asymmetry was observed for rows 2 and 3. The sectional side force for each one of the blowing nozzles generally followed the same pattern, except for blowing nozzle 7, which exhibited noticeable differences from the trends observed in the other four blowing nozzles. For nozzle 7, the measured vortex asymmetry of row 1 was larger for the blowing case than for the non-blowing case while the reduction in the asymmetry of the vortices at rows 2 and 3 was less than that observed when the other 4 blowing nozzles were used. It is worth pointing out that the geometry of nozzle 7 was the semi-ellipse with horizontal minor axis. From the pressure and side force results it may be inferred that aft blowing from a tall, slender nozzle exit was not as effective in reducing the vortex asymmetry as compared to the other four blowing nozzles from this group.

Figure 31 shows the sectional side forces plotted against the mean geometric center of the nozzle exit orifice, $\bar{y}/d$. The blowing coefficient was $C_\mu = 0.02$ and the blowing nozzles were positioned at $\phi_j = 120°$ over the range of angles of attack tested. For the lowest angle of attack tested, $\alpha = 40°$, a small decrease in magnitude of the sectional side forces was observed between the no-blowing sectional side forces, which were 0.8, 0.7 and 1.0 for rows 1, 2 and 3 respectively, and the blowing C_y's. For the 50° angle of attack case, blowing was observed to have a more marked effect on the vortex asymmetry. The measured C_y's for the blowing case were smaller in magnitude than the non-blowing sectional side forces, which were 1.8, 2.0 and 2.5 for rows 1 – 3 respectively. A peak in the sectional side forces is observed

at $\overline{y}/d = 0.0627$ (blowing nozzle 7). This confirms previous results which showed this particular blowing nozzle was the least effective in reducing the initial vortex asymmetry. For $\alpha = 60°$, the baseline C_y's were 3.2, 2.5 and 3.4 for rows 1, 2 and 3 respectively. These were much larger in contrast to the blowing C_y's. Again, blowing nozzle 7 exhibited the least effectiveness in reducing the initial vortex asymmetry.

It is interesting to note how the magnitude of the sectional side force varies for each row. For $\alpha = 40°$, it was observed that the magnitude of the sectional side forces for each row was relatively constant with changing $\overline{y}/d$. As the angle of attack increased to 50°, the magnitude of the sectional side force was observed to vary more with $\overline{y}/d$ than observed at $\alpha = 40°$. At the largest angle of attack tested, $\alpha = 60°$, the C_y's were observed to vary considerably for different blowing nozzles. For row 1, the sectional side force is observed to vary from 0.7 to 2.2, while the magnitude of the sectional side force varies little for row 3, -1.0 to -1.5. Thus, for the single blowing nozzle configuration, the effects of varying the nozzle exit geometry were observed to be less marked at more downstream locations.

The effect of varying C_μ was also investigated, Figure 32. The model was set at $\alpha = 60°$ with blowing nozzle 8 located at $\phi_j = 120°$. Similar trends were observed in the pressure coefficient distributions at both blowing coefficients. On the non-blowing side of the model, small differences in the C_p distributions were observed, while slightly larger differences were measured on the blowing side of the model.

Figure 33 shows the effect of increasing the magnitude of the blowing coefficient

on the sectional side force for the same test conditions. The effect of blowing was to decrease the magnitude of the sectional side force of rows 1 and 2 while reversing the vortex asymmetry for row 3 for $0° \leq \phi_j \leq 180°$. For $180° \leq \phi_j \leq 360°$ blowing generally decreased the magnitude of the sectional side force for row 1 and fully reversed the vortex asymmetry for rows 2 and 3. As the magnitude of the blowing coefficient increased, small differences in the sectional side forces were observed. Just as when the single blowing nozzles of group A were positioned on the body, proportional control of the vortex asymmetry was not observed.

3.5   Double Nozzle Configuration (Group B)

Initially the model was tested with the blowing nozzles sealed, that is $C_\mu = 0$. Over the range of angles of attack investigated, varying degrees of vortex asymmetry were observed. Figure 34 shows the pressure distributions for blowing nozzle 7. This data is representative of the trends observed for the no–blowing cases with the four other blowing nozzles from this group. When the model was positioned at 40° angle of attack, the vortices on the leeside of the model were quite symmetric. As the angle of attack increased through 50° to 60°, the degree of vortex asymmetry was also observed to increase. The vortex on the blowing–nozzle side of the model assumed the "high" vortex position while the opposite vortex assumed the "low" vortex position. Both the blowing–side and non–blowing–side vortices were observed to

move away from the model surface in the axial direction. These no–blowing cases will be taken as the "baseline" test conditions for this portion of the research.

Figure 35 shows the sectional side force plotted against the mean geometric center of the blowing nozzle exit plane, $\bar{y}/d$, for the baseline test cases. As expected from the above C_p distributions, for each blowing nozzle, that is a fixed $\bar{y}/d$, the magnitude of the sectional side force increased with increasing angle of attack. This confirmed the increase in the vortex asymmetry with increasing angle of attack. At each angle of attack, relatively small variations in C_y were observed with changing $\bar{y}/d$. This result indicated that the effects of interchanging the blowing nozzles were minimal, and that within the machining accuracy of the different blowing nozzles, the baseline conditions were the same for all five blowing nozzles. It is also relevent to point out that the baseline sectional side forces for the double nozzle configuration are smaller in magnitude than for the single nozzle configuration (Figure 28).

Figure 36 shows the effect of blowing at the intermediate angle of attack (α = 50°) and the smallest blowing coefficient ($C_\mu = 0.01$) for the blowing nozzles of group B. These C_p distributions are quite representative of the trends observed at the higher blowing coefficients and at the other angles of attack tested. Compared to the baseline case, a larger degree of vortex asymmetry was observed with blowing. The blowing–side vortex was positioned closer to the model surface, thus assuming the "low" vortex position, than the non–blowing–side vortex, which assumed the "high" vortex position. In the axial direction along the body, the variations in the

leeside pressure distributions showed that the blowing–side vortex moved closer the model surface while the opposite vortex was observed to move away from the body. This trend was observed for all five nozzle exit geometries. However, it was observed that blowing nozzles 7 and 8 produced the largest degree of vortex asymmetry at the upstream location, row 1, and the least asymmetry at the downstream location, row 3. On the other hand, blowing nozzles 4, 5 and 6 produced the maximum asymmetry at row 3, and the least asymmetry at row 1. The former set of nozzles (7,8) were those that overall had a higher mean geometric center compared with the latter set of nozzles (4–6). This would suggest that the higher the mean geometric center the more quickly in the downstream direction is the effectiveness of blowing lost; on the other hand, the lower the mean geometric center, the further downstream is the effectiveness of the blowing maintained.

The effect of blowing was also examined in the sectional side force plot, Figure 37. The model was positioned at $\alpha = 60°$, with $C_\mu = 0.01$. The largest difference in magnitude of the sectional side force between the baseline and blowing cases was observed for the three blowing nozzles, 4 – 6, for which the mean geometric center was closest the surface. The other two nozzles, 7 and 8, which had mean geometric centers further away from the surface, were effective with blowing, but not as effective as the former set of nozzles. It is interesting to notice that there is a marked change in the blowing effectiveness at $\bar{y}/d = 0.06$. For $\bar{y}/d < 0.06$, the sectional side force is approximately 0.0, -1.7 and -2.5 for rows 1, 2 and 3

respectively, while for $\bar{y}/d > 0.06$, the respective C_y's are 1.1, -0.3 and -1.2. This result indicates that there may exist a critical mean geometric height below which blowing is most effective (for this study it is $\bar{y}/d = 0.06$). It is also observed that further reduction in the mean geometric height below this critical value does not provide proportionally more gain in the blowing effectiveness.

The results in Figure 37 are also instructive to examine the effect of the nozzle exit geometry on the effectiveness of blowing. For the nozzle exits with $\bar{y}/d < 0.06$, the elliptic nozzle exit, nozzle 6, and semi–elliptic nozzle exit with horizontal major axis, nozzle 4, were the most effective while the semi–circular exit, nozzle 5, was observed to be only slightly less effective. Comparing nozzles 5 and 6, it is observed that although the mean geometric center of blowing nozzle 5 was less than that of blowing nozzle 6, the former nozzle exit was narrower than that of the latter. It would thus appear that a wider nozzle exit is more beneficial for blowing effectiveness. The effect of the nozzle exit width is further demonstrated by comparing blowing nozzles 6 and 7, which have nearly identical mean geometric centers, but in which the former nozzle is wider, $z_{max}/d = 0.235$, than the latter blowing nozzle, $z_{max}/d = 0.167$. The broader nozzle exit is observed to be more effective in blowing. Overall, these results suggest that a low, broad nozzle exit geometry is more effective for blowing than a high, narrow nozzle exit.

The effects of blowing with the two most effective blowing nozzles, 4 and 5, over the range of angles of attack tested are shown in Figure 38. The blowing coefficient

was set at $C_\mu = 0.01$. At $\alpha = 40°$, the blowing–side vortex was positioned closer to the model surface, compared with the baseline case, Figure 34, while the non–blowing–side vortex was positioned further from the model surface. The effect of blowing was to induce a small degree of asymmetry at this angle of attack. At $\alpha = 50°$, the blowing reduced the asymmetry at row 1, and completely reversed the asymmetry at rows 2 and 3, as compared to the baseline case. The effect of blowing was to move the blowing–side vortex closer to the model surface, and move the non–blowing–side vortex further away from the body when compared to the baseline test case. The variations in the leeside pressure coefficients indicate that the blowing–side vortex moved closer to the model surface in the streamwise direction, while the non–blowing–side vortex moved further away from the surface. At $\alpha = 60°$, the blowing induced a strong flow asymmetry, which was in the opposite sense to, and more marked than the flow asymmetry for the baseline flow conditions. The trends in the effect of blowing at this angle of attack were similar to those at 50° angle of attack, but more marked.

Figure 39 shows the sectional side forces plotted against the mean geometric height, $\bar{y}/d$, for all five blowing nozzles at a blowing coefficient of 0.01, at the three angles of attack tested. At $\alpha = 40°$, the effect of interchanging the blowing nozzles (that is varying $\bar{y}/d$) was small, but the changes were more marked than the baseline data presented in Figure 35. It should be noted that the trends in C_y as the mean geometric height is varied are different between the blowing and

baseline cases. This is a further indication that the trends with blowing obtained in this study were a consequence of the nozzle exit geometry, and not indicative of changes in the exterior geometry of the nozzle, which was previously noted to be small. The data in Figure 39 shows that at $\alpha = 40°$, blowing had little effect on the vortex asymmetry at rows 1 and 2 for all nozzles; while a small reversal in the vortex asymmetry was observed at row 3. A slightly larger effect on the baseline vortex pattern from blowing was observed for the smaller mean geometric height. At the higher angles of attack, $\alpha = 50°$ and $60°$, the effect of blowing is observed to be more dramatic than that at $\alpha = 40°$, when compared with baseline data presented in Figure 35. In addition, the effect of varying the nozzle exit geometry, as seen by the changes in C_y against $\overline{y}/d$, are more marked than at the lower angles of attack. In particular it is again noted that the jump in C_y around $\overline{y}/d = 0.06$ is more pronounced at the higher angles of attack, and that the largest effectiveness in blowing is obtained by the low, broad nozzle exit geometries.

In the final phase of the study the effects of changing the magnitude of the blowing coefficient was examined. A representative case of these results was the data for blowing nozzle 6 at $\alpha = 50°$ with $C_\mu = 0.01$ and 0.02, Figure 40. The C_p distributions were of the same magnitude and followed the same trends for both blowing coefficients tested with only localized differences in the C_p distributions observed on the blowing–nozzle side of the body. For the C_p's of row 1, the initial flow asymmetry observed in the baseline data was reduced, with the change in flow

asymmetry being greater at the higher blowing coefficient, while the differences in the C_p distributions of rows 2 and 3 were much less noticeable when compared to row 1. Just as observed with the previous single nozzle configurations, the effect on increased blowing was to move the blowing–side vortex closer to the model surface over a shorter axial distance. The sectional side forces for the above test case are plotted in Figure 41. Only small differences in the magnitude of C_y were observed as C_μ varied with the same trends in C_y observed for both blowing coefficients tested.

4 Conclusions

An experimental study has been conducted to examine the effectiveness of aft blowing as a method of forebody vortex control. A 3.0 caliber tangent ogive model fitted with a cylindrical afterbody was tested in subsonic, laminar flow conditions. Testing was conducted using both a single nozzle and a double nozzle configuration; for the double nozzle configuration, blowing was applied through only one nozzle. The following conclusions were drawn from this research:

(1)   Aft blowing was effective in reducing the initial vortex asymmetry. Aft blowing moved the blowing–side vortex closer to the surface of the model while the non–blowing–side vortex moved farther away from the body. It was also observed that blowing moved the separation location of the viscous layer from the body to a more leeward location.

(2)   Aft blowing was observed to be more effective at higher angles of attack than at the lower. This was due to the more effective augmentation of the axial flow component over the model as the angle of attack was increased.

(3)   Aft blowing was observed to be effective when applied at both axial locations tested, namely $x/D = 0.125$ and 0.25. The same magnitudes and trends in the C_p distributions were observed at both axial locations.

(4) Localized differences in the C_p distributions were observed as C_μ was varied. The effect of increasing the magnitude of the blowing coefficient was to move the blowing–side vortex closer to the model surface over a shorter axial distance.

(5) Low, broad nozzle cross–sectional exit geometries were observed to be more effective in reducing forebody vortex asymmetry than high, narrow cross–sections. This is consistent with the optimal conditions for the entrainment of the forebody flow by blowing, since the jet surface area is then maximum. This supports the previously proposed control mechanism of jet entrainment effects being responsible for forebody vortex control using aft blowing.

(6) For the dual blowing nozzle configuration, there apparently exists a critical jet height below which the aft blowing is most effective; in this study it was determined to be $\bar{y}/d = 0.06$. Further reductions in the mean geometric height did not provide much increased effectiveness of aft blowing.

5 Recommendations for Future Work

It is recommended that the following further studies with aft blowing be conducted:

(1) Additional rows of pressure taps located closer to the model apex than the present rows of pressure taps would be instructive in observing the development of the forebody vortices in the model apex region.

(2) Wind tunnel testing should be conducted to determine the effectiveness of aft blowing at non-zero sideslip positions.

(3) Further studies are required to confirm the validity of a critical jet height as observed in this research.

(4) Unsteady pressure measurements would provide insight into the dynamic effects of aft blowing for forebody vortex control.

(5) Dynamic testing should be conducted during model yaw, pitch, and roll to determine the effectiveness of aft blowing during aircraft maneuvers.

6 References

1. Degani, D., Schiff, L.B., and Levy, Y.,"Physical Considerations Governing Computation of Turbulent Flows Over Bodies at Large Incidence," AIAA 90-0096, January 1990.

2. Moskovitz, C.A., Hall, R.M., and DeJarnette, F.R., "Effects of Surface Perturbations on the Asymmetric Vortex Flow Over a Slender Body," AIAA 88-0483, January 1988.

3. Moskovitz, C.A., "An Experimental Investigation of the Physical Mechanisms Controlling the Asymmetric Flow Past Slender Bodies at Large Angles of Attack," Ph.D. Dissertation, North Carolina State University, Raleigh, 1989.

4. Moskovitz, C.A., Hall, R.M., and DeJarnette, F.R., "Combined Effects of Nose Bluntness and Surface Perturbations on Asymmetric Flow Past Slender Bodies," *Journal of Aircraft*, Vol. 27, October 1990, pp. 909-910.

5. Zilliac, G.G. and Degani, D., "Asymmetric Vortices on a Slender Body of Revolution," AIAA 90-0389, January 1990.

6. Hartwich, P.M., Hall R.M., and Hemsch, M.J., "Navier–Stokes Computations of Vortex Asymmetries Controlled by Small Surface Imperfections," *Journal of Spacecraft and Rockets*, Vol. 28, March–April 1991, pp. 258–264.

7. Degani, D., "Effect of Geometrical Disturbance on Vortex Asymmetry," *AIAA Journal*, Vol. 29, April 1991, pp. 560–566.

8. Ericsson, L.E., "Control of Forebody Flow Asymmetry – A Critical Review," AIAA 90–2833CP, August 1990.

9. Peake, D.J., Owen, F.K., and Johnson, D.A., "Control of Forebody Vortex Orientation to Alleviate Side Forces," AIAA 80–0183, January 1980.

10. Skow, A.M., Moore, W.A., and Lorincz, D.J., "Control of Forebody Vortex Orientation to Enhance Departure Recovery of Fighter Aircraft," *Journal of Aircraft*, Vol. 19, October 1982, pp. 812–819.

11. Malcolm, G.N. and Skow, A.M., "Enhanced Controllability Through Vortex Manipulation of Fighter Aircraft at High Angles of Attack," AIAA 86–2277CP, August 1986.

12. Malcolm, G.N., Ng., T.T., Lewis, L.C., and Murri, D.G., "Development of Non–Conventional Control Methods for High Angles of Attack Flight Using Vortex Manipulation," AIAA 89–2192CP, August 1989.

13. Rosen, B.S. and Davis, W.H., "Numerical Study of Asymmetric Air Injection to Control High Angle–of–Attack Forebody Vortices on the X–29 Aircraft," AIAA 90–3004CP, August 1990.

14. Ng, T.T. and Malcolm, G.N., "Aerodynamic Control Using Forebody Vortex Control," Extended Abstract submitted to the High Angle of Attack Technology Conference, Hampton VA, October 1990.

15. Ng, T.T. and Malcolm, G.N., "Aerodynamic Control Using Forebody Blowing and Suction," AIAA 91–0619, January 1991.

16. Cornelius, K.C., Pandit, N., Osborn, R.F., and Guyton, R.W., "An Experimental Study of Pneumatic Vortex Flow Control on High Angle of Attack Forebody Model," AIAA 92–0018, January 1992.

17. Guyton, R.W. and Maerki, G., "X–29 Forebody Jet Blowing," AIAA 92–0017, January 1992.

18. LeMay, S.P., Sewall, W.G., and Henderson, J.F., "Forebody Vortex Flow Control on the F–16C Using Tangential Slot and Jet Nozzle Blowing," AIAA 92–0019, January 1992.

19. Ng, T.T., Ong, L.Y., Suarez, C.J., and Malcolm, G.N., "Wing Rock Suppression Using Forebody Vortex Control," AIAA 91–3227CP, September 1991.

20. Gittner, N.M. and Chokani, N., "An Experimental Study of the Effects of Aft Blowing on a 3.0 Caliber Tangent Ogive Body at High Angles of Attack," AIAA 91–3252CP, September 1991.

7 Appendix

A method of calibrating the blowing nozzles was developed to determine the level of blowing. A simple calibration apparatus, shown in Figure A1, was assembled for this purpose. It consisted of a pressure regulator used to vary the plenum stagnation pressure; a pressure transducer to measure the plenum pressure; and an in-line flow meter positioned between the plenum and the blowing nozzle to measure the volumetric flow rate of the jet. Prior to the nozzle calibration, the pressure drop across the flow meter was measured, and was observed]to be negligible. Each section of tubing used in the calibration procedure was of the same length as that used during the subsequent wind tunnel testing.

From the calibration apparatus, the stagnation pressure and volumetric flow rate were measured while the stagnation temperature was taken to be the ambient laboratory temperature. By use of the definitions of perfect gas ($P = \rho R T$) and mass flow rate ($\dot{m} = \rho u A$), and the isentropic pressure and temperature relation ($PT^{1/\gamma} = \text{constant}$), it can be shown that:

$$\dot{m}_j = \frac{P_o \dot{V}}{RT_o} \left[1 - \frac{\gamma - 1}{2\gamma RT_o} \left(\frac{\dot{V}}{A_{fm}} \right)^2 \right]^{\frac{1}{\gamma - 1}} \tag{7.1}$$

The blowing nozzles were designed to be choked at the nozzle exit plane, thus the

nozzle exit velocity, u_j, can be calculated as the sonic velocity:

$$u_j = \sqrt{\frac{2\gamma R T_o}{\gamma + 1}} \tag{7.2}$$

The blowing coefficient, C_μ, was then calculated from:

$$C_\mu = \frac{\dot{m}_j u_j}{q_\infty A_{ref}} \tag{7.3}$$

where A_{ref} was taken to be $40(\pi D^2/4)$. This reference area was chosen to enable comparison of the blowing coefficient with previous researches.

Figure A2 shows the calibration curves for the blowing nozzles of group A. Nozzles 1 and 2 provided almost identical levels of blowing for a given supply pressure. The range of C_μ's for these blowing nozzles was 0.007 to 0.028. Blowing nozzle 3 was designed to provide a lower range of C_μ's. For this nozzle, the blowing range was 0.003 to 0.015. Figure A3 shows the calibration curves for blowing nozzles 4 – 8. These blowing nozzles exhibited different magnitudes of blowing at a given supply pressure. It is thought that these differences are due to the different nozzle exit geometries. Each blowing nozzle has its own range of attainable C_μ's, but as shown by the shaded bar line, the range of C_μ's common to all 5 blowing nozzles is 0.009 to 0.024. The use of these calibration curves enabled the desired C_μ to be determined from the applied supply pressure.

Exit to Atmosphere

Flowmeter

To Pressure Transducer

Plenum

High Pressure Air
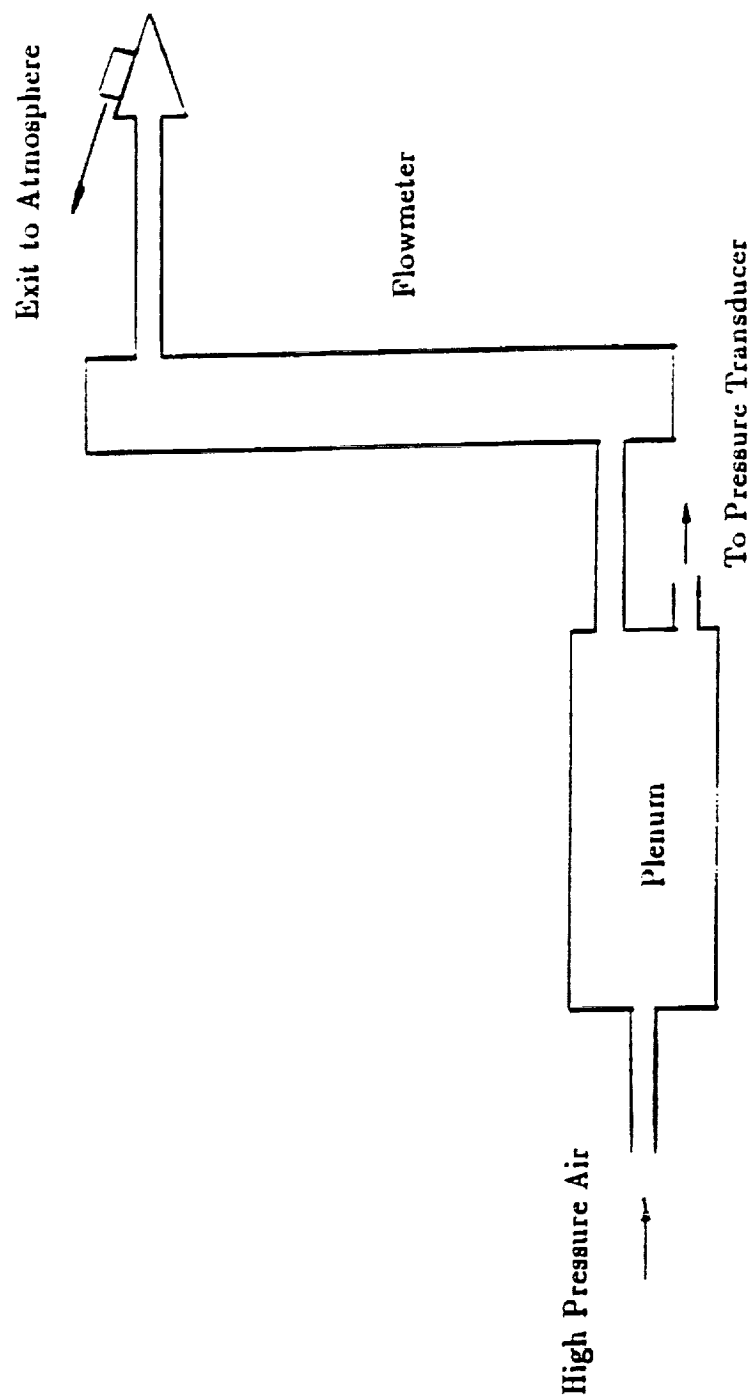
Figure A1 – Blowing Nozzle Calibration Test Schematic
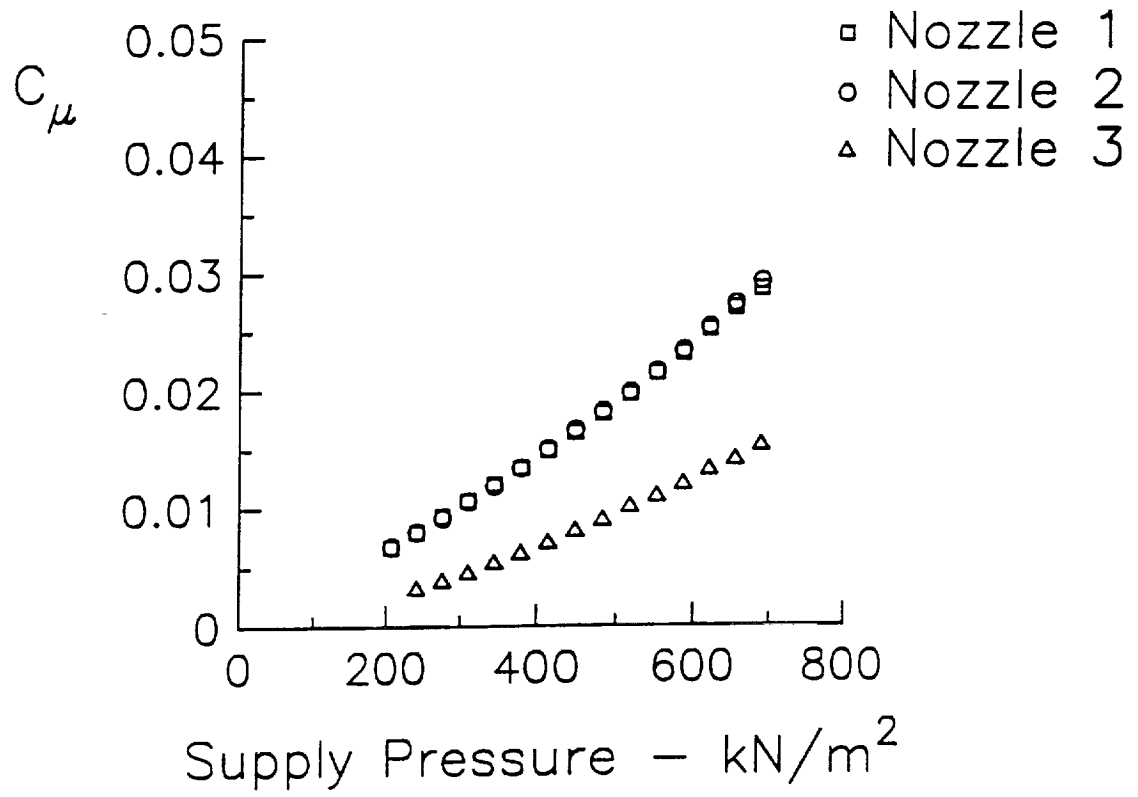
Figure A2 – Nozzle Calibration Curves
Group A Nozzles
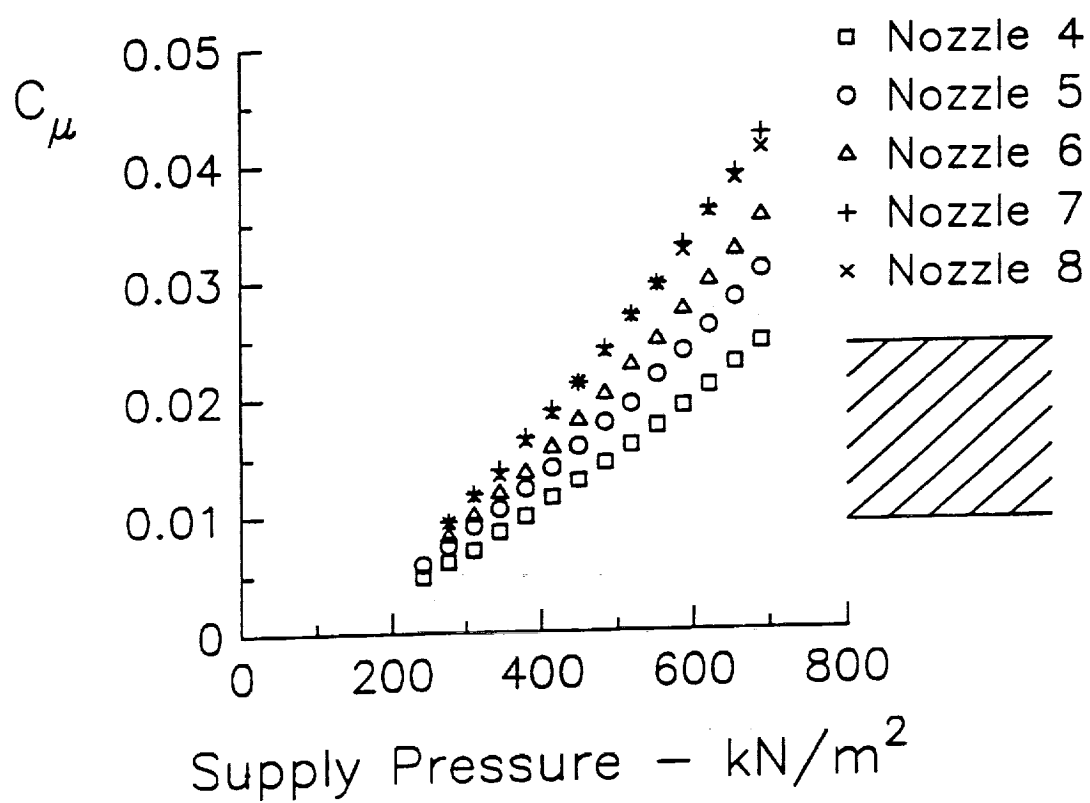
Figure A3 – Nozzle Calibration Curves
Group B Nozzles

Tables
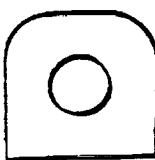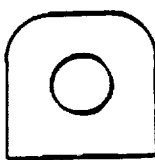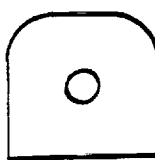
Blowing Nozzle	Exit Geometries	x/D
1		0.125
2		0.250
3		0.125

Table 1 – Group A Blowing Nozzles
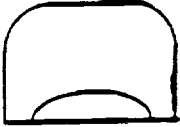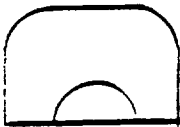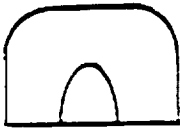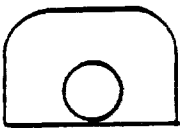
Blowing Nozzle	Exit Geometries	x/D	$\overline{y}/d$	z_{max}/d
4		0.125	0.0354	0.334
5		0.125	0.0499	0.235
6		0.125	0.0588	0.235
7		0.125	0.0627	0.167
8		0.125	0.0836	0.167

Table 2 – Group B Blowing Nozzles

Figures

(i) No Vortices

$V_\infty sin(\alpha)$

(ii) Symmetric Vortices

$V_\infty sin(\alpha)$

(iii) Asymmetric Vortices

Increasing Angle of Attack

$V_\infty sin(\alpha)$

(iv) Vortex Wake

$V_\infty sin(\alpha)$
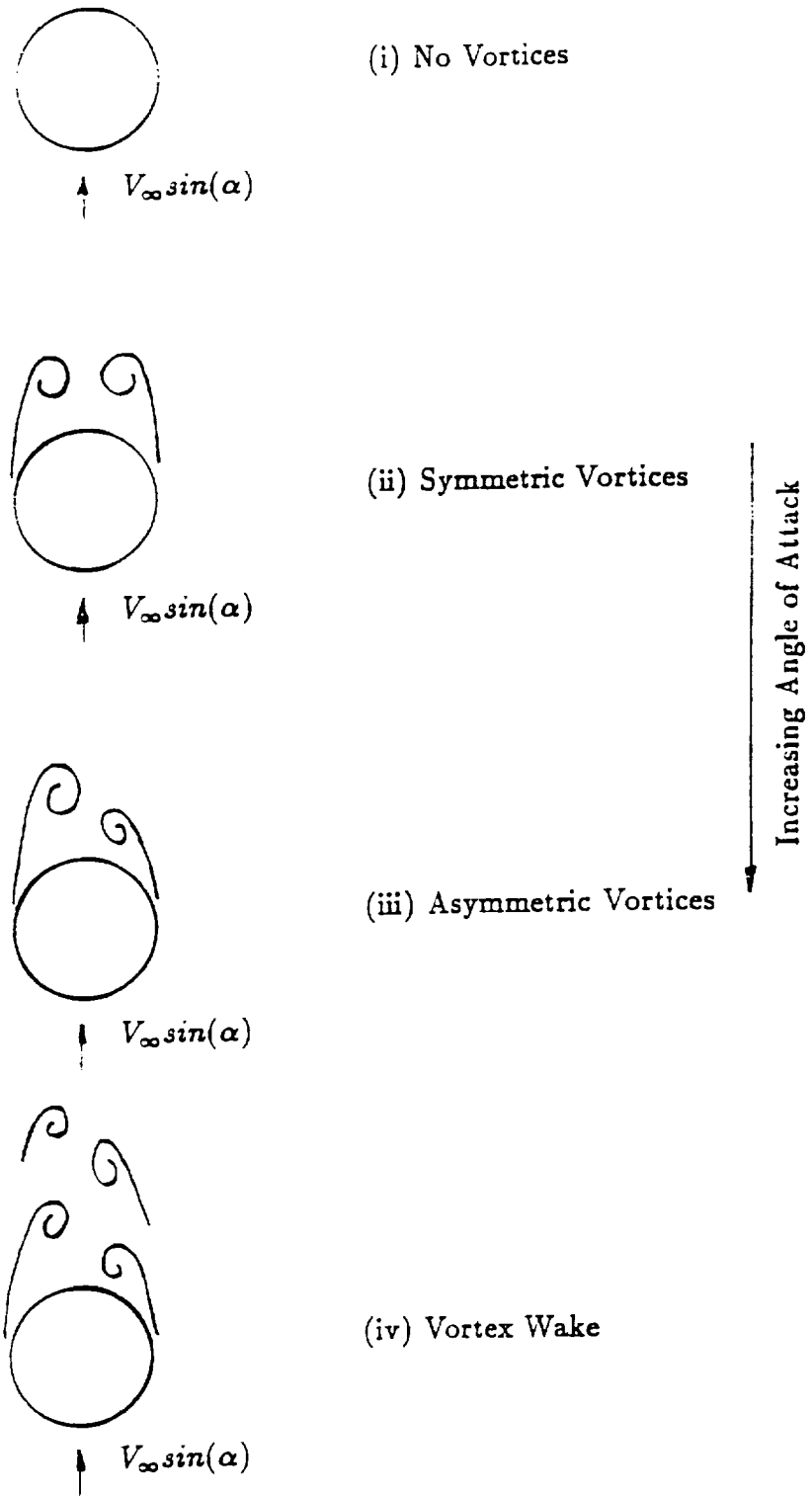
Figure 1 – Various Leeside Flowfields
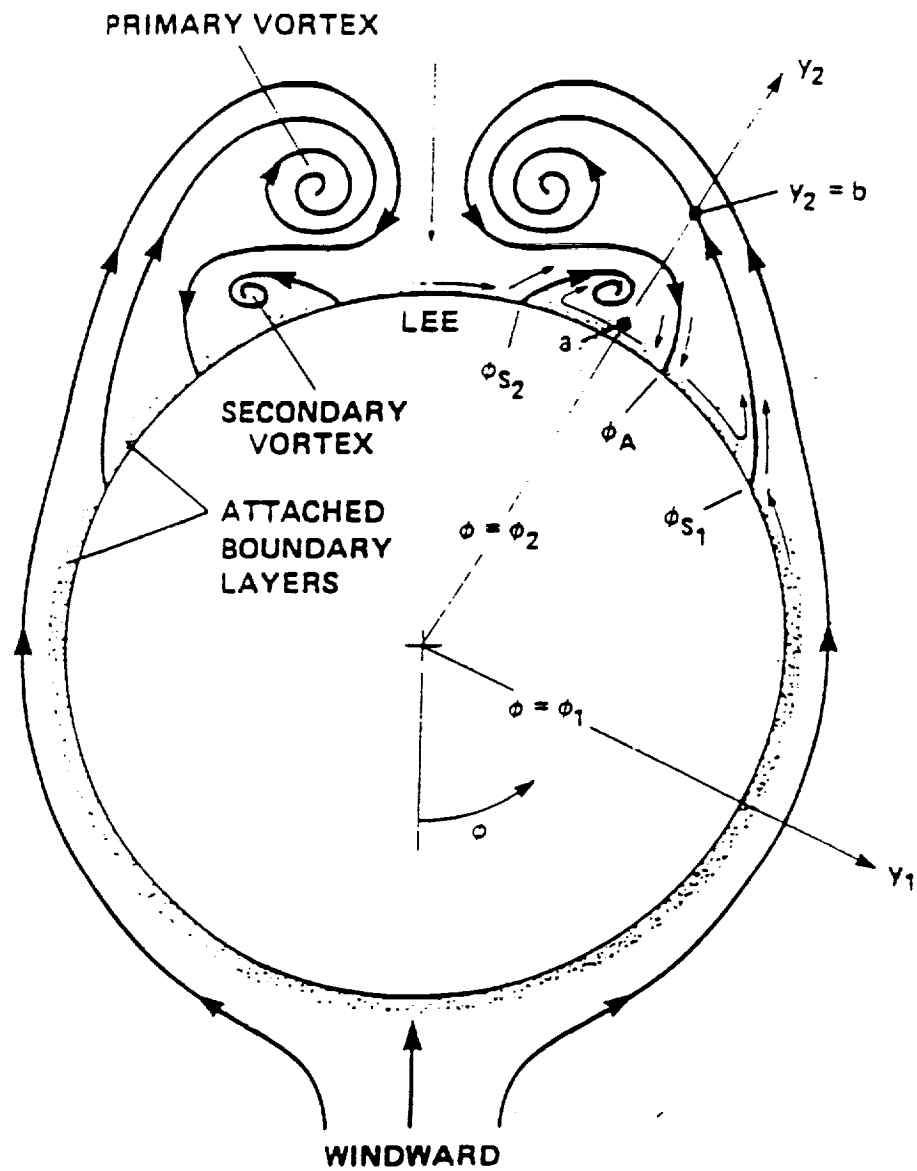
Figure 2 – Cross–Section Flow Structure (ref. 1)
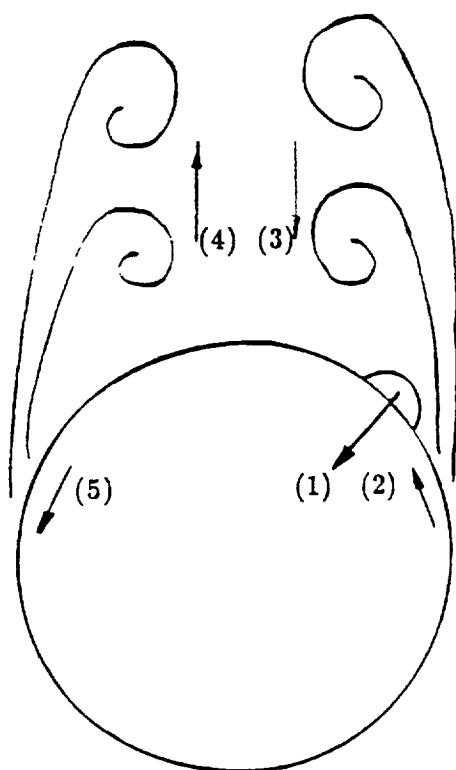
(1) Blowing is initiated.
(2) Separation is moved leeward due to entrainment.
(3) Blowing–side vortex moves towards body.
(4) Non–blowing side vortex moves away from body.
(5) Separation is moved windward.

Figure 3 – Effects of Aft Blowing on the Leeside Vortices (ref. 15)
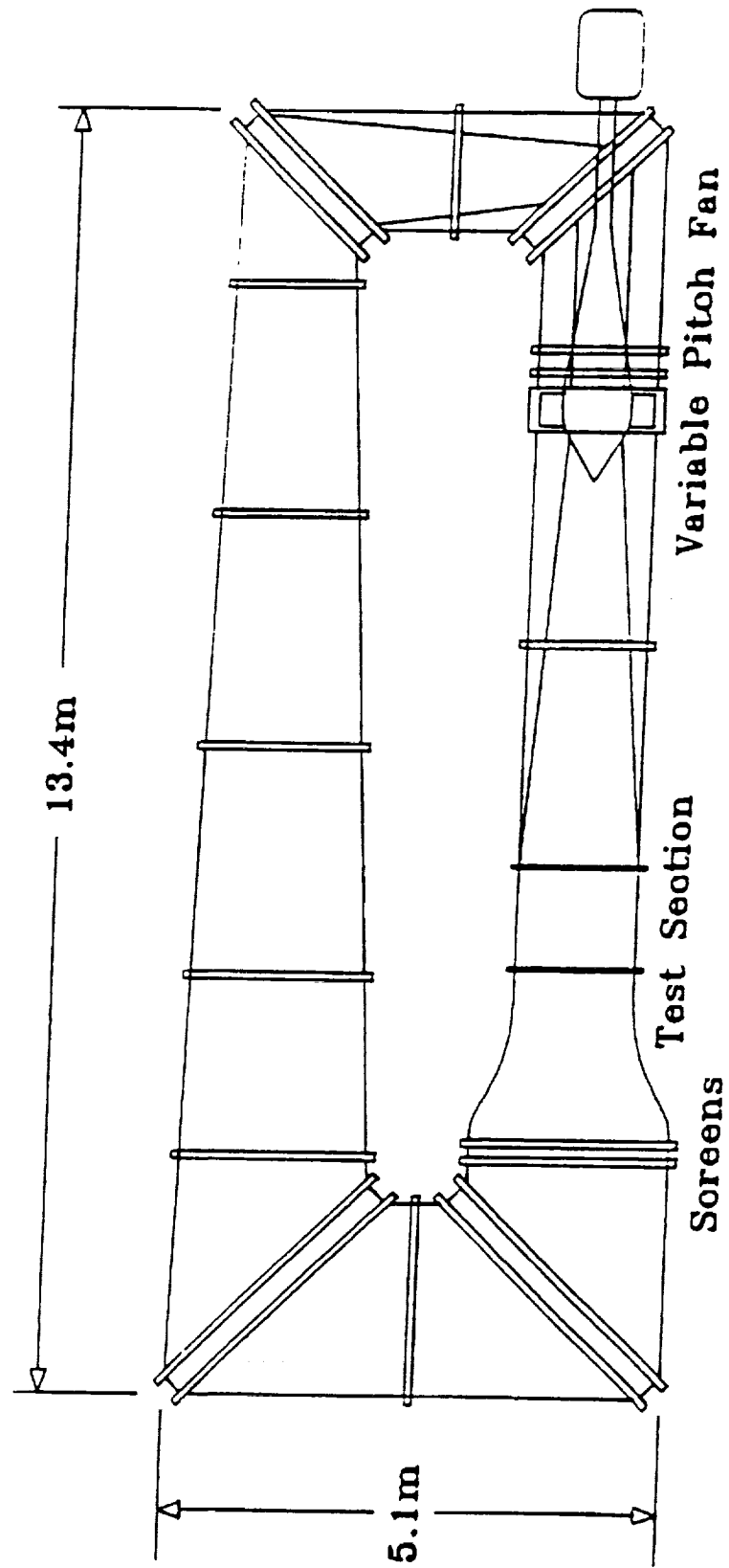
Figure 4 – North Carolina State University Subsonic Wind Tunnel
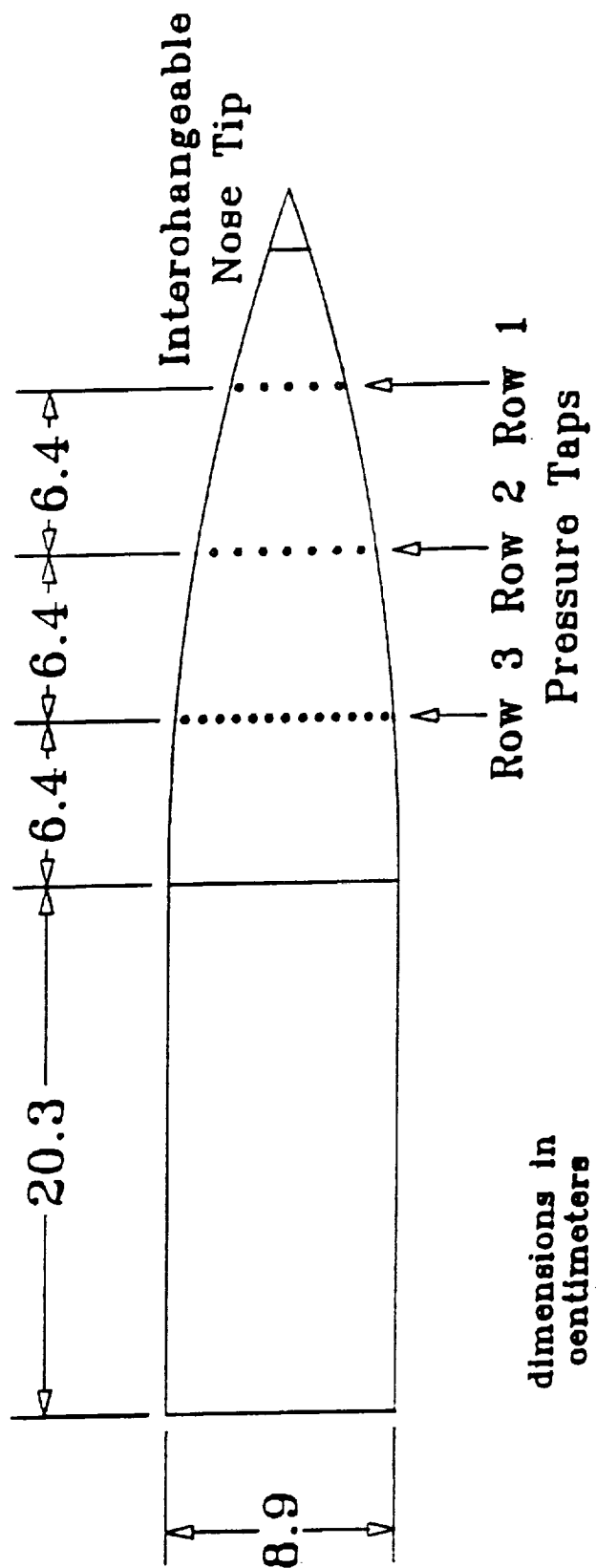
Figure 5 – 3.0 Caliber Tangent Ogive Model

1.11

1.90

0.159

1.52

To Plenum

dimensions in
centimeters
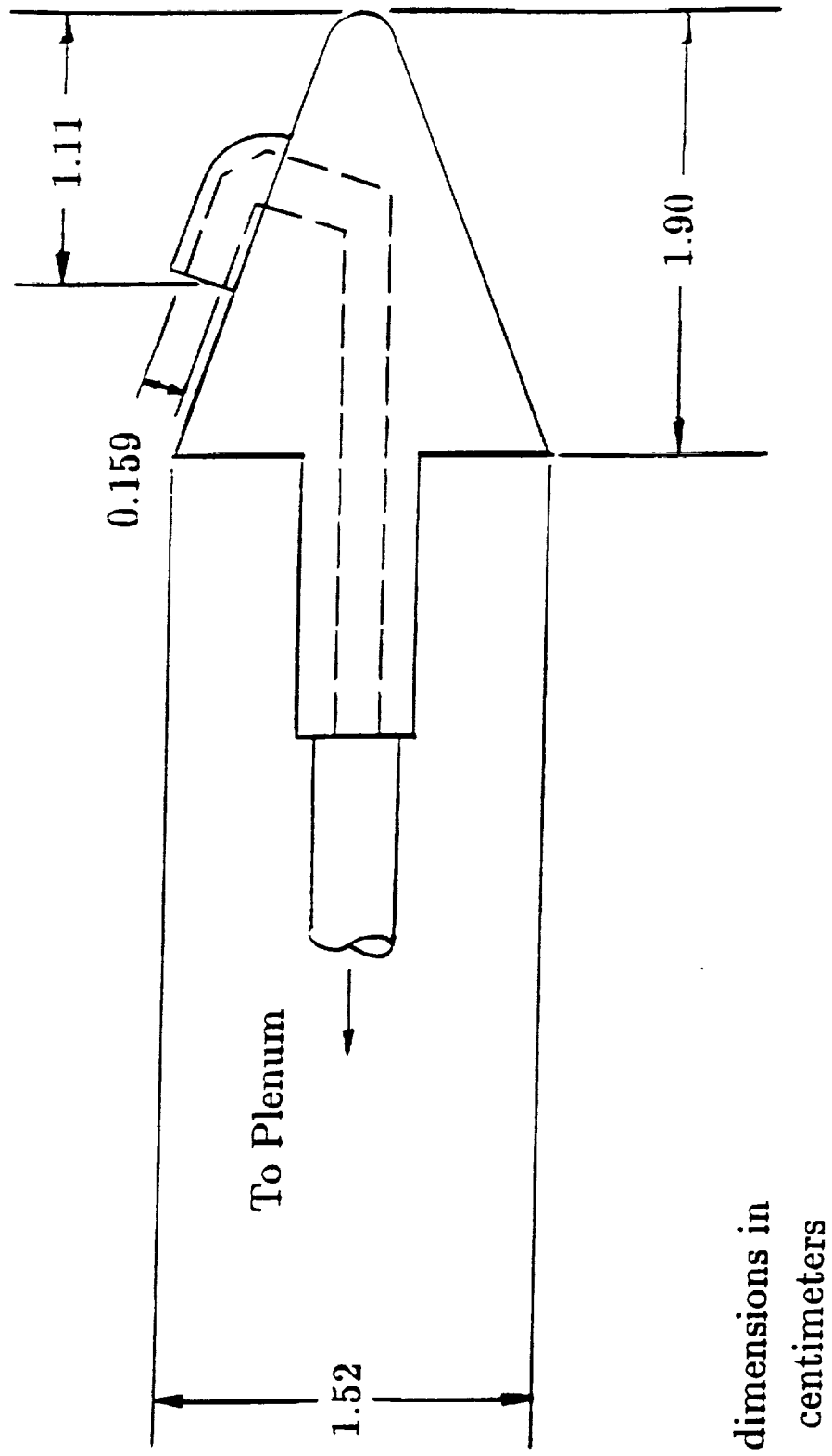
Figure 6 – Removable Nose Tip with Blowing Nozzle 1
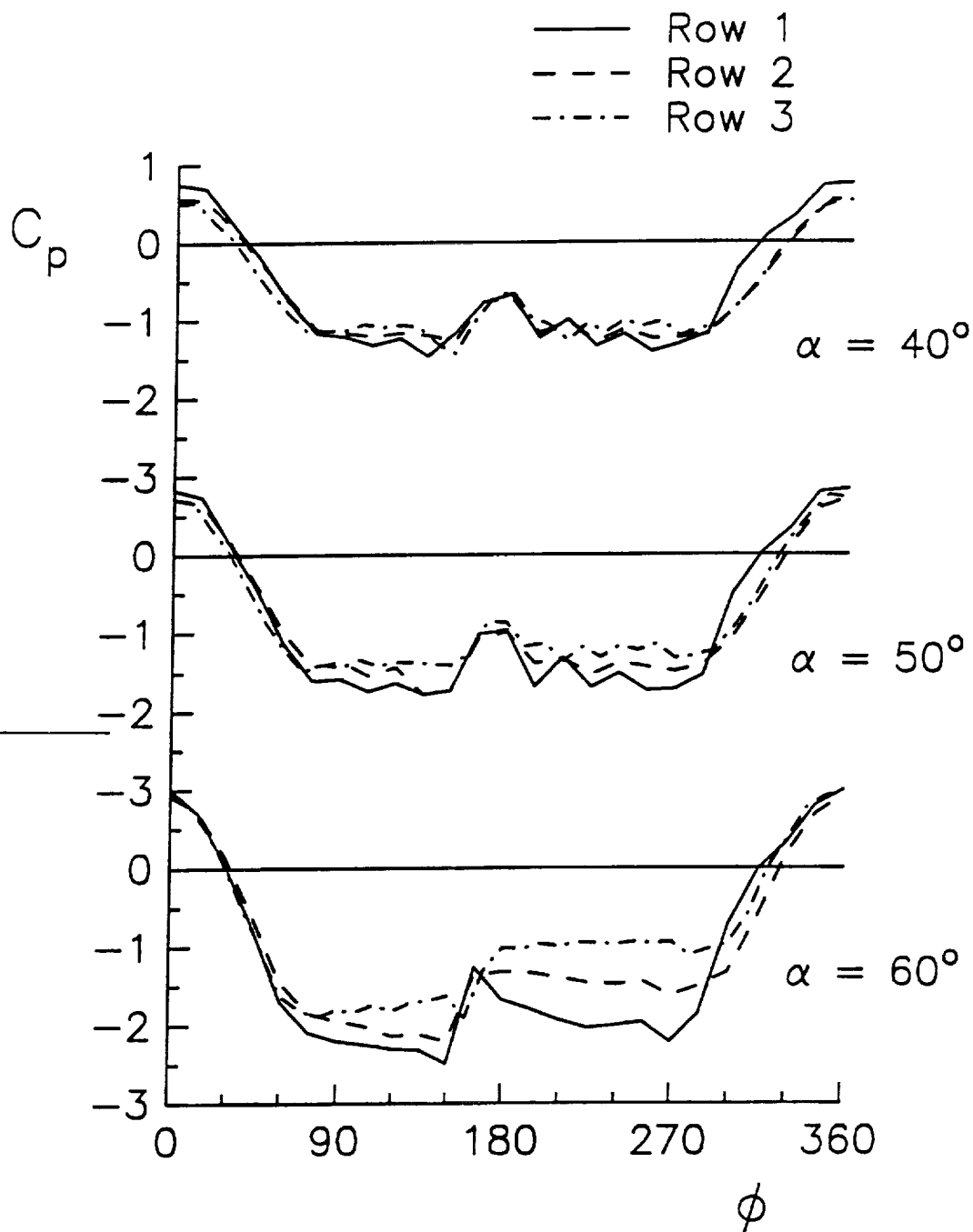
Figure 7 – Pressure Coefficient Distributions
"Clean" Model – $\phi_m = 120°$
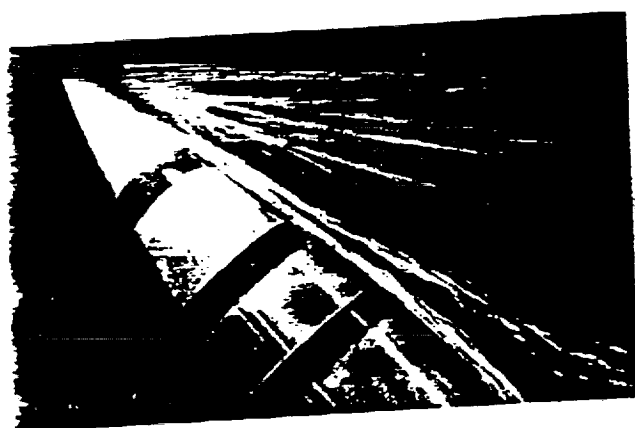
$\alpha = 40°$

$\alpha = 50°$
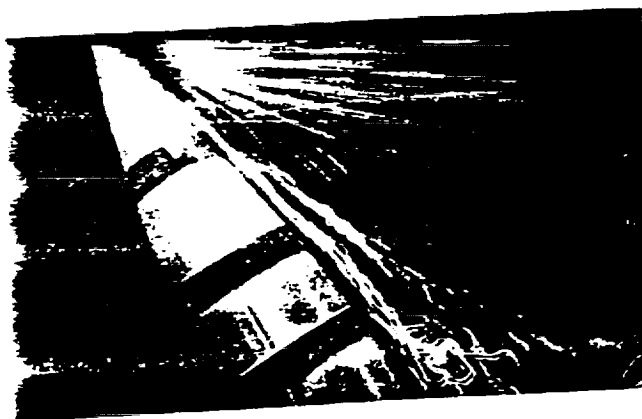
$\alpha = 60°$

Figure 8 – Side View Flow Visualization
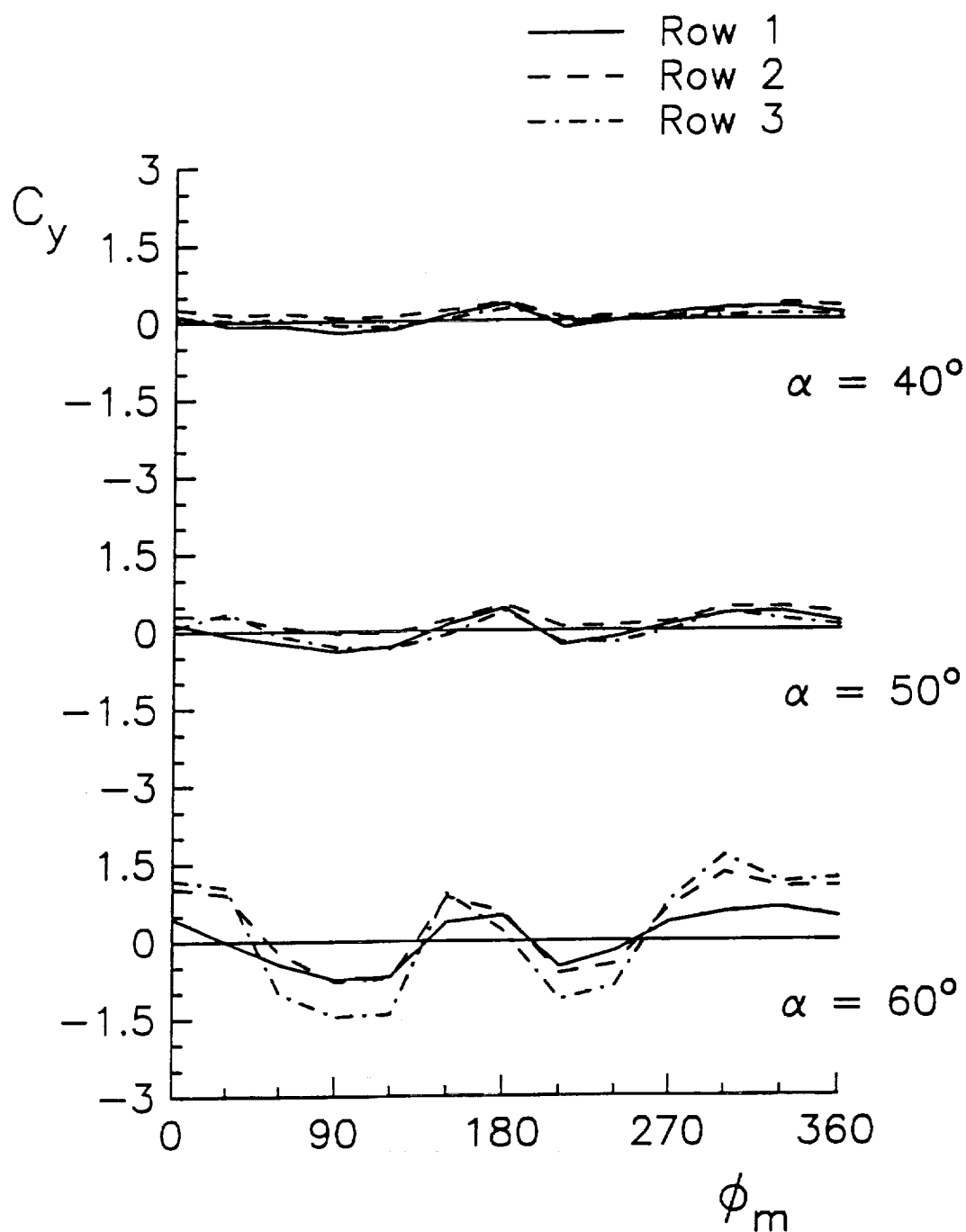
Figure 9 – Sectional Side Force Coefficient Plots
"Clean" Model
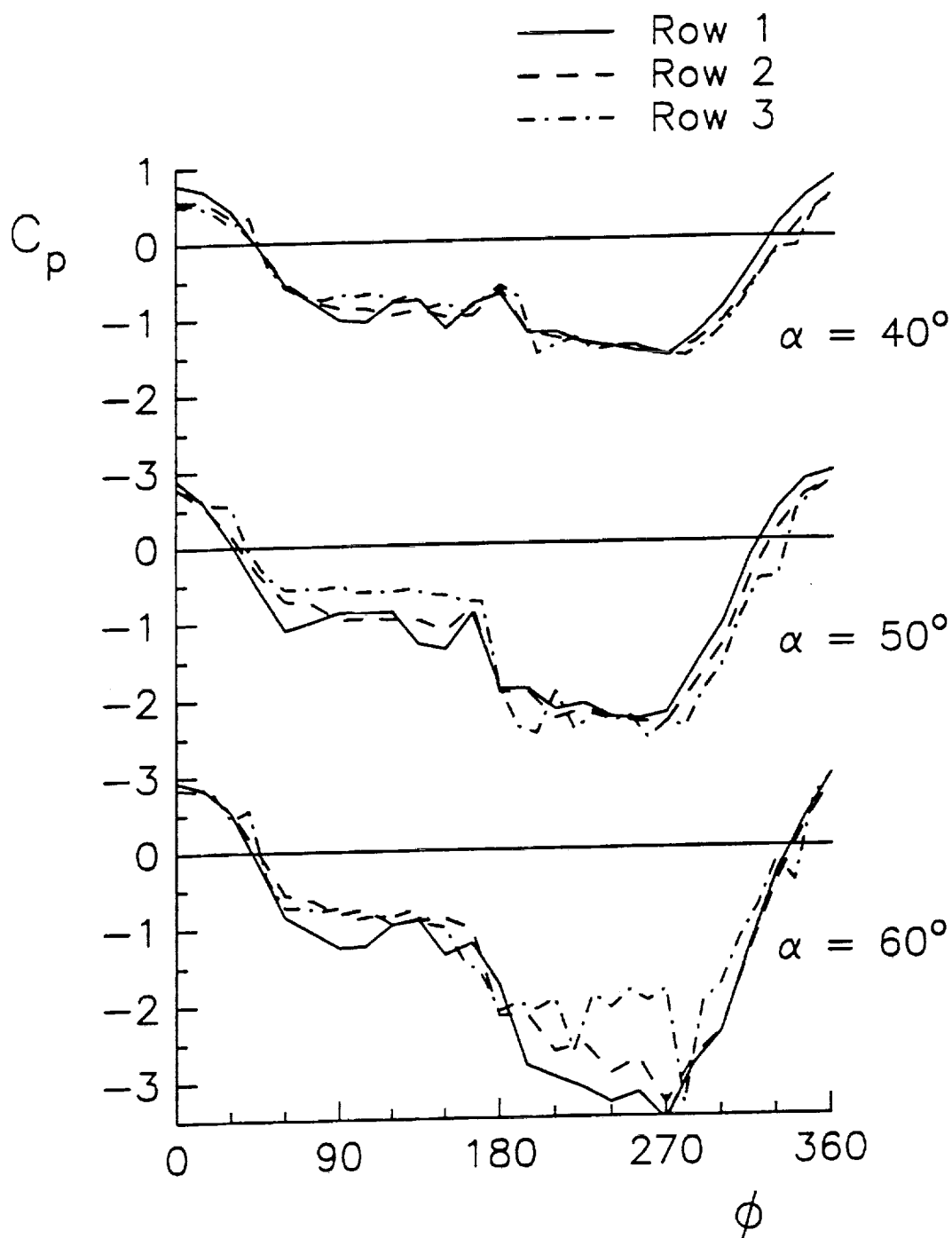
Figure 10 – "Baseline" Pressure Coefficient Distributions
Nozzle 1, $\phi_j = 120°$, $C_\mu = 0$
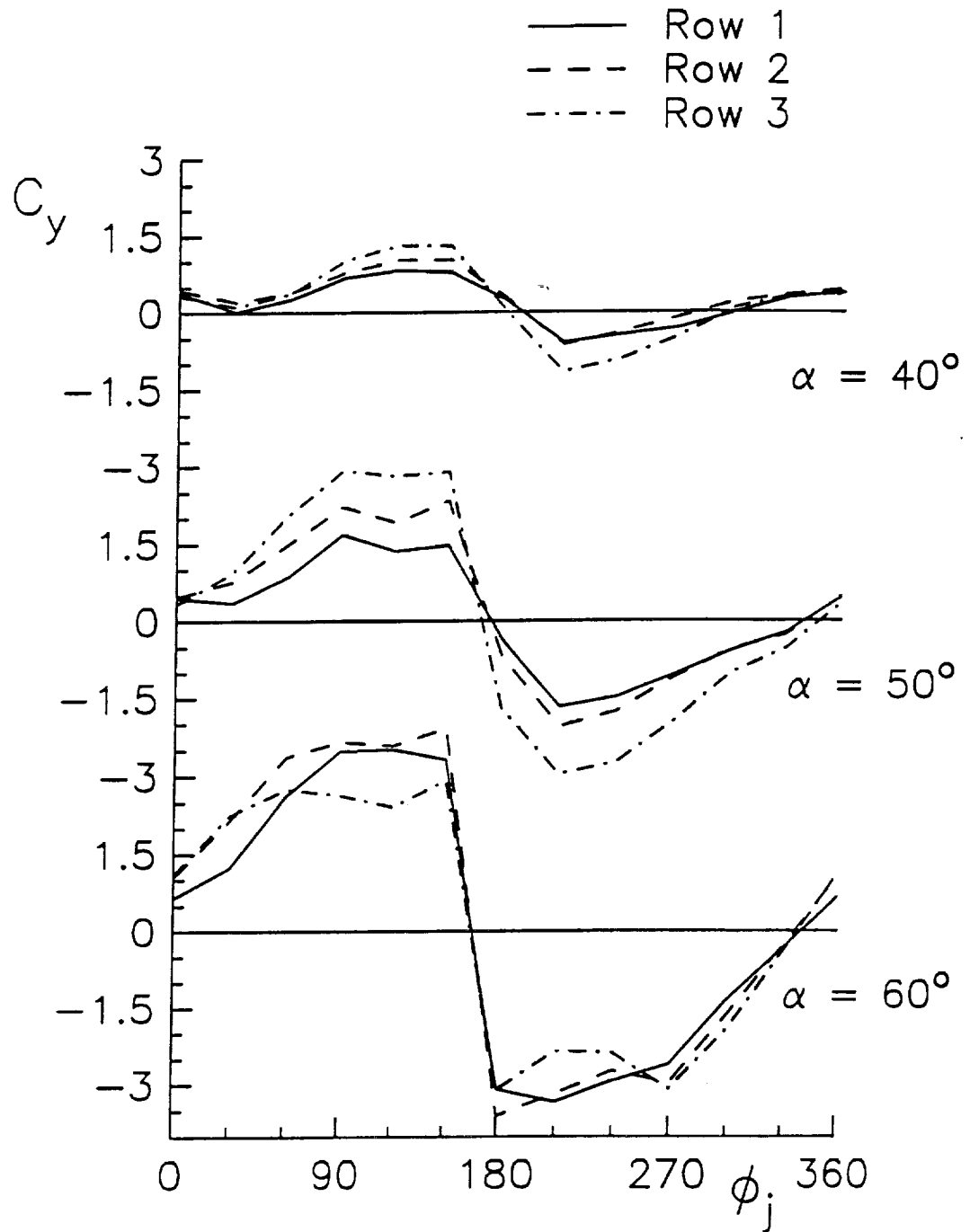
Figure 11 – "Baseline" Sectional Side Force Coefficient Plots
Nozzle 1, $C_\mu = 0$
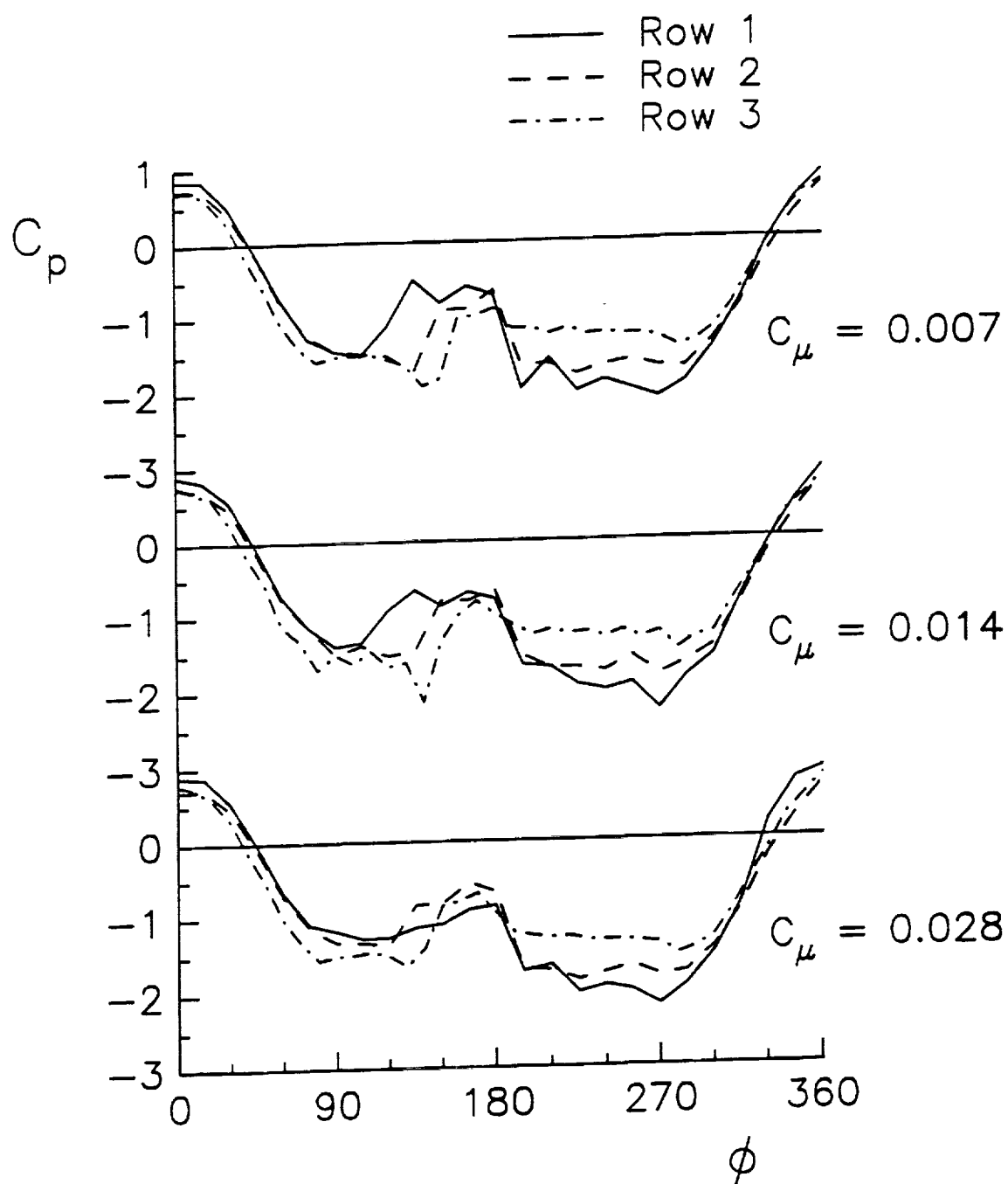
Figure 12 – Pressure Coefficient Distributions
Nozzle 1, $\alpha = 50°$, $\phi_j = 120°$

$C_\mu = 0$

$C_\mu = 0.007$

$C_\mu = 0.014$

$C_\mu = 0.028$

Row 2   Row 3
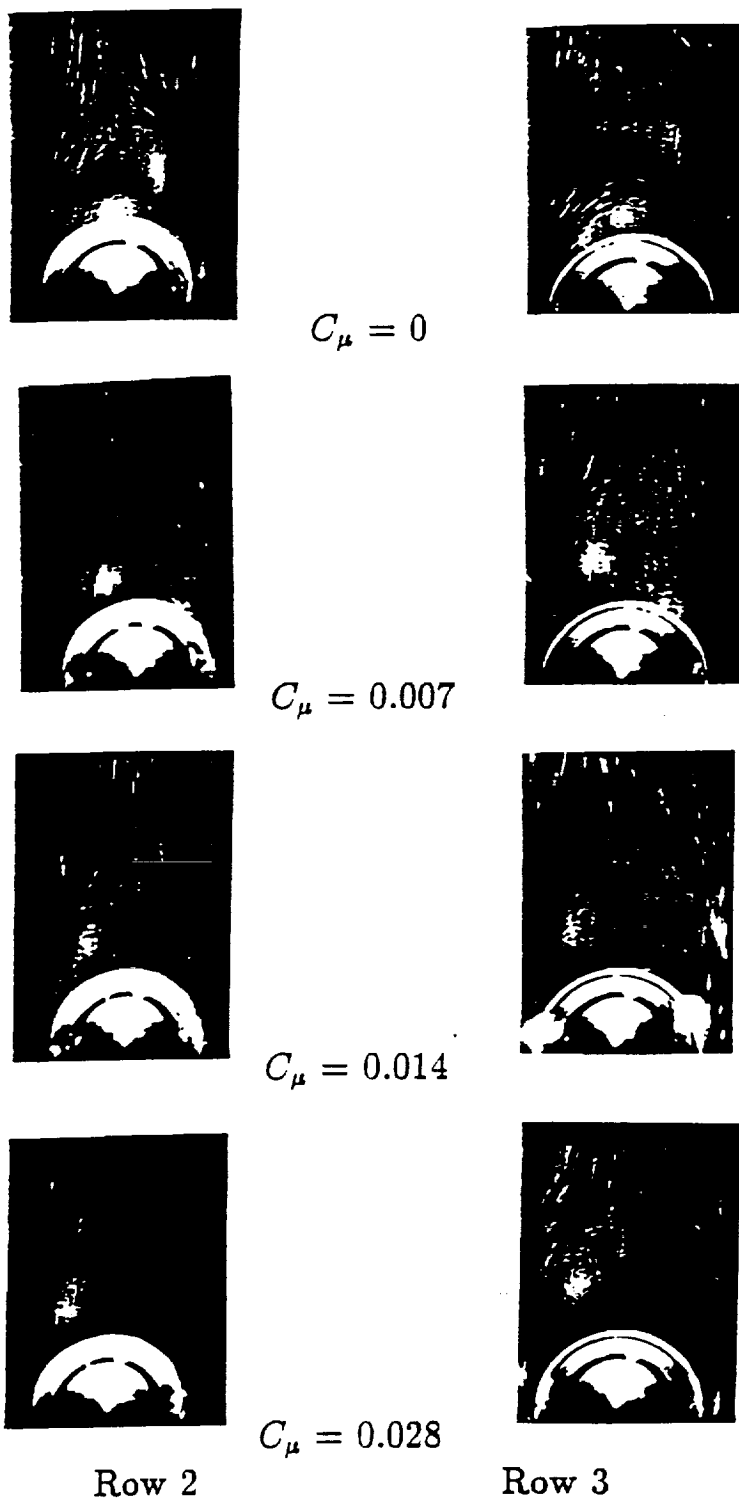
Figure 13 – Cross–Sectional Flow Visualization
Nozzle 1, $\alpha = 50°$, $\phi_j = 120°$
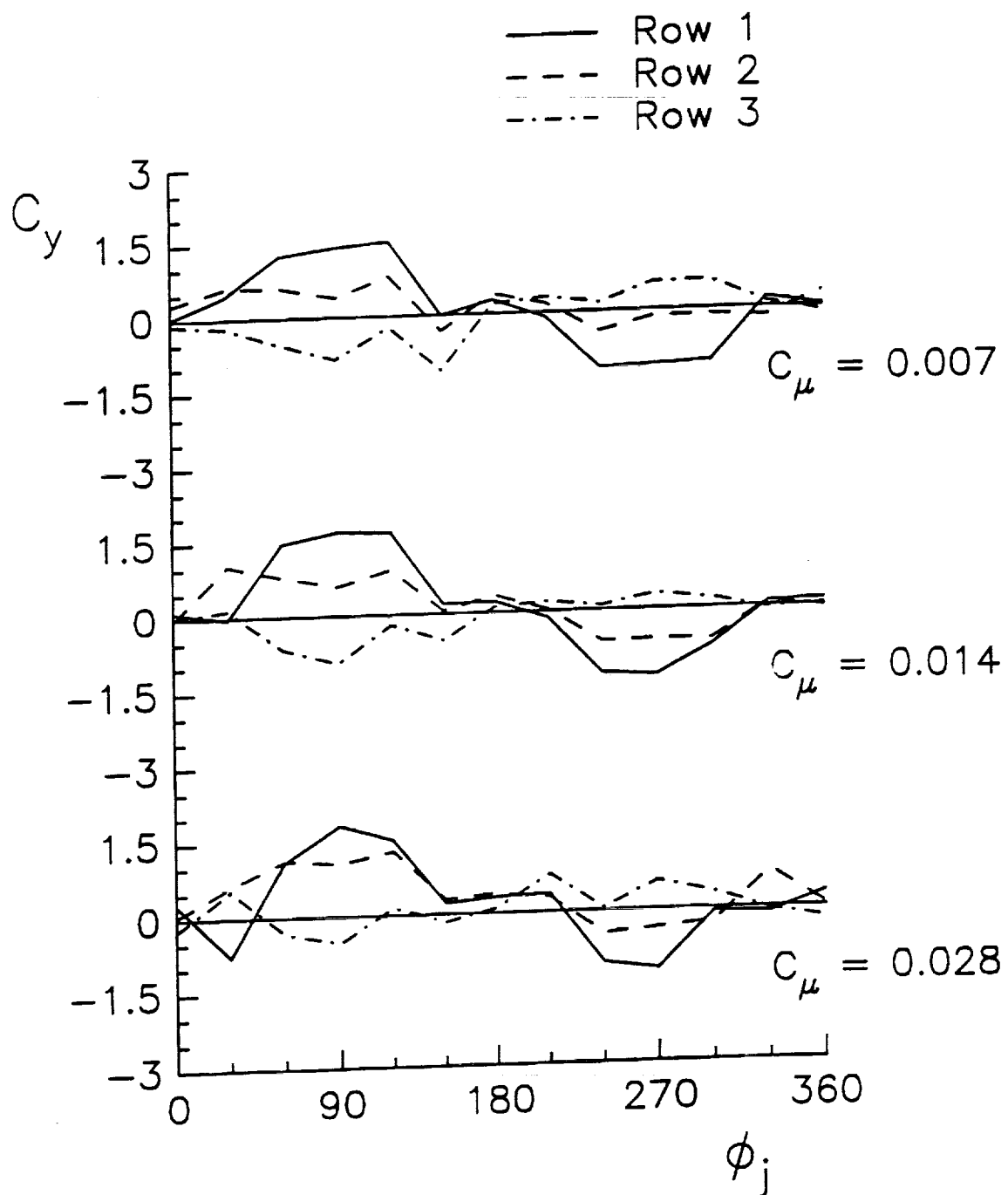
Figure 14 – Sectional Side Force Coefficient Plots
Nozzle 1, $\alpha = 50°$
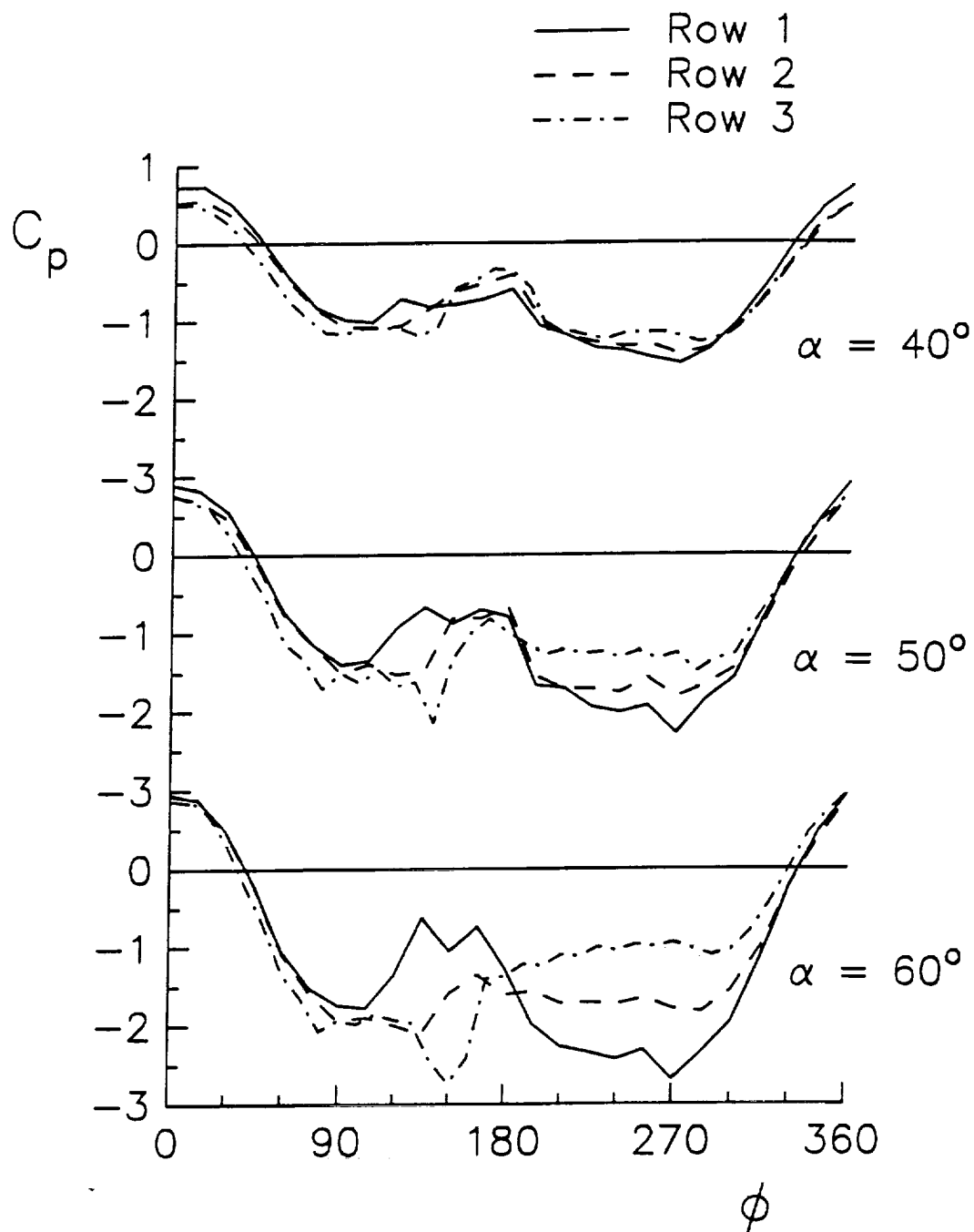
Figure 15 – Pressure Coefficient Distributions
Nozzle 1, $\phi_j = 120°$, $C_\mu = 0.014$
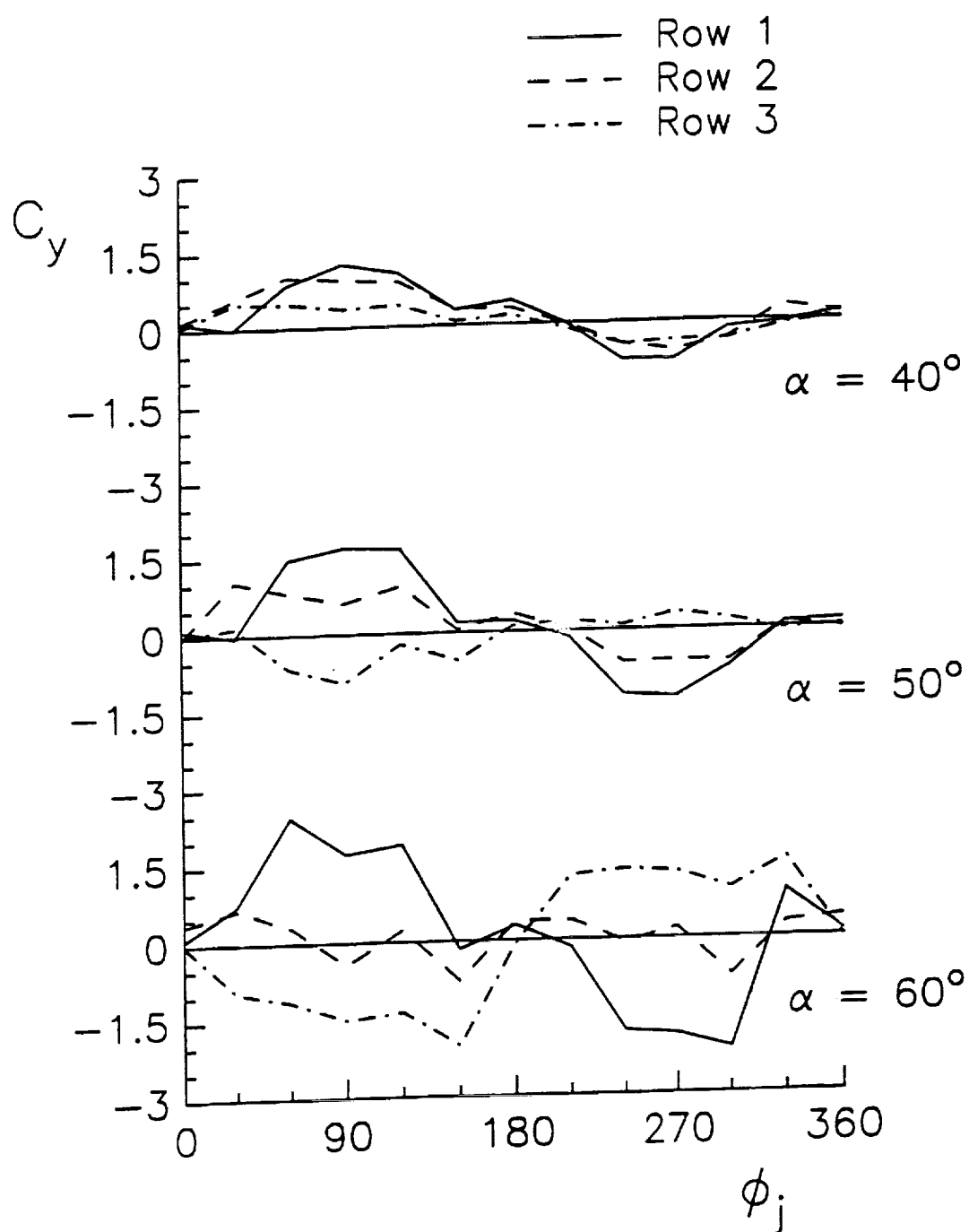
Figure 16 – Sectional Side Force Coefficient Plots
Nozzle 1, $C_\mu = 0.014$
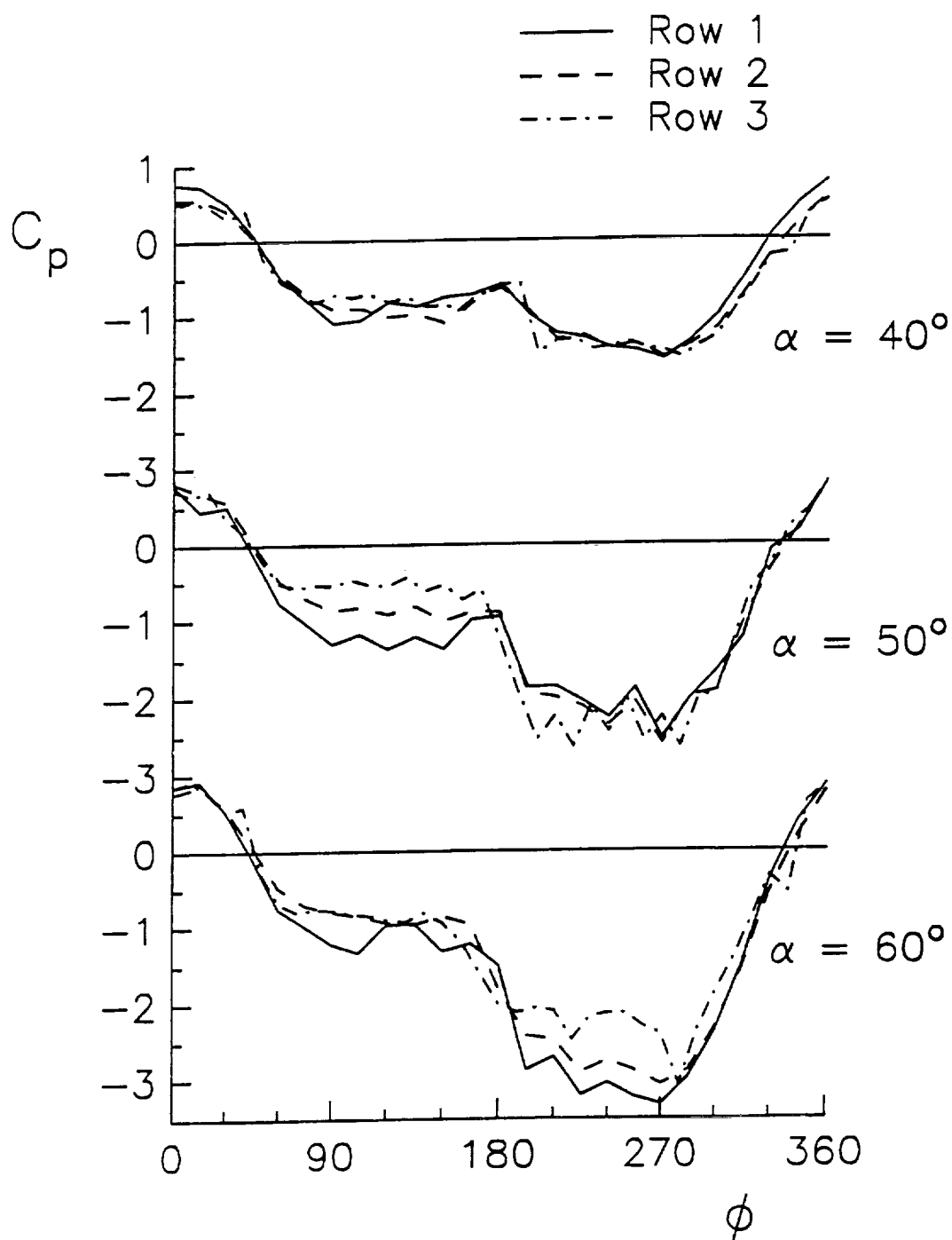
Figure 17 – "Baseline" Pressure Coefficient Distributions
Nozzle 2, $\phi_j = 120°$, $C_\mu = 0$
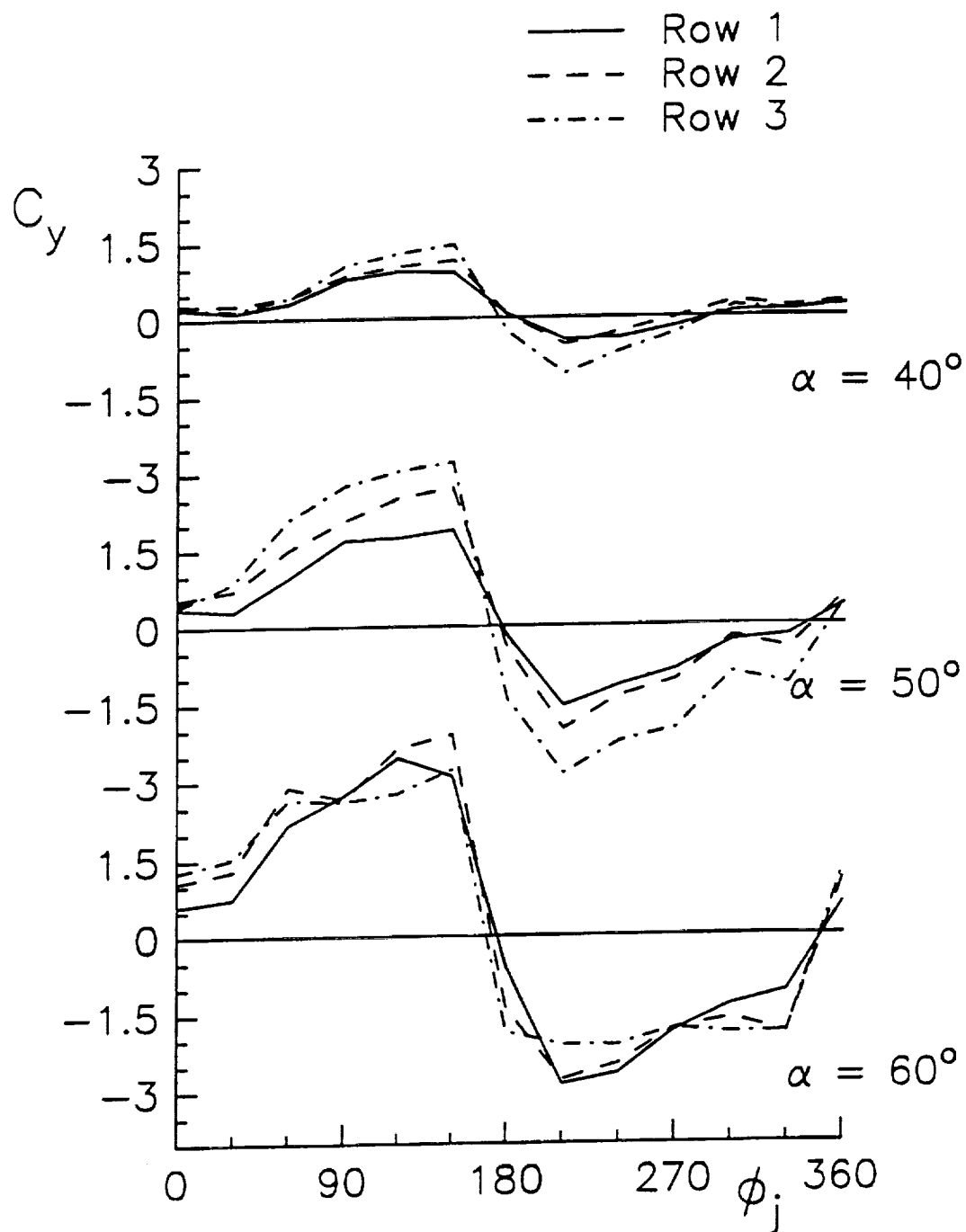
Figure 18 – "Baseline" Sectional Side Force Coefficient Plots
Nozzle 2, $C_\mu = 0$
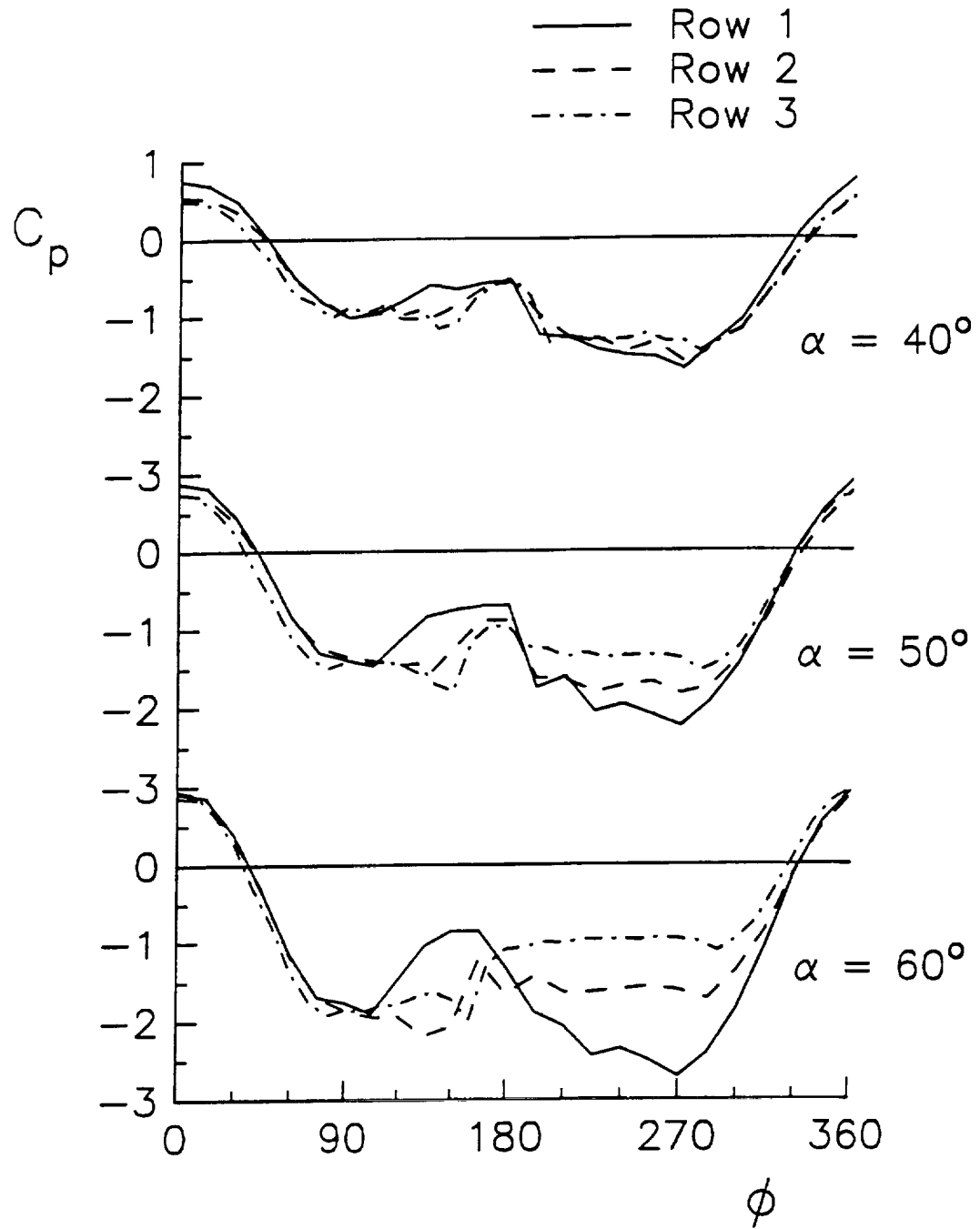
Figure 19 – Pressure Coefficient Distributions
Nozzle 2, $\phi_j = 120°$, $C_\mu = 0.007$
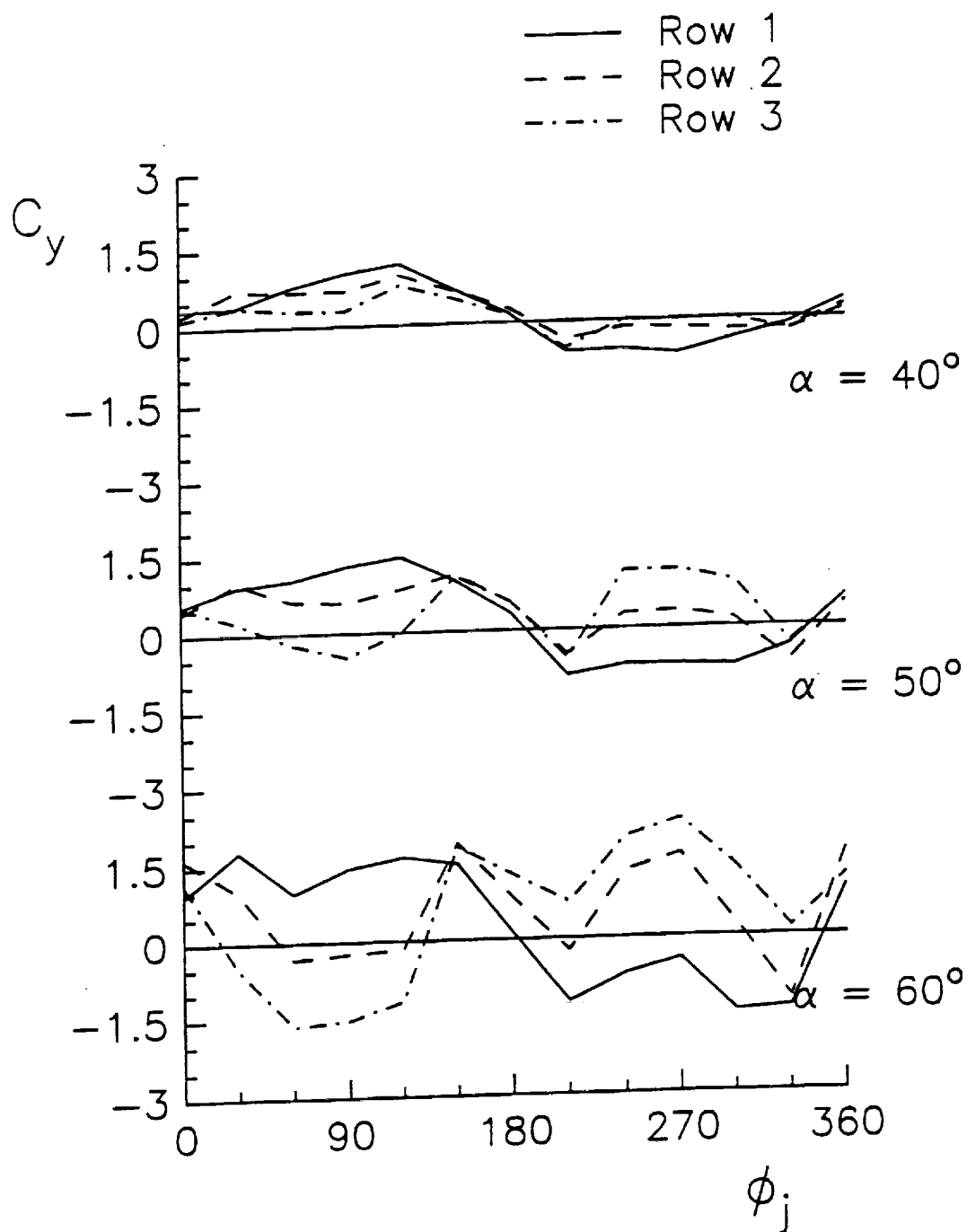
Figure 20 – Sectional Side Force Coefficient Plots
Nozzle 2, $C_\mu = 0.007$
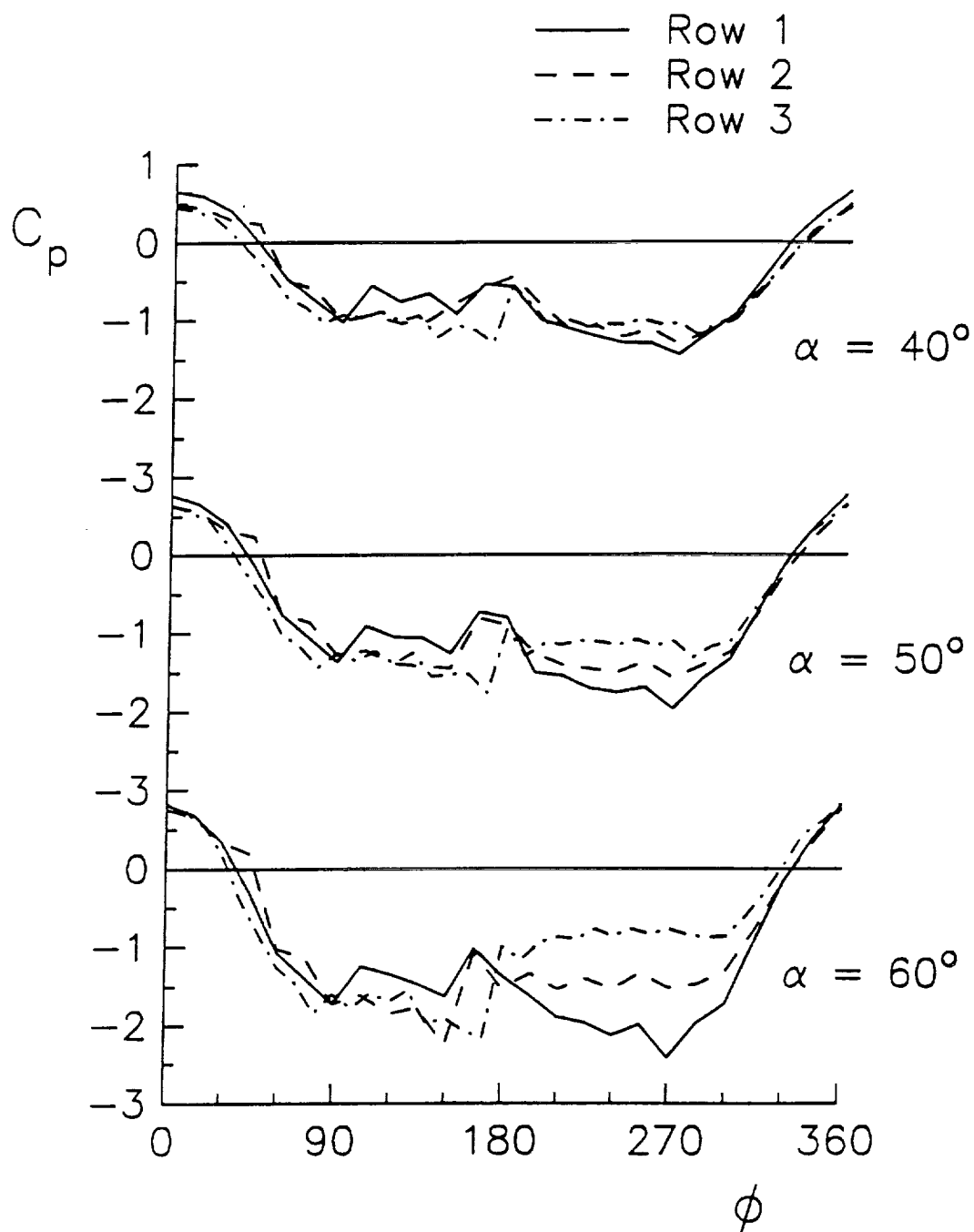
Figure 21 – Pressure Coefficient Distributions
Nozzle 3, $\phi_j = 120°$, $C_\mu = 0.0035$
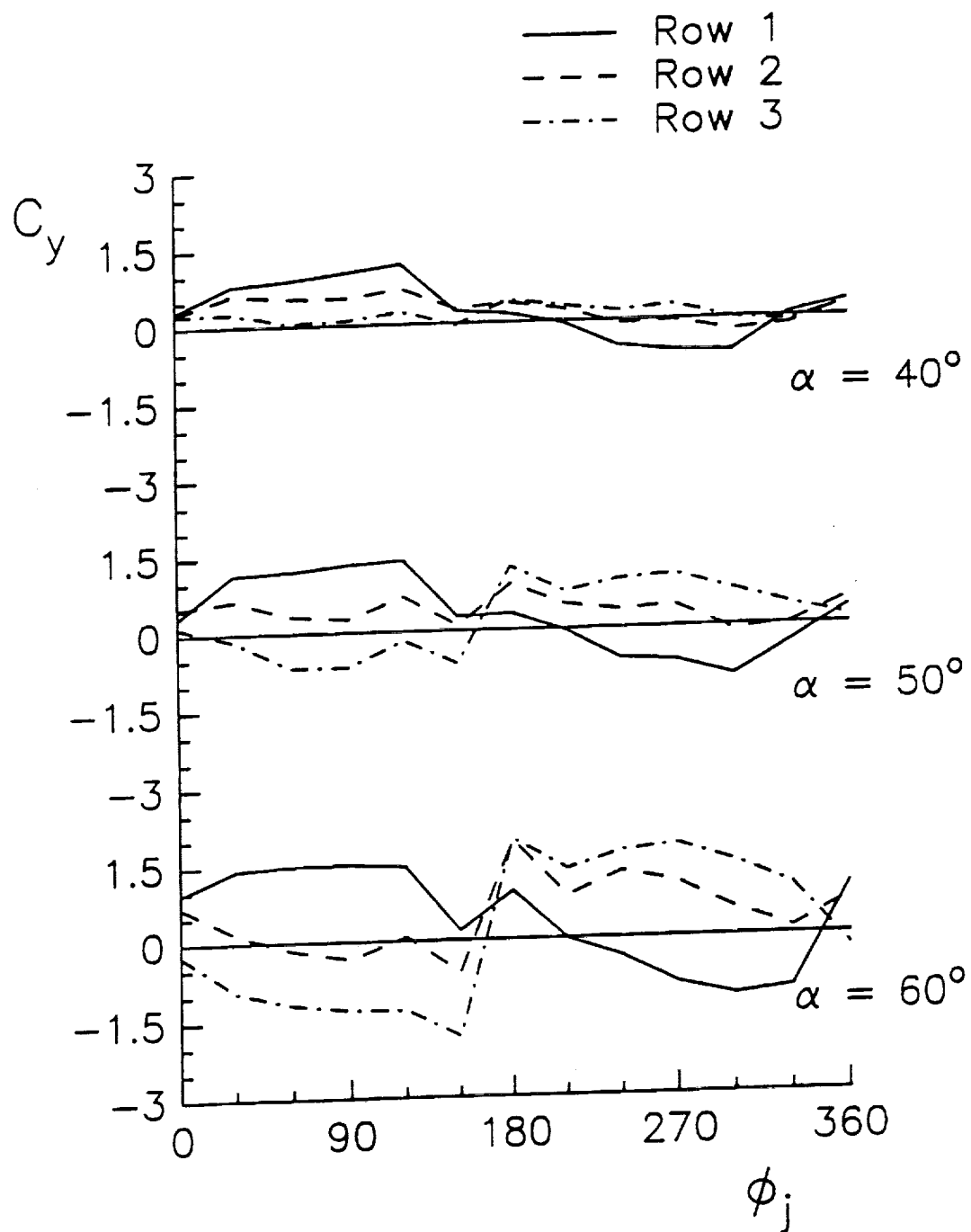
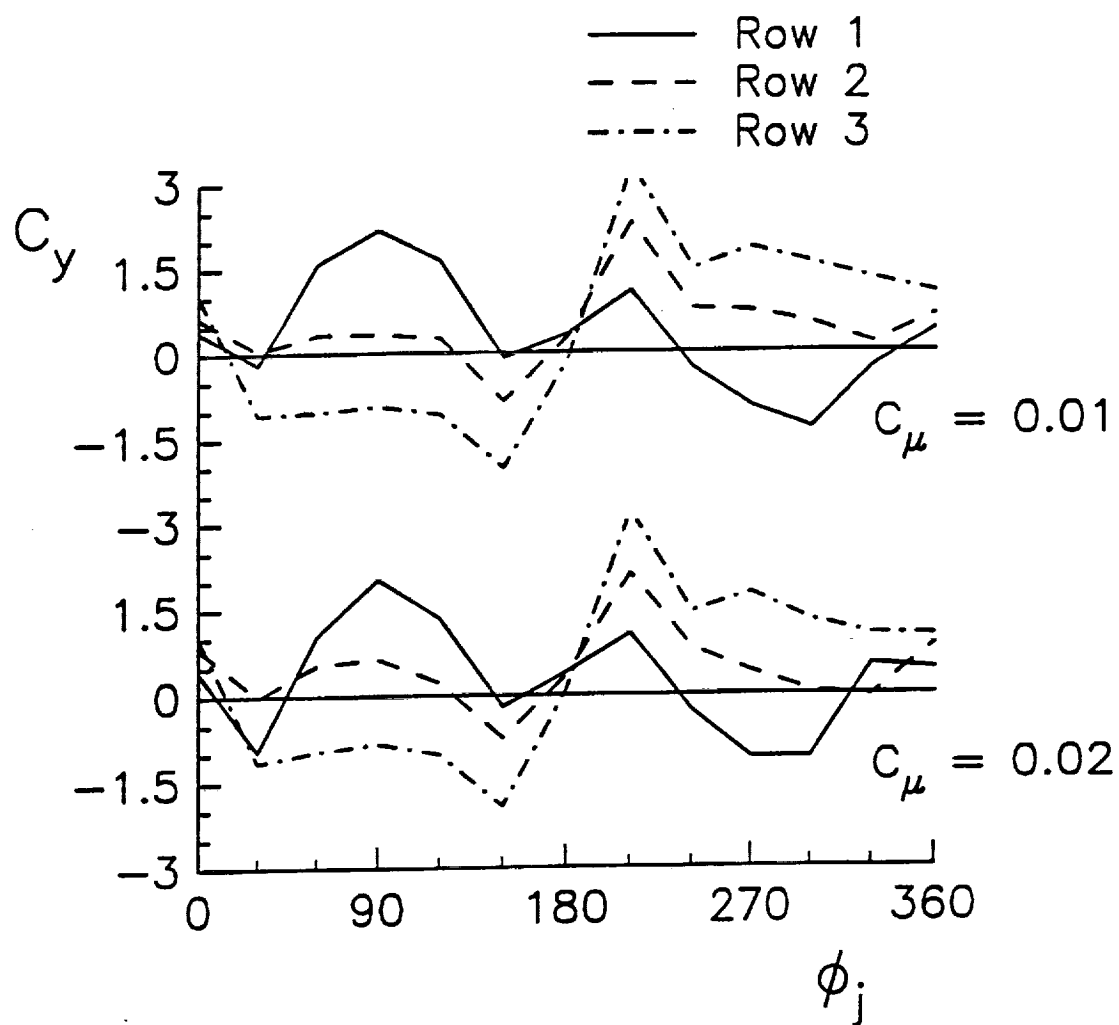Figure 22 – Sectional Side Force Coefficient Plots
Nozzle 3, $C_\mu = 0.0035$
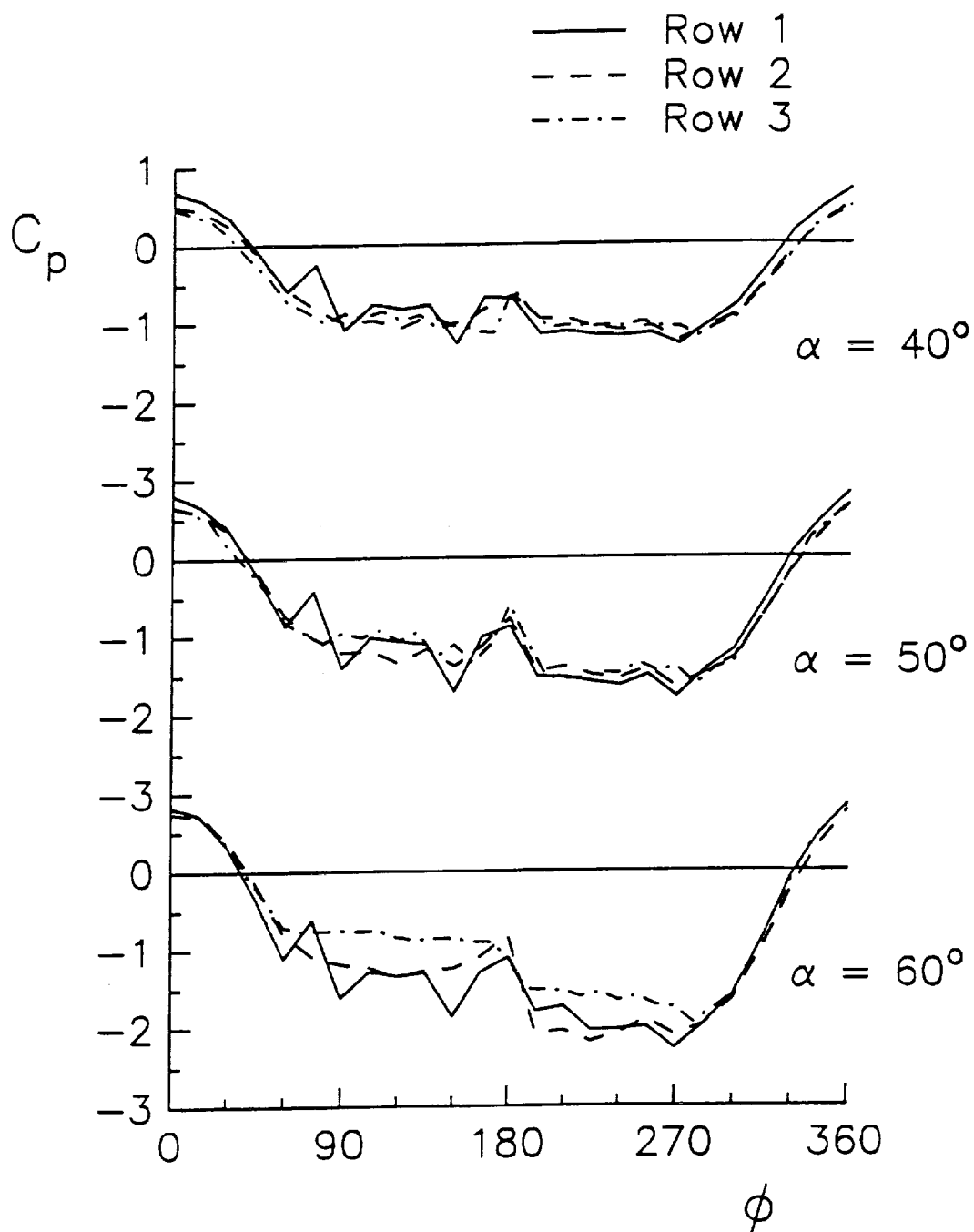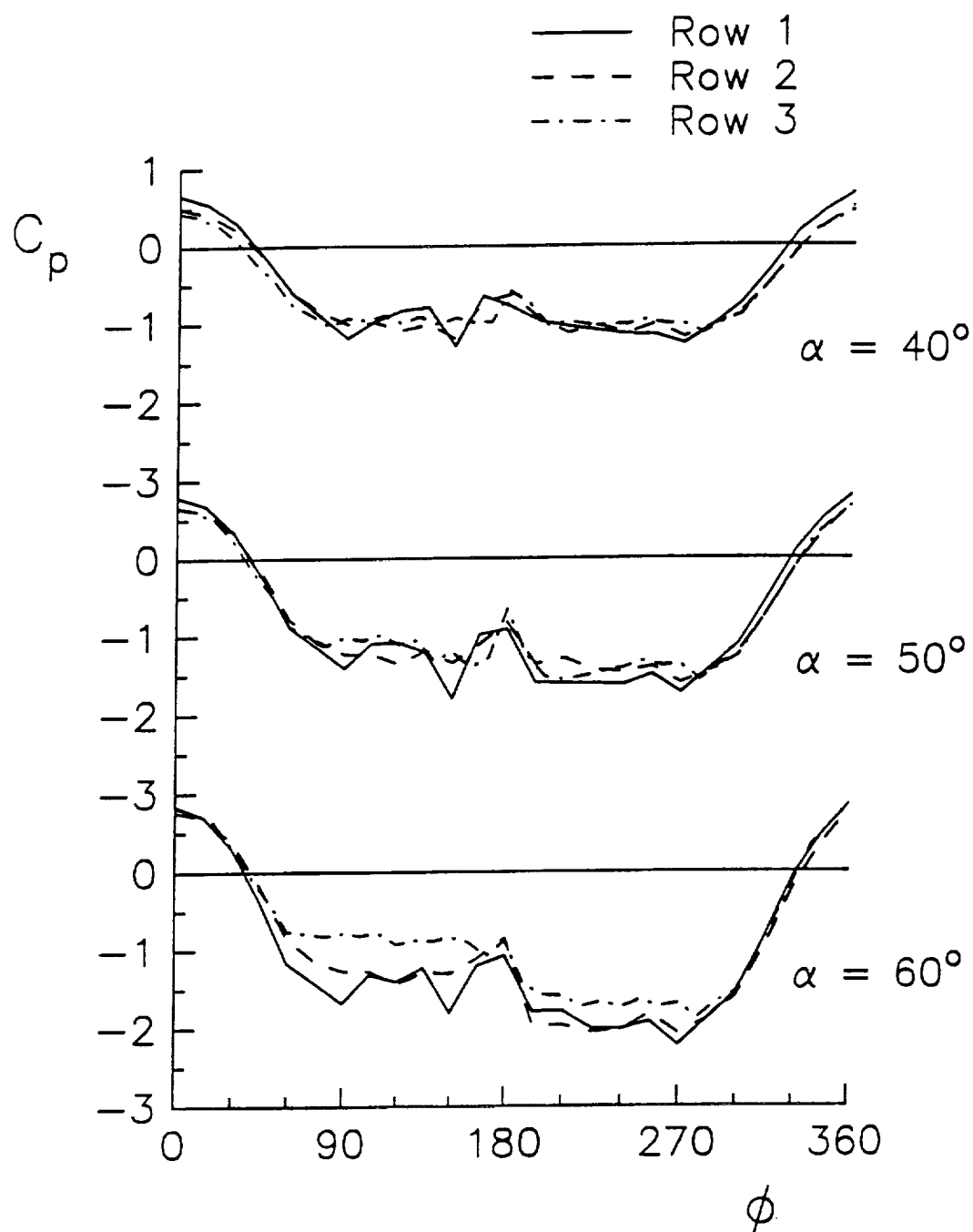
Figure 23 – "Baseline" Pressure Coefficient Distributions
Nozzle 1, $\phi_j = 120°$, $\phi_b = 240°$, $C_\mu = 0$
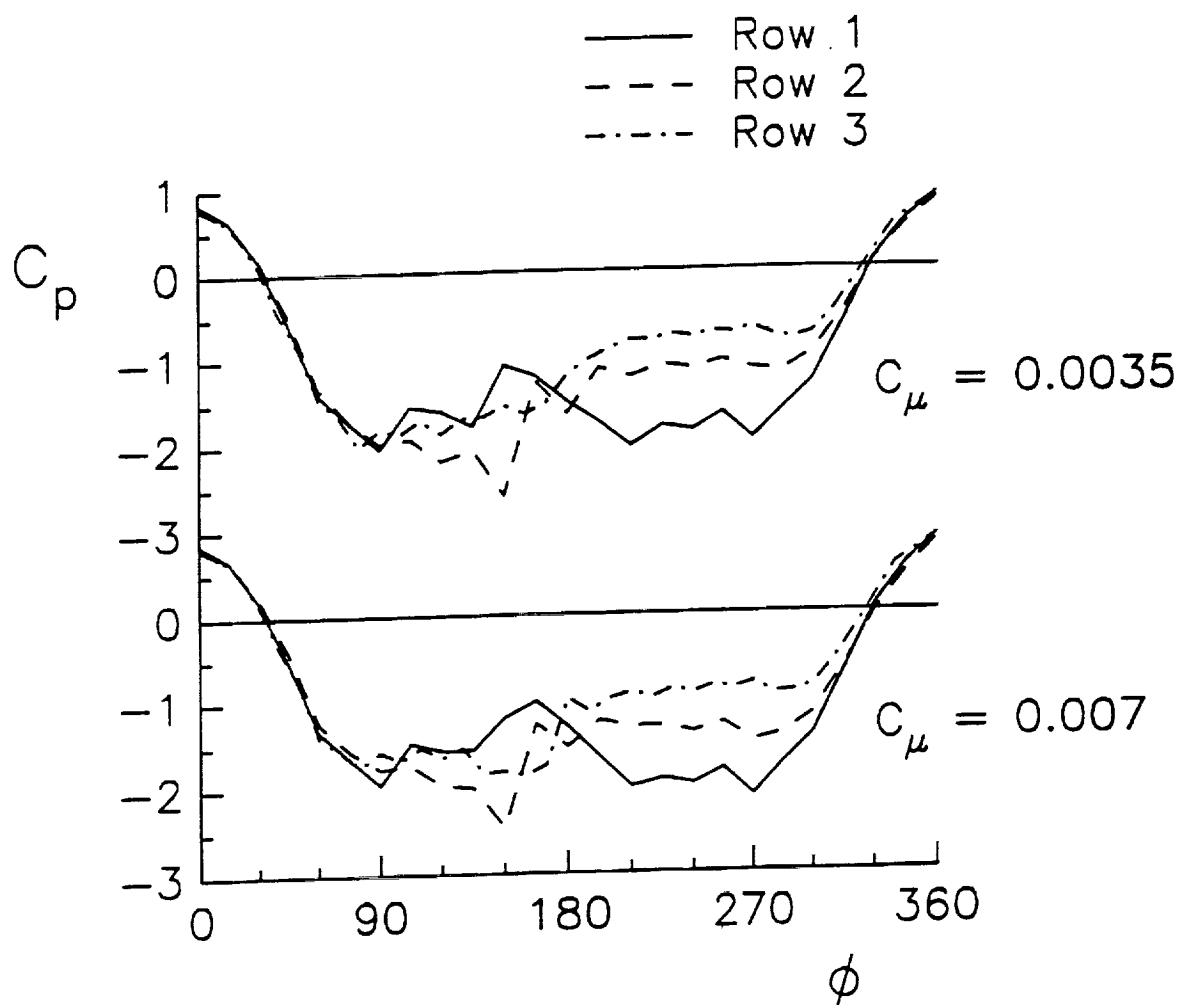
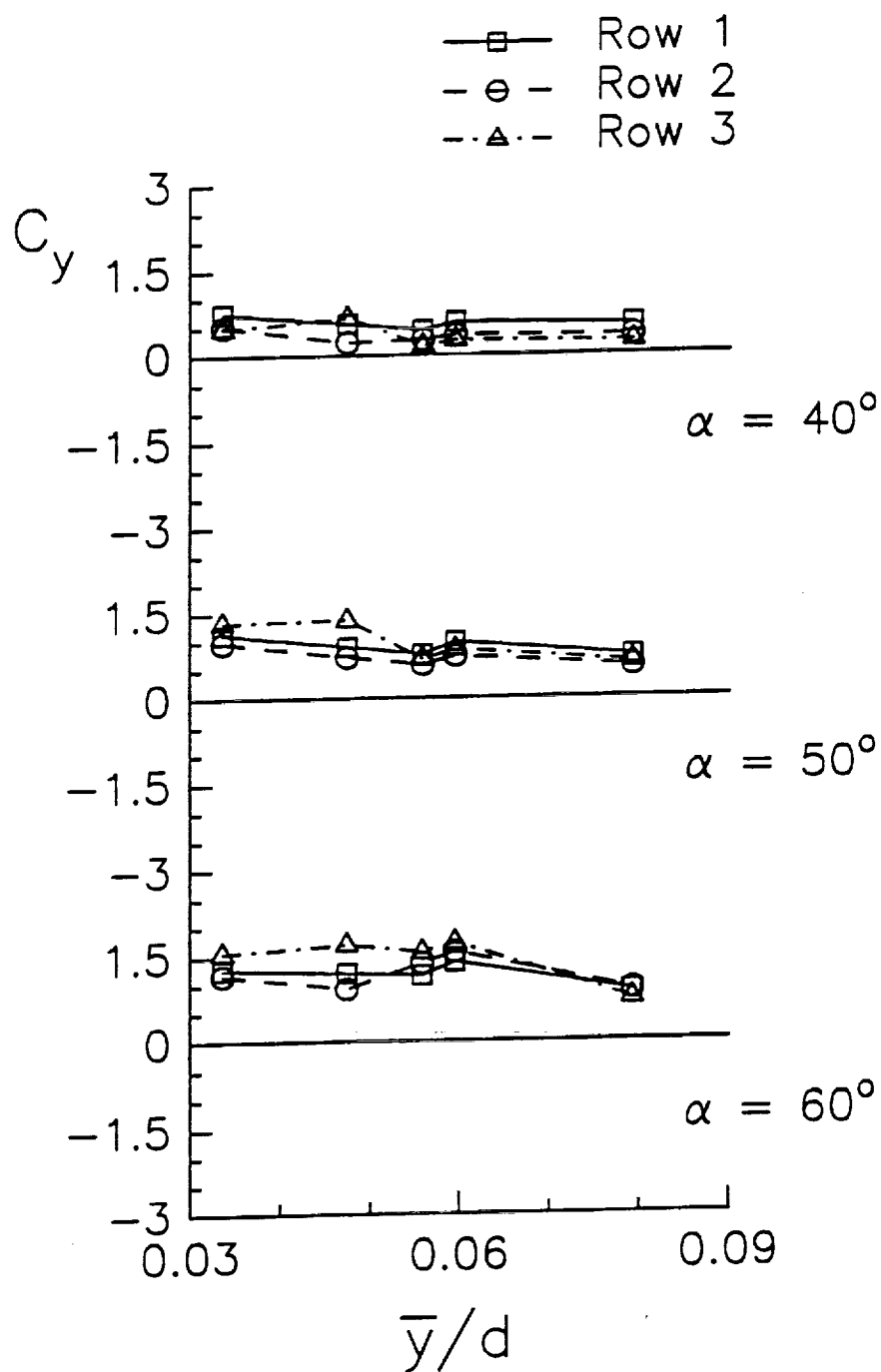Figure 24 – Pressure Coefficient Distributions
Nozzles 1 & 3, $\alpha = 60°$, $\phi_j = 120°$, $\phi_b = 240°$
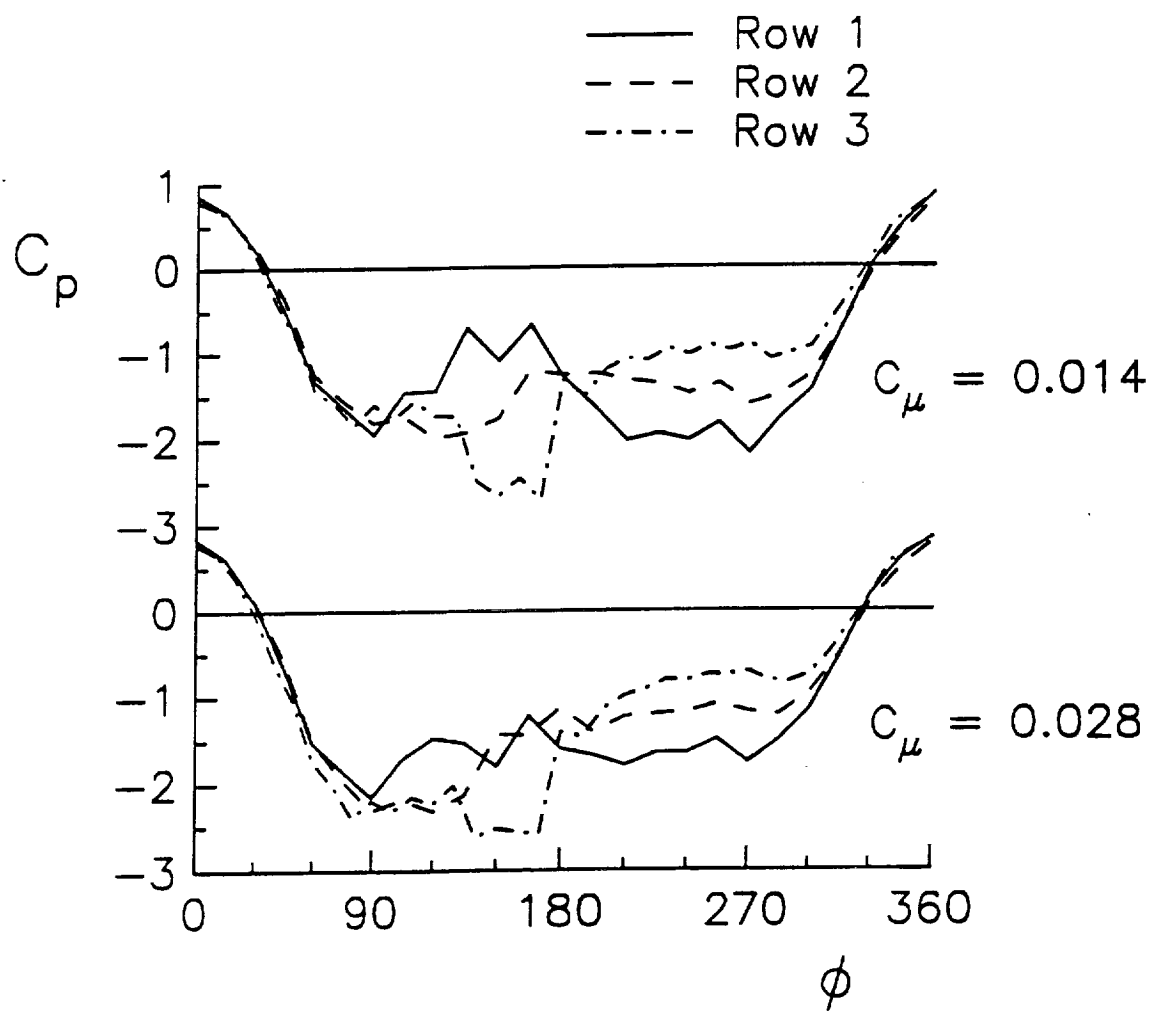
Figure 24 (continued) – Pressure Coefficient Distributions
Nozzles 1 & 3, $\alpha = 60°$, $\phi_j = 120°$, $\phi_b = 240°$
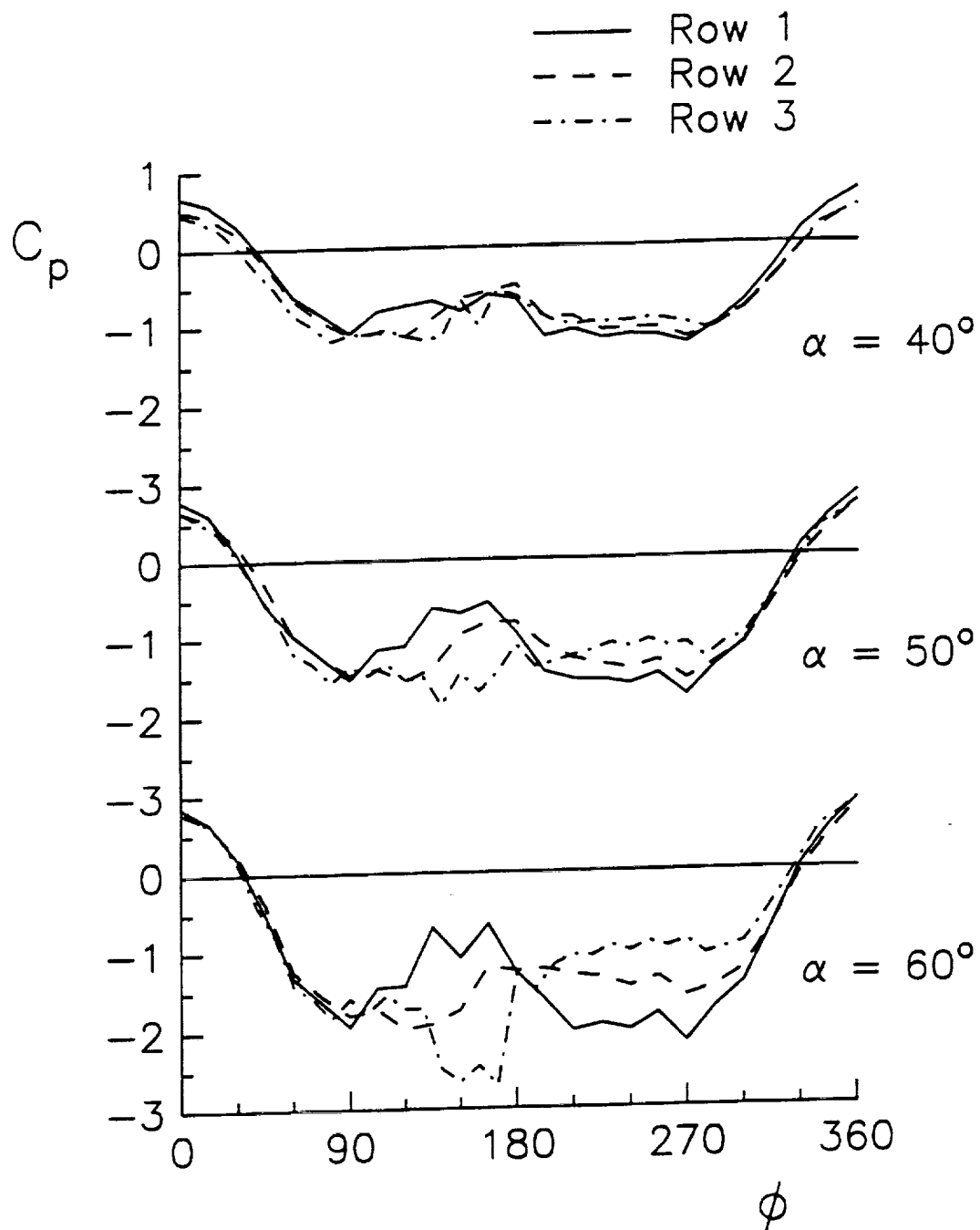
Figure 25 – Pressure Coefficient Distributions
Nozzle 1, $\phi_j = 120°$, $\phi_b = 240°$, $C_\mu = 0.014$
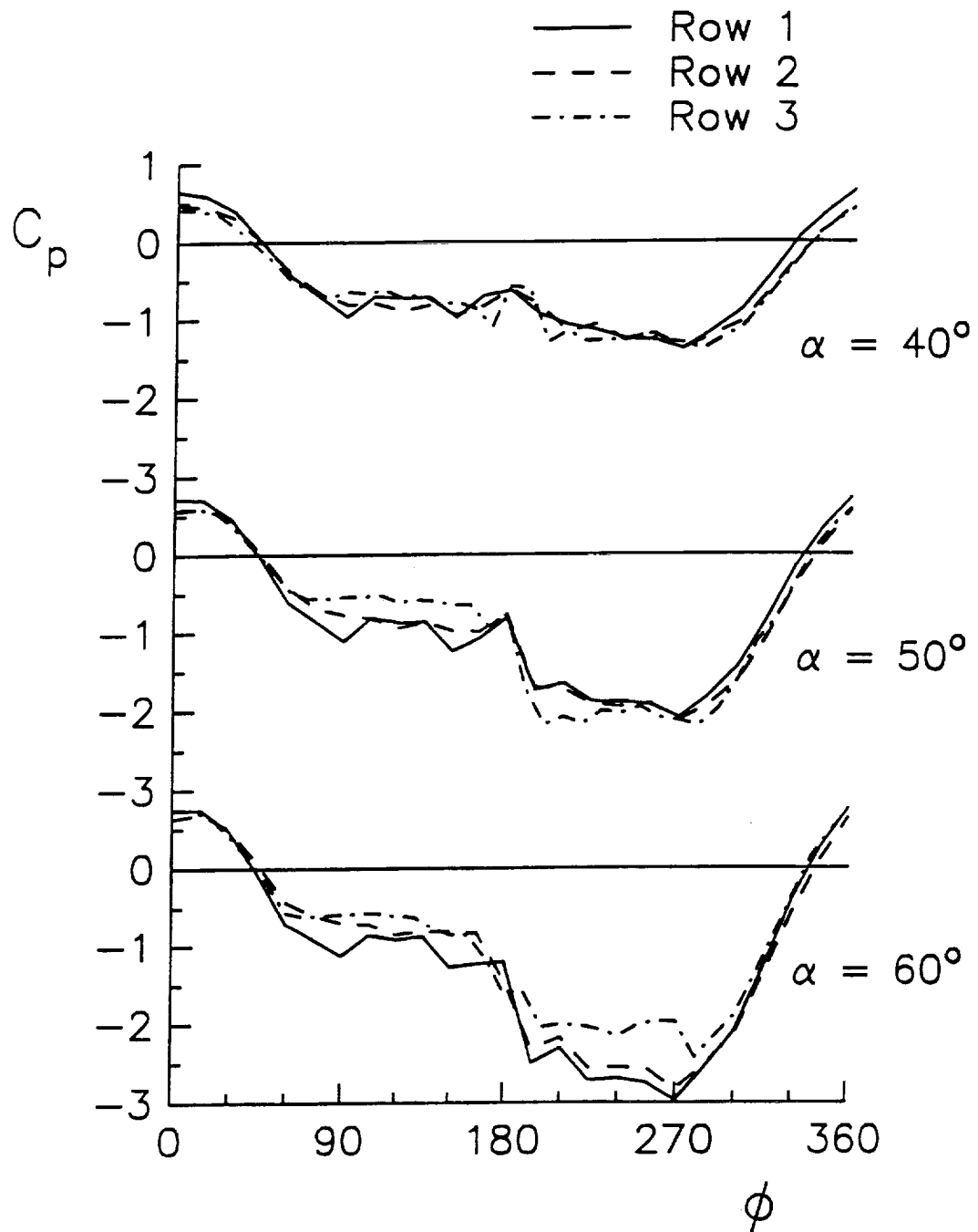
Figure 26 – "Baseline" Pressure Coefficient Distributions
Nozzle 8, $\phi_j = 120°$, $C_\mu = 0$
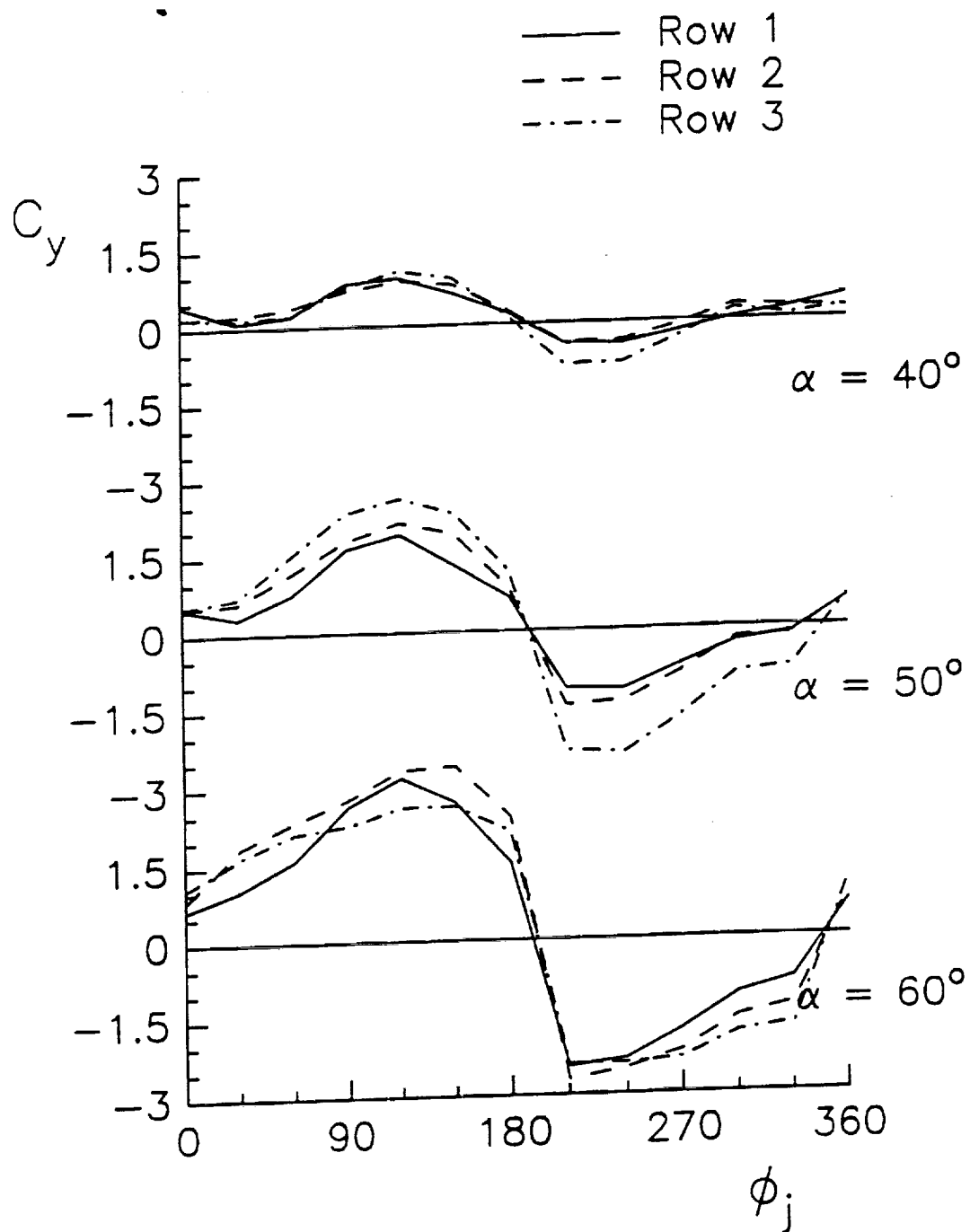
Figure 27 – "Baseline" Sectional Side Force Coefficient Plots
Nozzle 8, $C_\mu = 0$
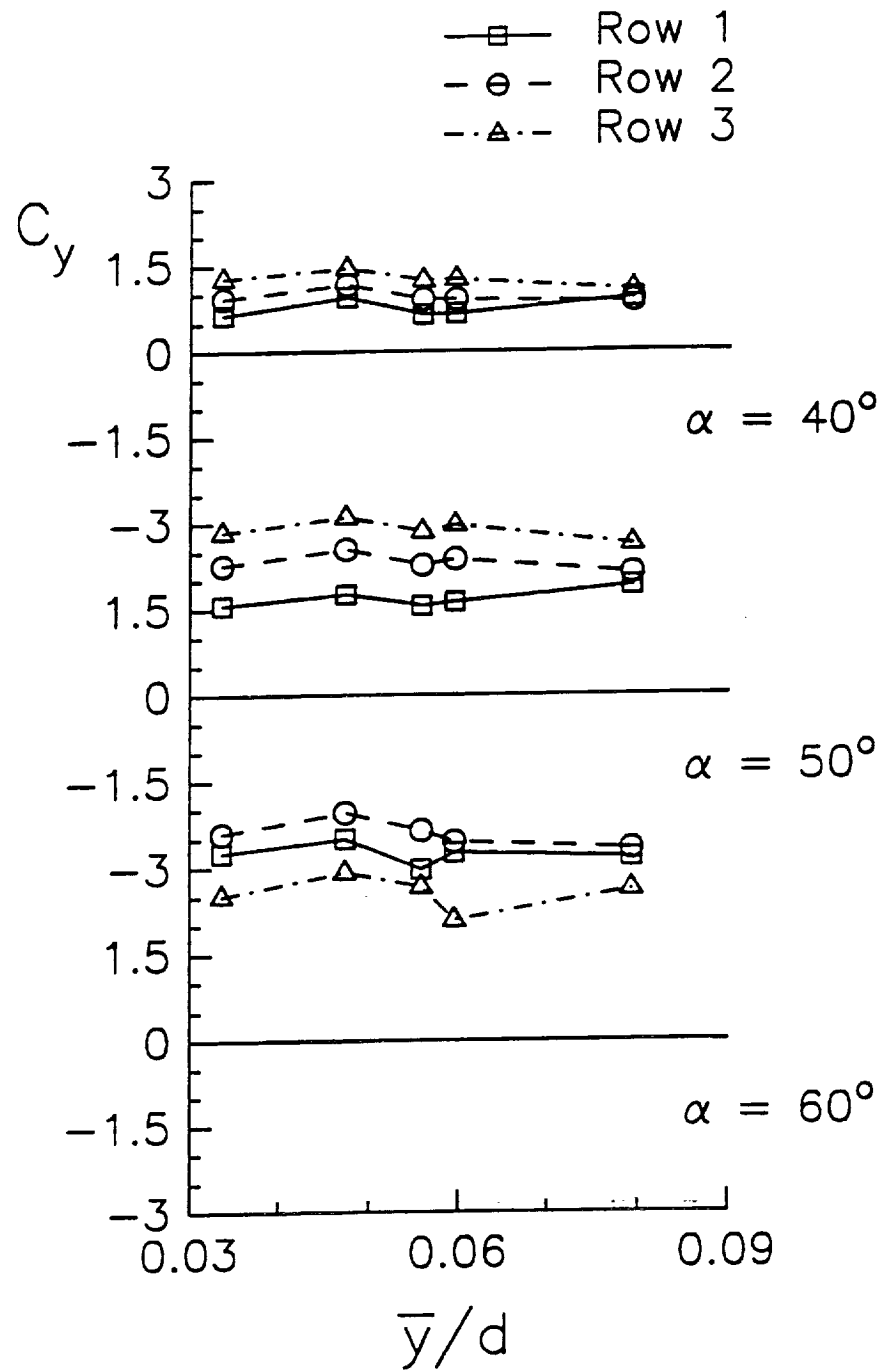
Figure 28 – "Baseline" Sectional Side Force Coefficient Plots
$\phi_j = 120°$, $C_\mu = 0$
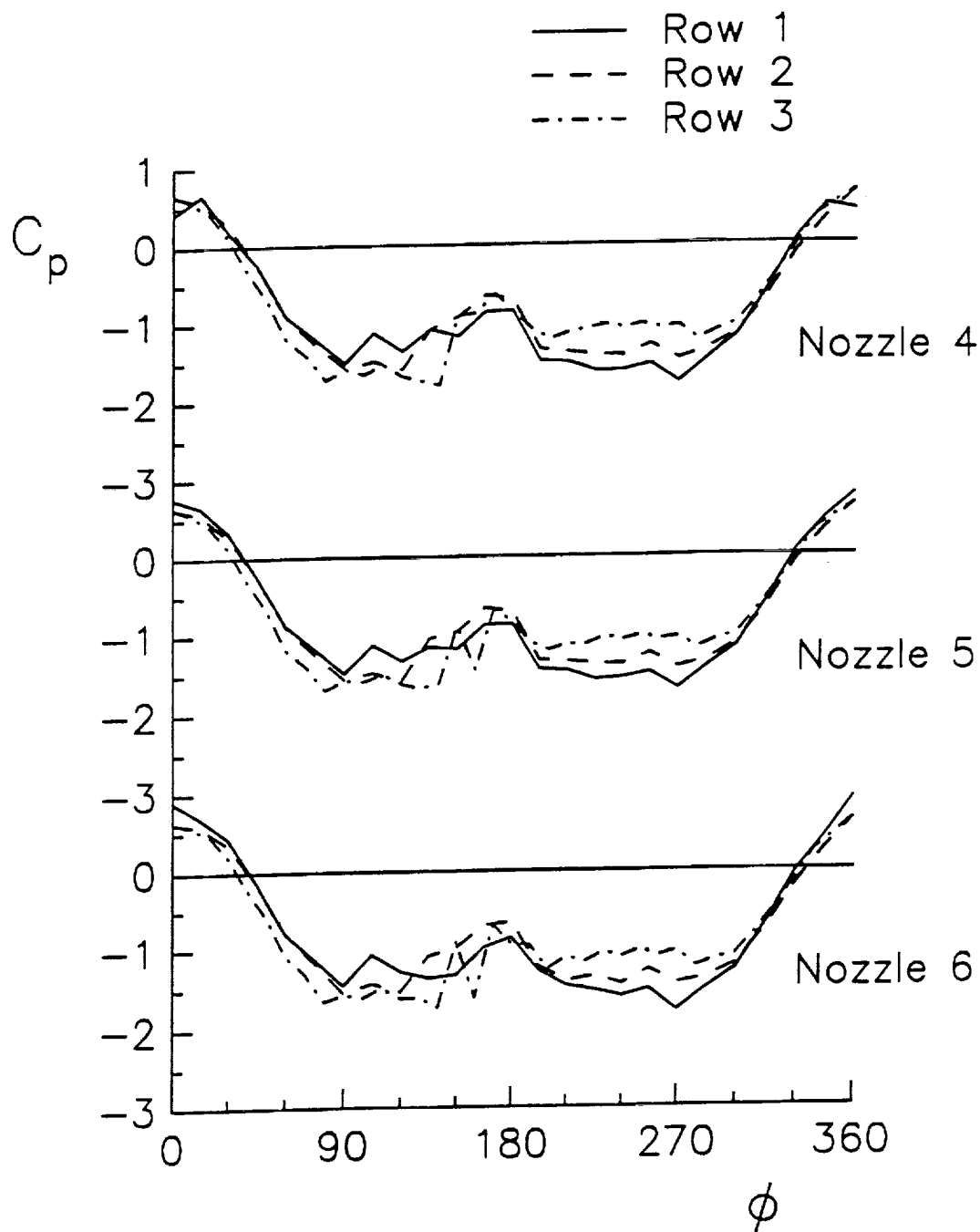
Figure 29 – Pressure Coefficient Distributions
$\alpha = 50°$, $\phi_j = 120°$, $C_\mu = 0.02$
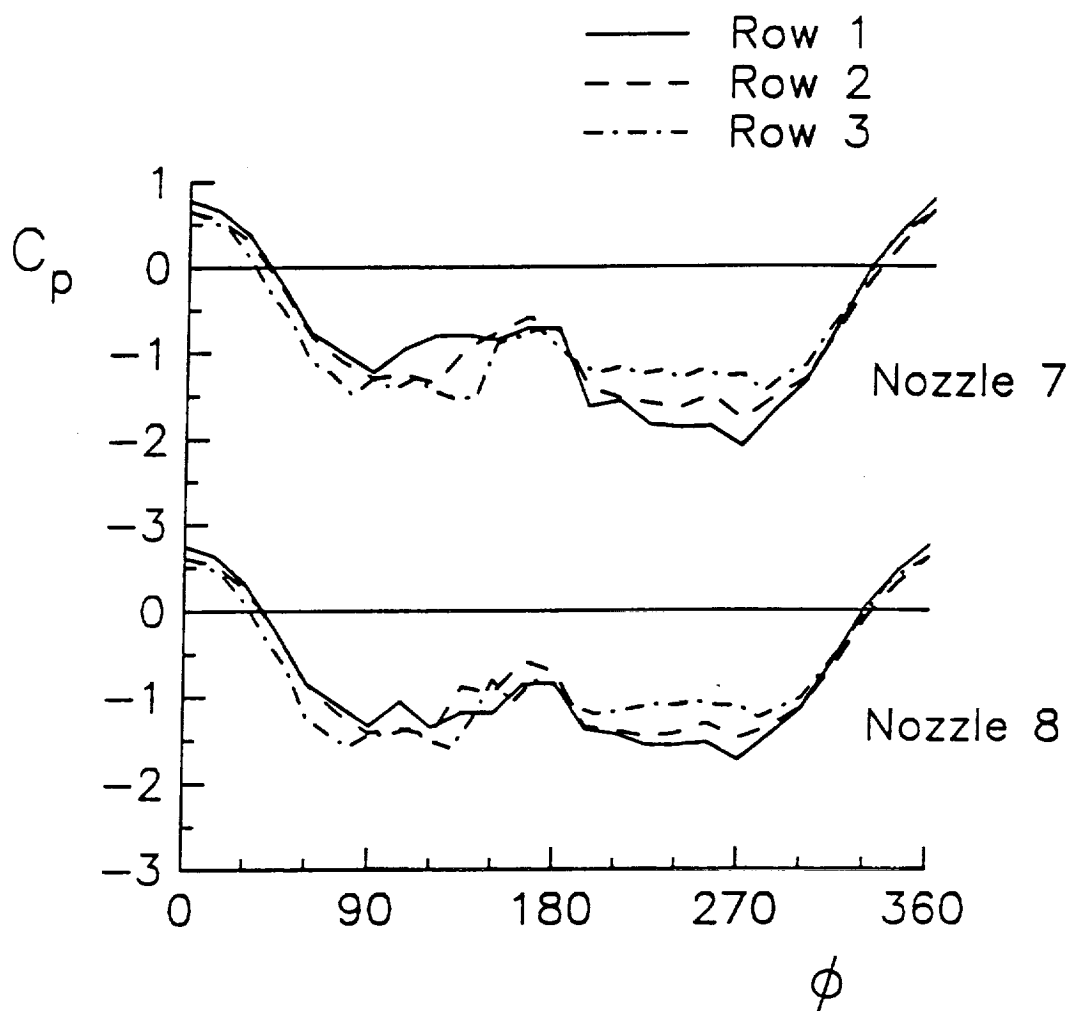
Figure 29 (continued) – Pressure Coefficient Distributions
$\alpha = 50°$, $\phi_j = 120°$, $C_\mu = 0.02$
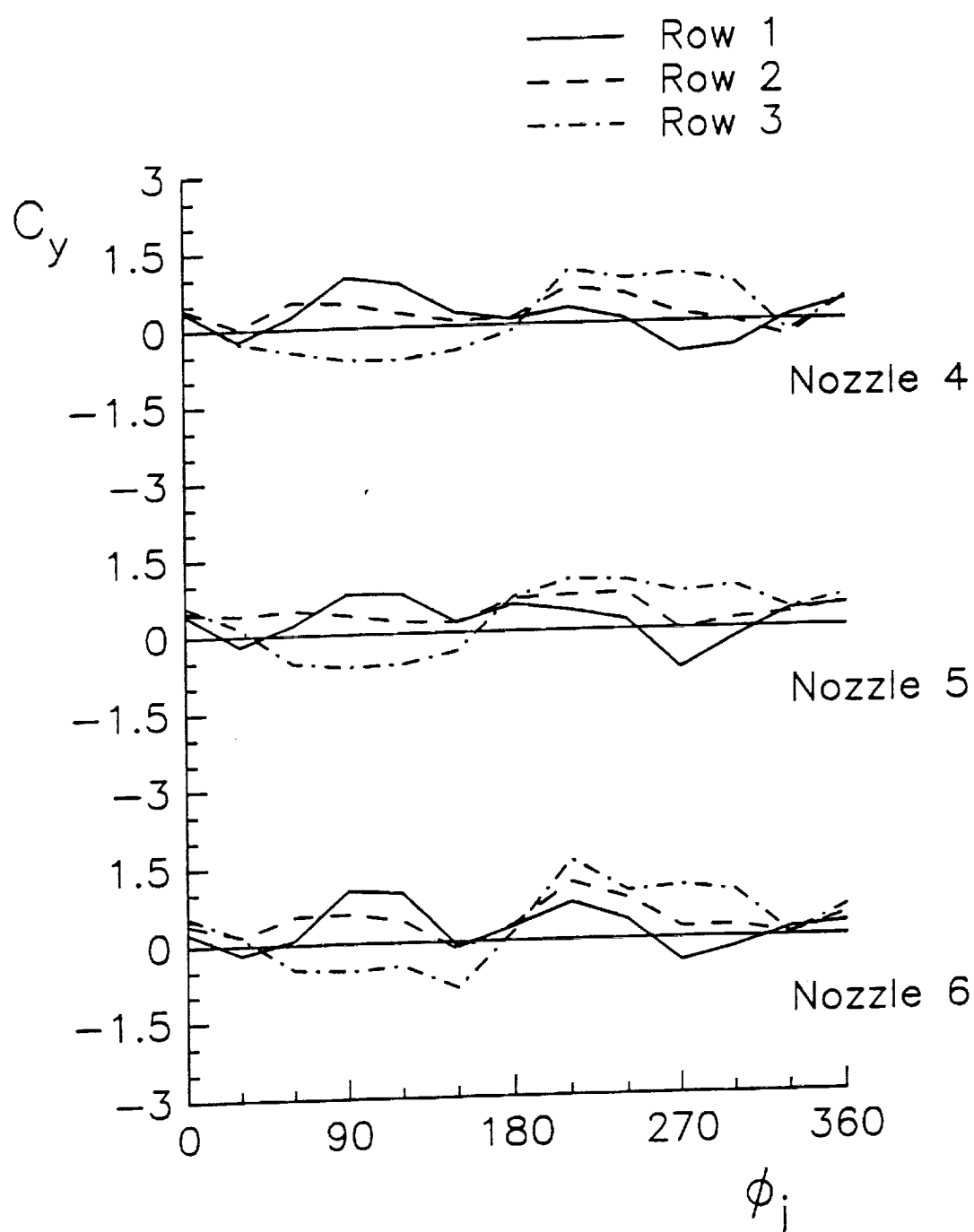
Figure 30 – Sectional Side Force Coefficient Plots
$\alpha = 50°$, $C_\mu = 0.02$
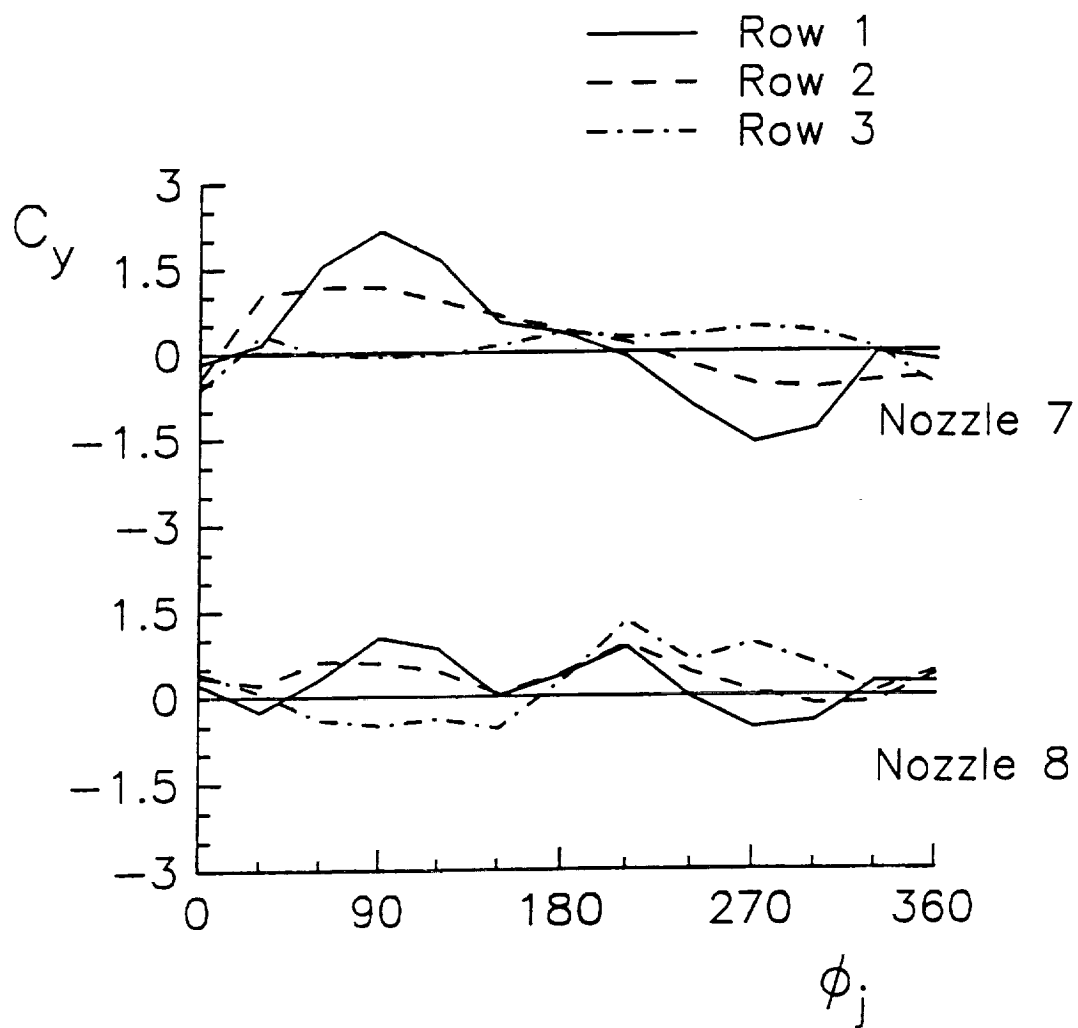
Figure 30 (continued) – Sectional Side Force Coefficient Plots
$\alpha = 50°$, $C_\mu = 0.02$
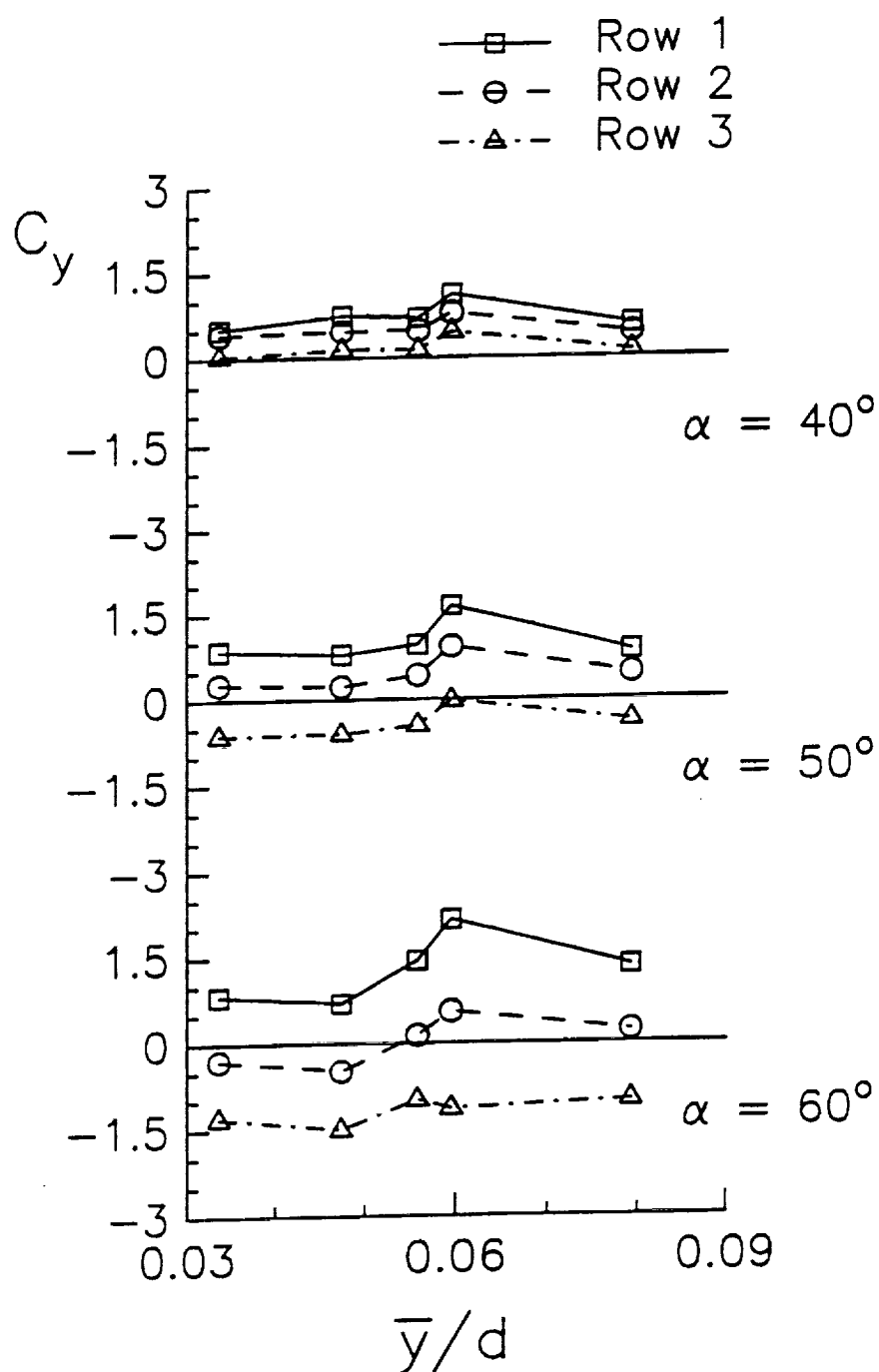
Figure 31 – Sectional Side Force Coefficient Plots
$\phi_j = 120°$, $C_\mu = 0.02$
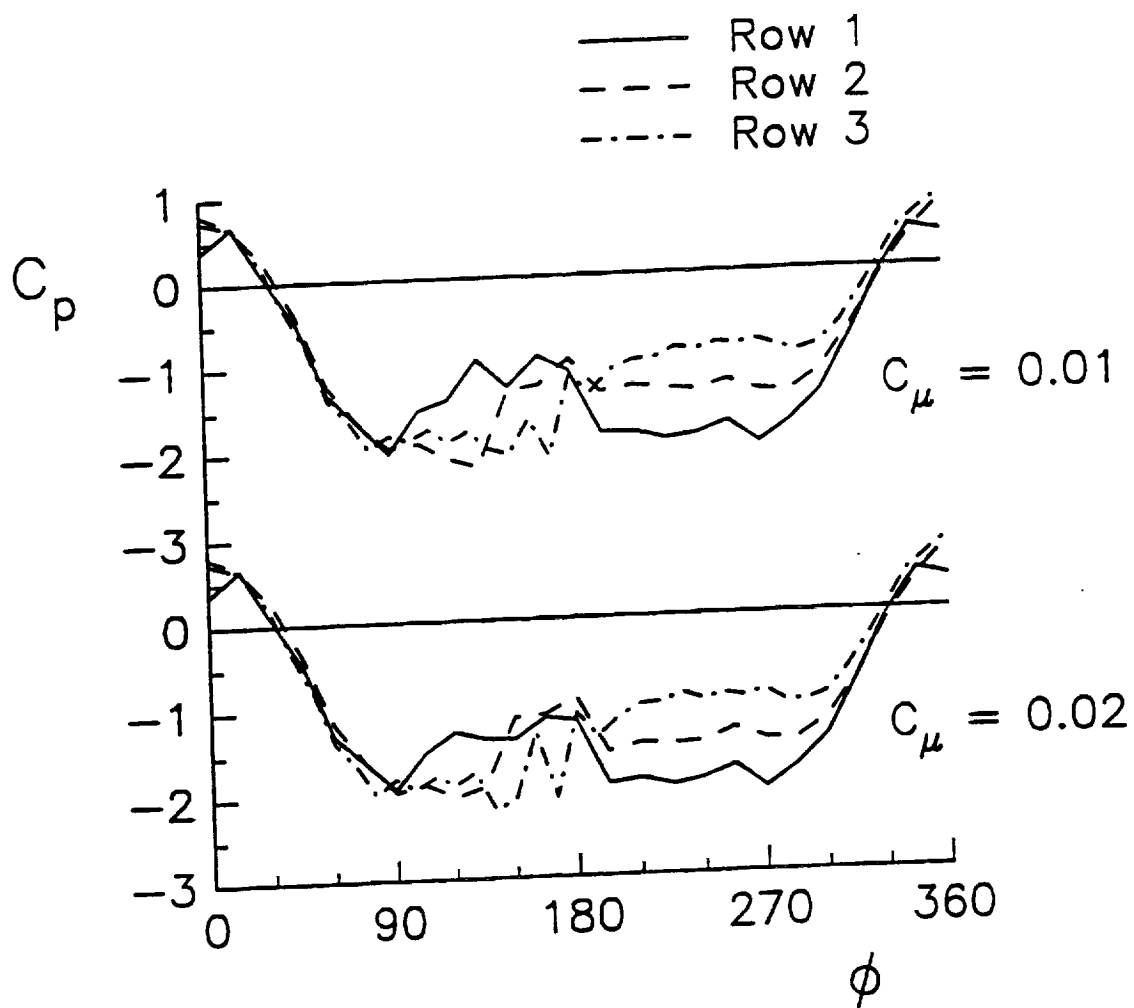
Figure 32 – Pressure Coefficient Distributions
Nozzle 8, $\alpha = 60°$, $\phi_j = 120°$

Figure 33 – Sectional Side Force Coefficient Plots
Nozzle 8, $\alpha = 60°$

Figure 34 – "Baseline" Pressure Coefficient Distributions
Nozzle 7, $\phi_j = 120°$, $\phi_b = 240°$, $C_\mu = 0$

Figure 35 – "Baseline" Sectional Side Force Coefficient Plots
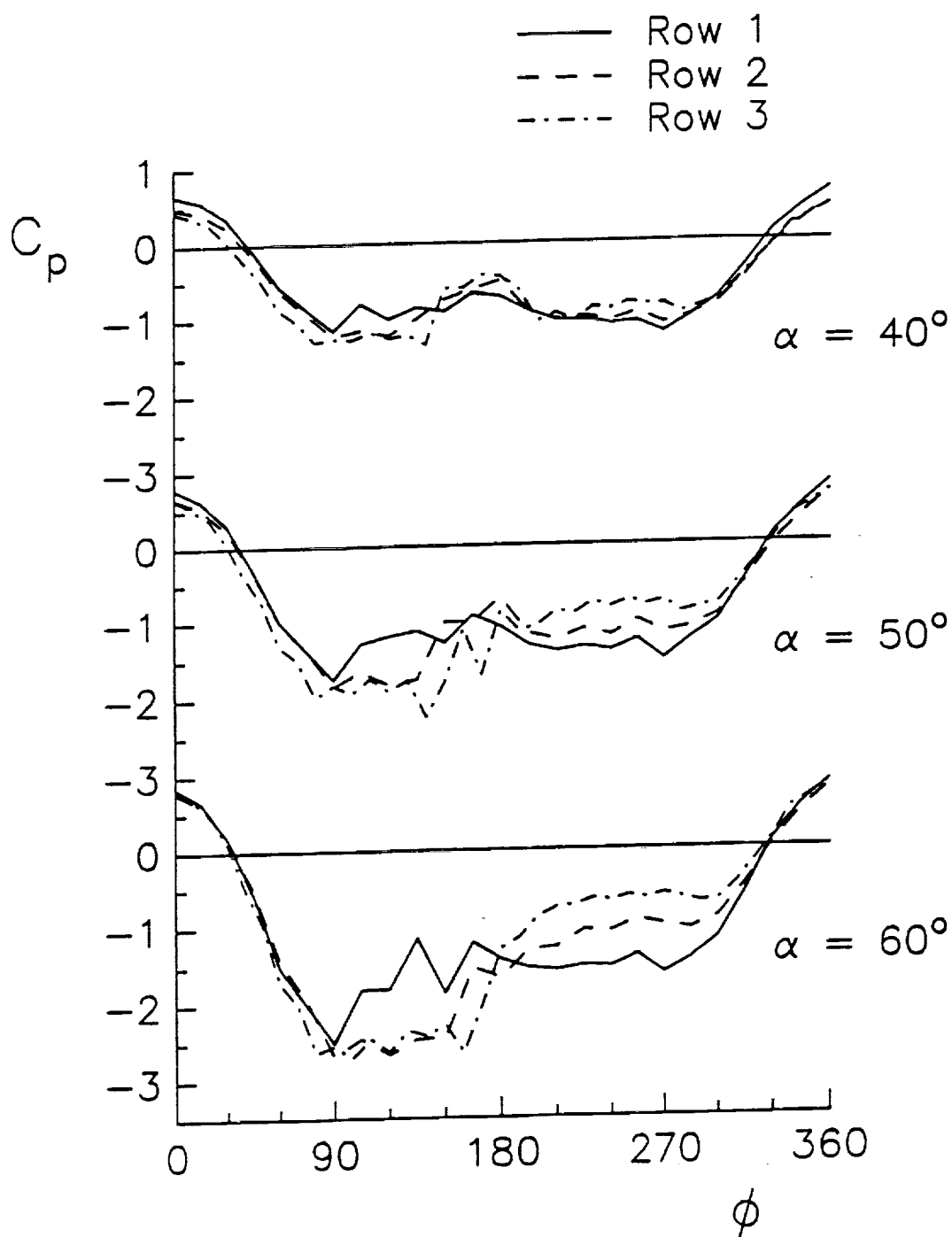$\phi_j = 120°$, $\phi_b = 240°$, $C_\mu = 0$
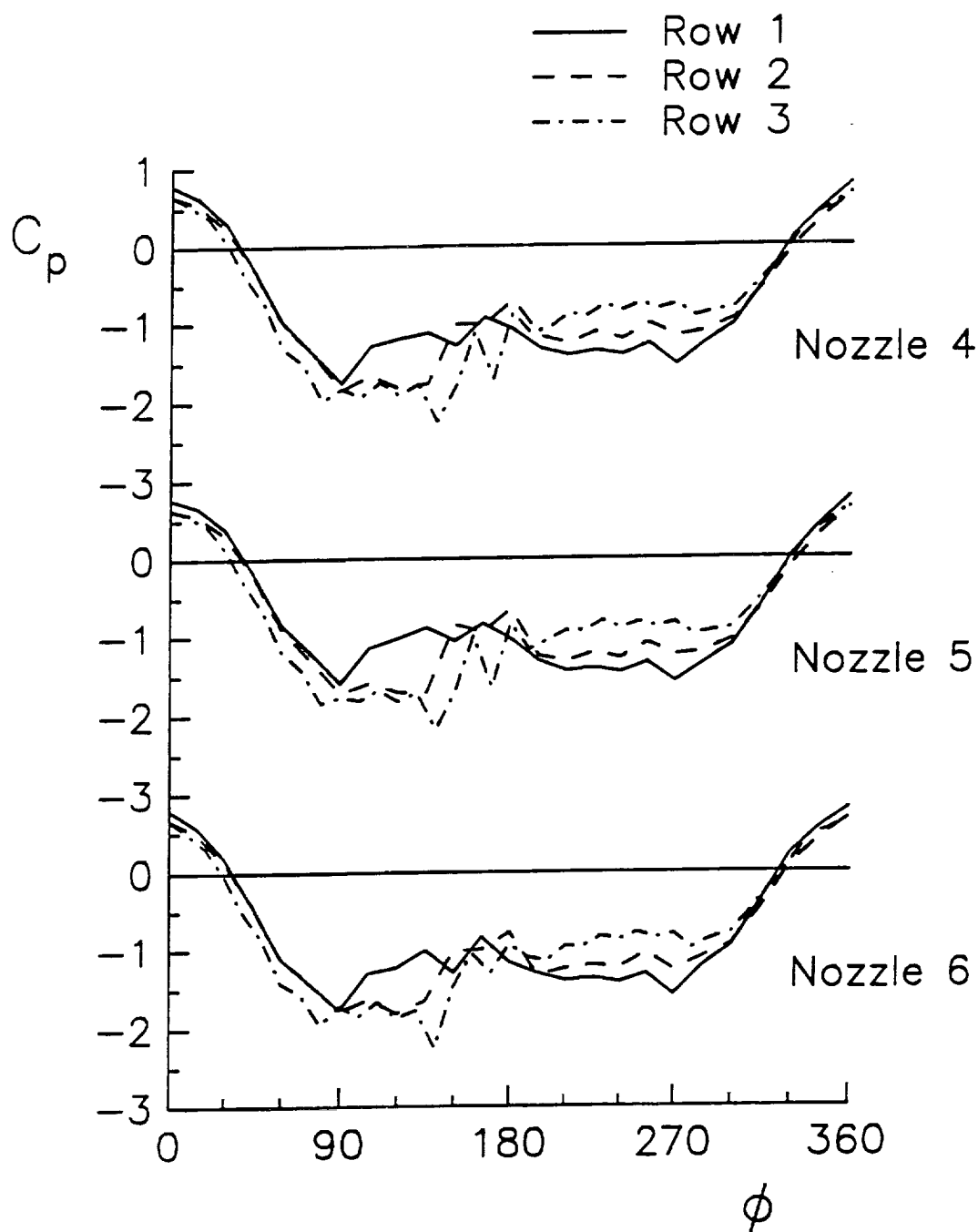
Figure 36 – Pressure Coefficient Distributions
$\alpha = 50°$, $\phi_j = 120°$, $\phi_b = 240°$, $C_\mu = 0.01$
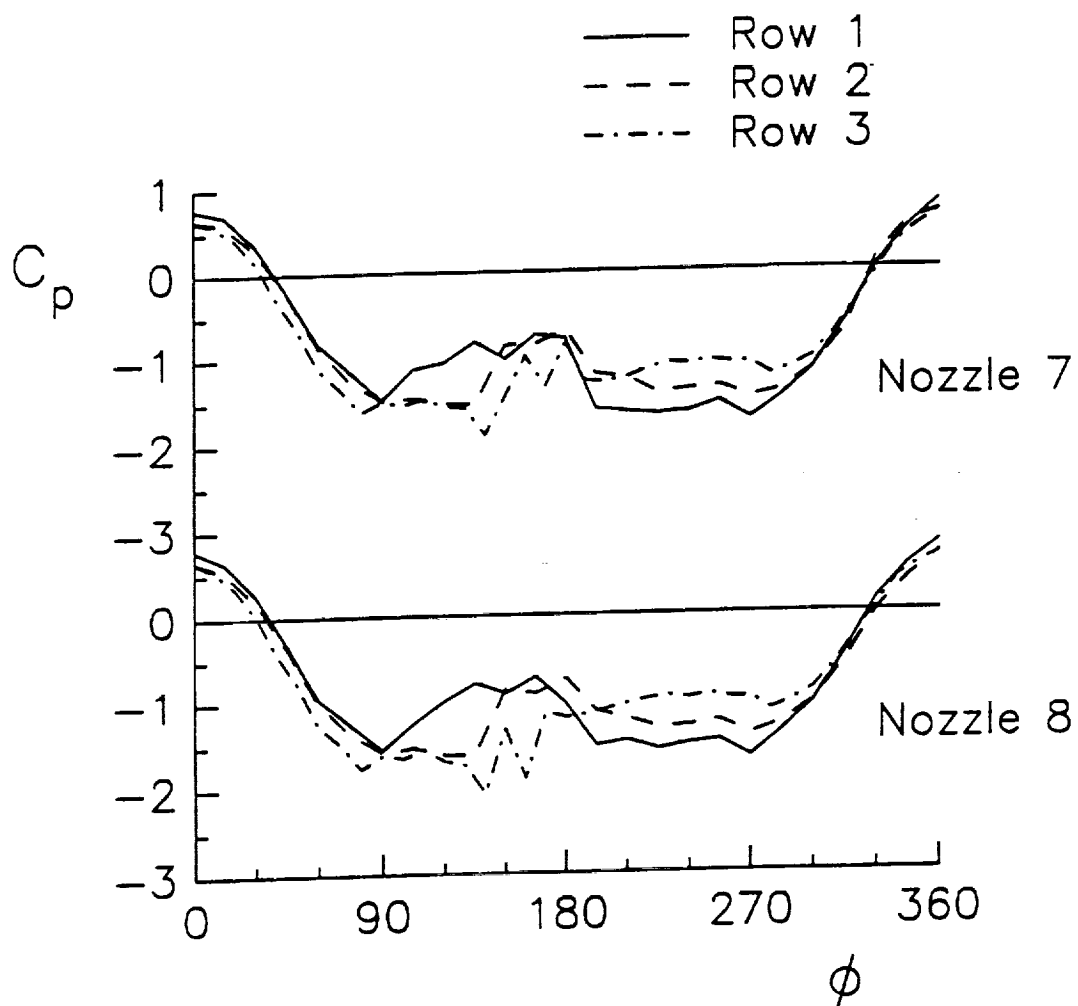
Figure 36 (continued) – Pressure Coefficient Distributions
$\alpha = 50°$, $\phi_j = 120°$, $\phi_b = 240°$, $C_\mu = 0.01$
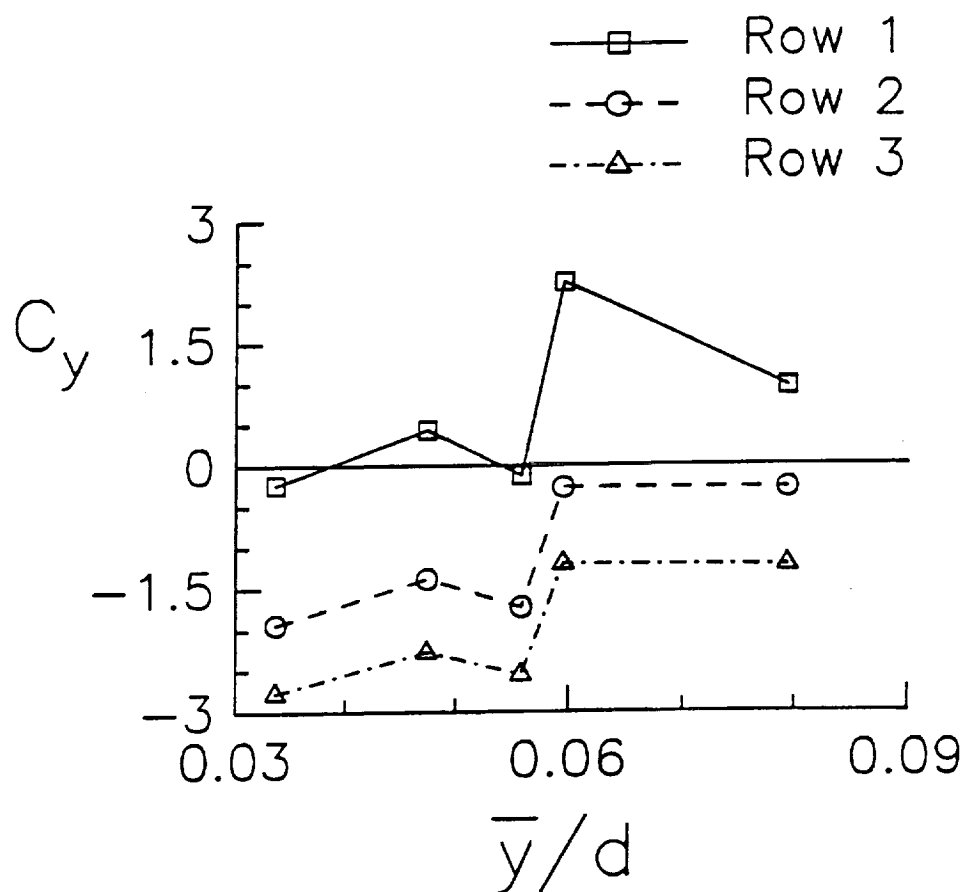
Figure 37 – Sectional Side Force Coefficient Plots
$\alpha = 60°$, $\phi_j = 120°$, $\phi_b = 240°$, $C_\mu = 0.01$

Figure 38 – Pressure Coefficient Distributions
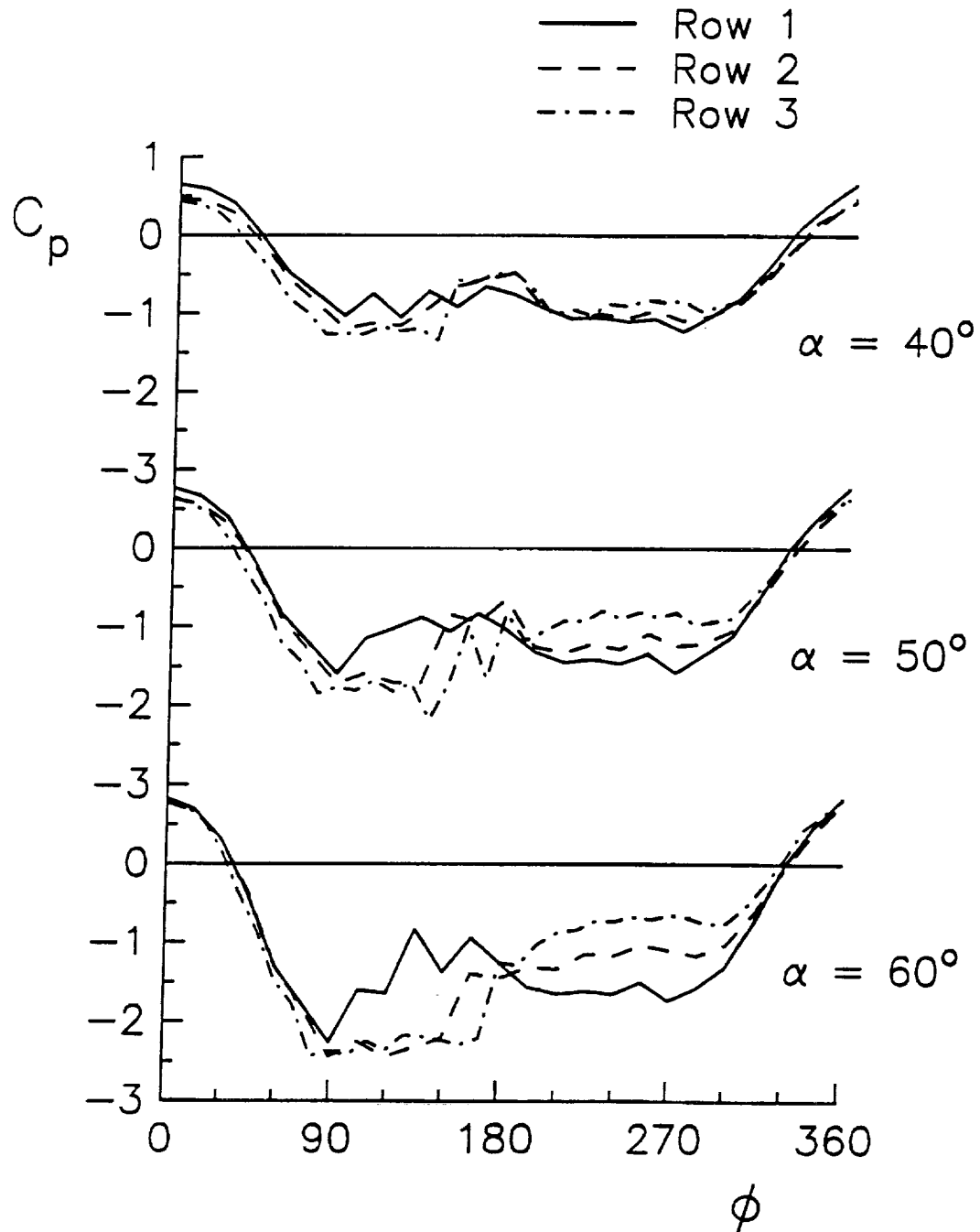Nozzle 4, $\phi_j = 120°$, $\phi_b = 240°$, $C_\mu = 0.01$

Figure 38 (continued)– Pressure Coefficient Distributions
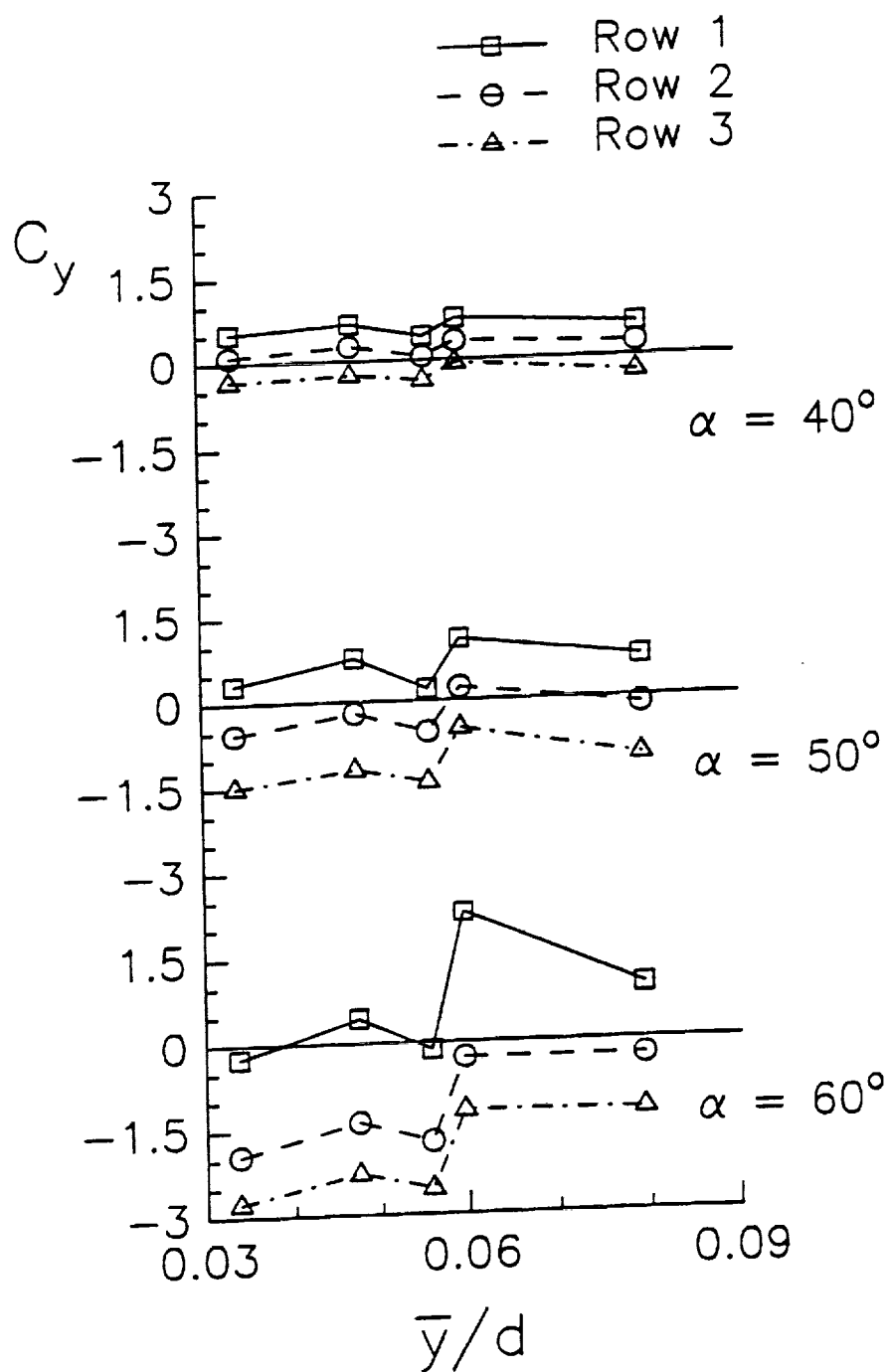Nozzle 5, $\phi_j = 120°$, $\phi_b = 240°$, $C_\mu = 0.01$

C-2

Figure 39 – Sectional Side Force Coefficient Plots
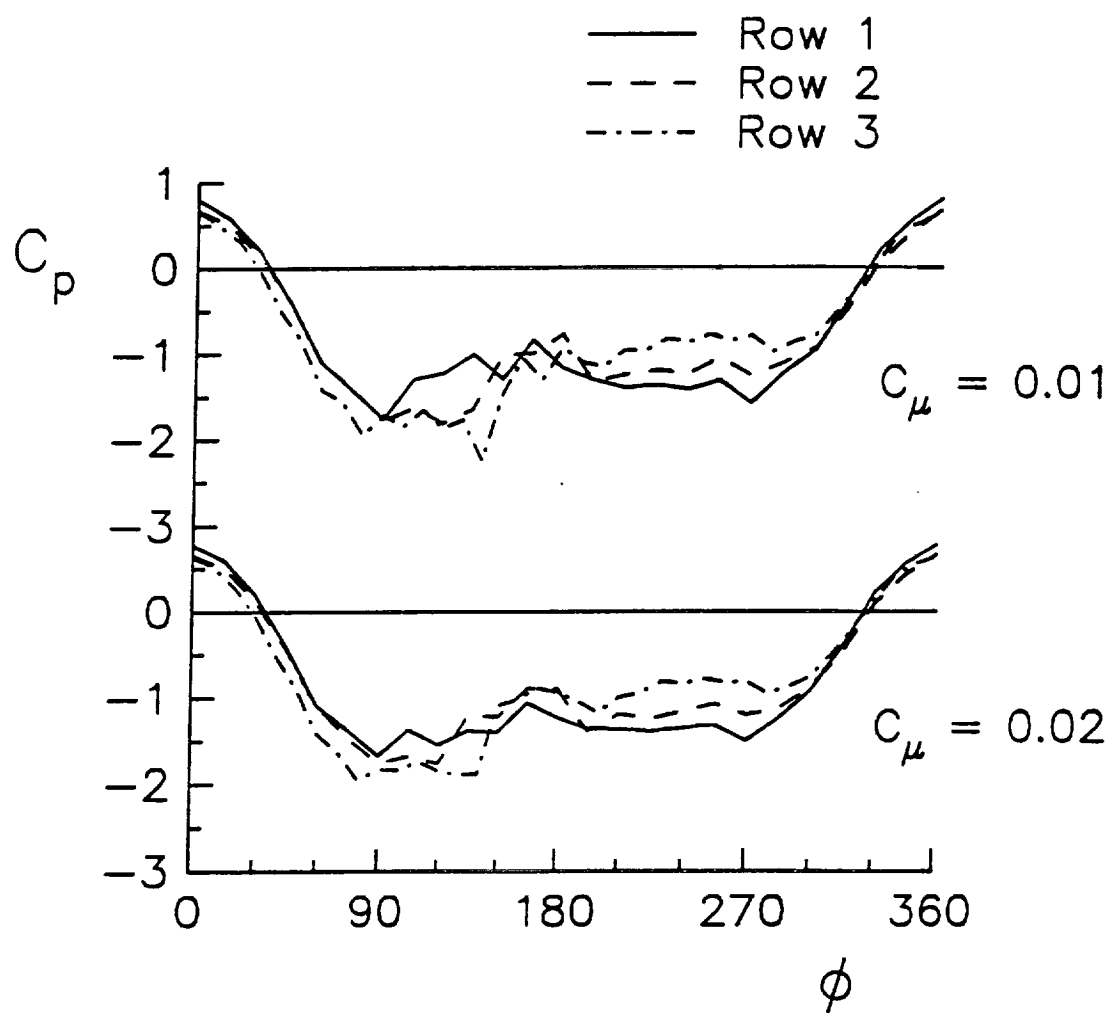$\phi_j = 120°$, $\phi_b = 240°$, $C_\mu = 0.01$

Figure 40 – Pressure Coefficient Distributions
Nozzle 6, $\alpha = 50°$, $\phi_j = 120°$, $\phi_b = 240°$

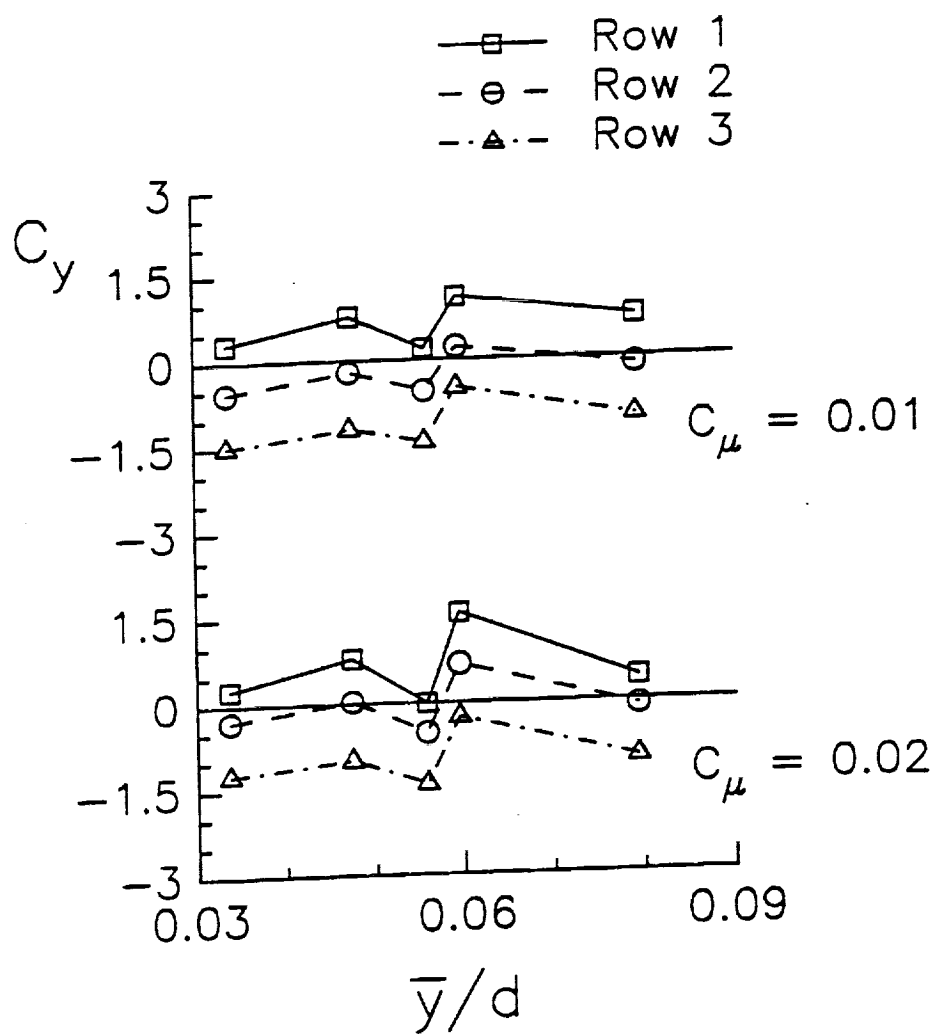Figure 41 – Sectional Side Force Coefficient Plots
$\alpha = 50°$, $\phi_j = 120°$, $\phi_b = 240°$